# DETECTION OF LUBRICATION STARVATION IN BALL BEARINGS BY MEANS OF LATERAL AND TORSIONAL VIBRATIONS

A Dissertation

by

JORGE ARTURO MIJARES TOBIAS

Submitted to the Office of Graduate and Professional Studies of
Texas A&M University
in partial fulfillment of the requirements for the degree of

DOCTOR OF PHILOSOPHY

| | |
|---|---|
| Chair of Committee, | Bryan P. Rasmussen |
| Committee Members, | Kim Won-Jong |
| | Chii-der Steve Suh |
| | Edgar Sanchez-Sinencio |
| Head of Department, | Andreas Polycarpou |

May 2018

Major Subject: Mechanical Engineering

# ABSTRACT

Considerable research has been conducted in fault detection and diagnosis for ball bearings but it has been focused on detecting the early stages of imminent faults due to fatigue. In reality, most bearings never reach the expected life or fatigue cycles due to problems related to maintenance or installation. This work studies lubrication starvation, which is one of the main causes of premature bearing failure.

This work focuses on explaining the origin of the frequency indicators based on proposed bearing models. The validation of one of the models is achieved through a series of experiments measuring lateral vibrations and proving that the characteristic signal originates from the gap created by the absence of lubricant. Additionally, several lateral vibration indicators are compared for fault detection concluding that Fast-Kurtogram is the best technique for detecting lubrication starvation. A further diagnosis using envelope analysis verifies another model that proposes the ball pass frequency of the outer race (BPFO) as the main indicator of lubrication starvation in the frequency domain.

An alternative method based on torsional vibrations at the shaft is additionally evaluated. A sensor based on the Time Interval Measurement System (TIMS) is developed using a field programmable gate array (FPGA) and a quadrature encoder to measure torsional vibrations. From the simulation of torque friction, the torque is found to not be significant compared to the driving torque of industrial motors. Hence the use of torsional vibrations as a mean to detect lubrication starvation is limited to applications in which bearing friction could impact the performance of the rotor drastically. The results are verified by the experiments in which the torsional vibrations are not able to detect changes in lubrication conditions.

Finally, an energy analysis is presented to study the impact of lubrication starvation in

the motor efficiency, which could be an economical motivator to encourage the research of condition monitoring of lubrication starvation. Lubrication starvation decreases the efficiency by dissipating power as heat and is dependent on the speed and static load rather than the load factor of the motor.

# DEDICATION

To my wife, mother, and my father.

# ACKNOWLEDGMENTS

I would like to mainly thank Dr. Bryan Rasmussen, for his great mentorship in this time of my life as a Ph.D. student, for his lessons that I will carry with me the rest of my life, and of course for the financial support to complete this work.

Additionally, I want to thank Dr. Steve Suh for the long talks full of helpful advices and for serving on my advisory committee together with Professors Kim Won-Jong and Edgar Sanchez-Sinencio.

I would also like to thank my wife for the incredible emotional support and wise counsel through out this process. I think this work is as much hers as it is mine.

Moreover, I want to thank the friends I gathered during this period of my life and my colleagues at the Themo-Fluids Controls Laboratory.

Finally, thanks to my family, for their support and encouragement.

CONTRIBUTORS AND FUNDING SOURCES

## Contributors

This work was supported by a dissertation committee consisting of Professors Bryan P. Rasmussen, Kim Won-Jong, Chi-ider Steve Suh of the Department of Mechanical Engineering and Professor Edgar Sanchez-Sinencio of the Department of Electrical & Computer Engineering.

## Funding Sources

Graduate study was supported partially by a CONACYT scholarship. This material is based upon work supported by the U.S. Department of Energy, Office of Energy Efficiency and Renewable Energy, Advanced Manufacturing Office, under Award Number DE-EE0007700. Any opinions, findings, and conclusions or recommendations expressed in this material are those of the author(s) and do not necessarily reflect the U.S. Department of Energy.

TABLE OF CONTENTS

Page

LIST OF FIGURES

FIGURE Page

LIST OF TABLES

TABLE Page

# 1. INTRODUCTION AND LITERATURE REVIEW

## 1.1 Background and Motivation

Failed bearings are the most common failure mode for electric motors and pumps [7]; therefore, condition monitoring of bearings is fundamental for a complete preventive maintenance program. There are different types of bearings depending on the applications [5], [8], from which deep groove ball bearings are the most common due their low friction, ease of maintenance and durability.

Bearing lifetime has increased with the advanced manufacturing technologies, but eventually all bearings fail due to fatigue, which is the cause of spalling (small indentations due fatigue cracks) on the surfaces in contact [5]. Current technology can detect the initial stages of spalling months in advance, but most bearings have premature failures due to improper lubrication [9] and 90% never reach their expected lifetime [10]. Improper lubrication could be divided in lubricant contamination, insufficient lubricant (lubricant starvation), aging of lubricant due to long time without renewal, and unsuitable lubrication selection for the application. For grease lubricated bearings, starvation is a common characteristic. The early detection and diagnosis of improper lubrication could maximize bearing lifetime and avoid downtime problems, hence the importance of developing condition monitoring methodologies that could deal with lubrication starvation.

The process of condition monitoring is classified by some authors in three stages [2]. The first stage is to detect the presence of a fault in the system (fault detection or screening). Once a fault has been found, the next stage is to determine the cause of the fault (fault diagnosis). In this stage is important to isolate the signal of interest and relate it to a known characteristic fault signature. The finally stage, called prognosis, is to predict the time of failure for a specific damaged component or system.

Efforts have been made to address the problem of lubrication starvation using lateral vibrations for detection and diagnosis. For the sake of clarity during this work, lateral vibration will refer to any vibration measured by an accelerometer, velometer or displacement sensor at the bearing housing in the radial or axial directions (X, Y or Z axis). Singh and Kazzas [11] found an increase in the root mean square (RMS) value of wavelet components related to dry bearing conditions proving that it is possible to isolate the frequencies associated with lubrication starvation. Using a more complex analysis, Boškoski et al. [12], found an increment in ball spin (BSF) and fundamental cage frequencies (FTF) by using spectral coherence analysis and fast-kurtogram to identify the frequency band affected by impacts. Boškoski proposed that fault signature on FTF and BSF is caused due the lack of movement restriction of the cage, created by the absence of lubricant filling the gaps between components.

Lateral vibrations measured at the ball bearings are the result of impacts of components that excite the natural frequency of the bearing and its housing, but the main effect of ball bearing is the friction torque [13] which could impact the efficiency of the system due all the energy dissipated as heat. Variations in friction torque impact the speed of the shaft which should be measured as a torsional vibration.

In rotor-machinery, torsional vibrations provide important information for fault detection. Some authors [14] have pointed out the advantage of torsional vibrations to retrieve useful information of the system. Since 1974, lateral vibrations are the standard in fault detection in industry (ISO 10816, VDI 2056), but some coupling between lateral and torsional vibrations have been demonstrated in the presence of some faults as shaft cracks [15] or misalignment in gears [16]. Research has been conducted to explain the relation between torsional vibration and faults as cracks, stator-rotor rub, misalignment, worn shafting, gear errors and other problems [15–20].

One of the most successful applications is in reciprocating machines for the detection

of faulty cylinders [21], [22], for gear trains to evaluate dynamic transmission error [23], [24] and for electromechanical systems [25]. Despite the relation between friction and speed variations, limited work has been done to relate faults in ball bearings to torsional vibrations. The most related work is a fault detection system developed by Bujoreanu and Breaban [26]. They detected scuffing (severe adhesive wear) by measuring friction torque using strain gages.

There are other methods used for condition monitoring of improper lubrication, mainly lubricant contamination and starvation. Monitoring of ball bearings with contaminated grease using acoustic emission (AE) measurement method was proposed by Miettinen and Andersson [27]. Their results proved that AE detects even low concentration (0.02 weight-%) of contaminant. Tandon et al. [28] compare the effectiveness of different condition monitoring techniques for detection of grease contaminants, acoustic emission and shock pulse maximum showed the best results for lubrication problems.

An interest in torque-based detection has recently increased due to applications where accelerometers or AE are not an option. A torque-base method was developed for a research reactor [29] were a bearing was submerged in lead-bismuth eutectic, which is a poor lubricant. The torque RMS was used as the indicator of bearing degradation and localized defects were diagnosed by methods used for lateral vibrations signals.

In conclusion, most of the work is focus in lateral vibrations detection or AE, but there is a need to understand the mechanics of lubrication starvation by corroborating that lack of lubrication increases the space between components; therefore, in this work is presented an experimental study that proves the relation between the space of inner components (clearance) and the characteristic signal of lubrication starvation.

Insufficient research has been conducted to take advantage of the variation of torque friction for fault detection, despite being the main impact of improper lubrication. For this reason, this work includes a characterization of the signal of lubricant starvation in tor-

sional vibrations and a methodology for the selection of a feature that indicates improper lubrication. During the development of this work it was found an impact of lubrication on torsional vibrations on a small system powered by a DC motor, but the impact was found to be negligible for bigger systems used commonly on industry (Induction Motors > 1/4 hp).

Finally, a study of the impact of lubrication starvation in the energy efficiency is presented. The study is complemented with an economical analysis using the data of a real plant to show the potential savings of implementing the fault detection techniques proposed in this work. The possibility to maximize the lifetime of the machines together with the potential energy savings are a strong motivator to continue the research in lubrication starvation.

## 1.2 Tribology

The fundamental theory to understand the effect of inappropriate lubrication on lateral/torsional vibrations is covered by tribology (branch of mechanical engineering in charge of lubrication, friction and wear).

The main effect of ball bearings in torsional vibration is friction torque, Ragulskis [13] identify eight different causes that compose the friction torque:

- Differential sliding.
- Gyroscopic spin.
- Elastic hysteresis in the materials of contacting bodies.
- Geometric errors and the effect of microasperities on contact surfaces.
- Cage contact with balls.
- Shear and shifting of lubricant.

- Caused by the environment of the bearing
- Temperature increase.

In the problem of lubrication starvation the relevant components are friction of shear and shifting of lubricant. Sier et al. [30] obtained a model that include all components of friction torque using the law of energy conservation and Wang et al. [31] proved that this model is more accurate than the torque model of the Swedish ball bearing factory SKF (Svenska Kullagerfabriken) [32] for high-speed ranges and high radial loads, but in normal speed and normal loads both models are in good agreement. The SKF model (4S model) was derived from a computational model that considers all the components in ball bearings [33], similar to the components mentioned by Ragulskis. The total friction moment $M_f$ for the 4S model is given by

$$M_f = \phi_{ish}\phi_{rs}M_{rr} + M_{sl} + M_{seal} + M_{drag}, \tag{1.1}$$

where $M_{rr}$ represents rolling friction, $M_{sl}$ sliding friction, $M_{seal}$ seal friction and $M_{drag}$ the drag losses. The effect of inlet shear heating and replenishment/starvation are considered with the factors $\phi_{ish}$ and $\phi_{rs}$ respectively. The sliding friction component considers two friction losses in the contact area: lubricant shearing and/or asperity contact. Sliding friction is described as

$$M_s l = \phi_{bl}M_{bl} + (1 - \phi_{bl})M_{EHL}, \tag{1.2}$$

where $M_{bl}$ and $M_{EHL}$ are asperity contact (dry friction) and lubricant shearing friction (obtained from lubrication model), respectively. A more complete description of the other friction components could be found in [29] and values for friction parameters in [34].

In sliding friction component the lubrication model has the most impact due the need to model the transition from lubricant shearing to asperity contact. The transition is con-

trolled by the weighting factor $\phi_{bl}$ which is a function of the film parameter $\Lambda = h/\sigma_s$, the ratio between minimum lubricant film thickness $h$ and surface roughness $\sigma_s$. In a further section, the method to calculate the weighting factor is covered by the Greenwood-Williamson model (GW model).

### 1.3 Elasto-Hydrodynamic Lubrication Theory

Lubrication has been a topic of research for more than 100 years, a complete review on the historical background of lubrication theory was presented by D. Dowson [35]. The most used lubrication models are Hydrodynamic Lubrication (HL) and Elasto-hydrodynamic lubrication (EHL). Both models are concerned with calculating the minimum film thickness of lubrication generated between the surfaces in contact but EHL is more used for rolling bearings, high loads or high speeds. To generalize the use of EHL equations, a set of dimensionless groups are used:

- Load parameter: $W = \frac{w}{E'R}$
- Speed parameter: $U = \frac{\eta_0 u}{E'R}$
- Material parameter: $G = \alpha E'$
- Minimum thickness parameter: $H = \frac{h}{R}$

where, $w$ is the load per unit width, $E'$ is the effective elastic modulus of the roller pair, $R$ is the effective radius of roller pair, $\eta_0$ and $\alpha$ are viscous properties of lubricant, $u$ is speed and $h$ is the unknown film thickness. After a series of iterations to improve the EHL model [36–38] and with the advances of computational resources [39] the most appropriate model for ball bearings is given by Equation 1.3, which is the point contact that includes the ellipticity parameter $k$.

$$H^{**} = 3.63 * U^{0.68} G^{0.49} W^{-0.073} (1 - e^{-0.68k}). \tag{1.3}$$

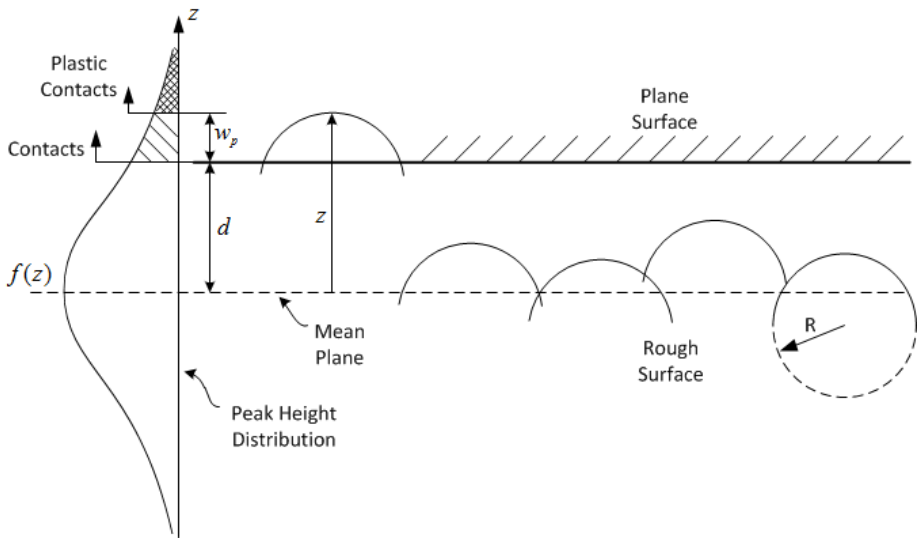


Figure 1.1: Greenwood and Williamson stochastic model for surface roughness

## 1.4 GW Model

Bearing roughness is known to be microscopic but comparable with the lubricant film thickness is considerable [40]. For that reason, full separation between the two surfaces is achieved but only if the minimum film thickness is greater than the highest spots of both surfaces combined, however, this is not the usual case. As a result, there is friction due elastic and plastic contact of high spots. The distribution of these high spots is random, so stochastic models are applied to model this interaction.

In 1966 Greenwood and Williamson [41] proposed a model for the contact of a rigid plane and a elastic rough surface where only few peaks are in contact with the plane. The two surfaces are separated by a distance $d$ measured from the mean plane of the rough surface as shown in Figure 1.1. The model assumes a normal distribution for the peak height with all peaks having a spherical shape with identical radius $R$ and a uniform distribution of summits per unit area. The peaks in contact will exhibit a degree of plastic flow when the deformation exceed the elastic region defined by $w_p$.

As mention before, the height of the peaks is normally distributed

$$f(z) = \left(\frac{1}{2\pi\sigma_s^2}\right)^{1/2} e^{-\frac{z^2}{2\sigma_s^2}}, \tag{1.4}$$

where $\sigma_s$ is the standard deviation of the height distribution and is called roughness. Hence the probability that a random selected peak has a height higher than $d$ is

$$P[z > d] = \int_d^\infty f(z)ds. \tag{1.5}$$

This value could be found by normalizing the distribution and using the standard normal curve with 0 mean and standard deviation of 1.0, the probability is now given as

$$P[z > d] = \int_{d/\sigma_s}^\infty \phi(x)dx = F_0\left(\frac{d}{\sigma_s}\right), \tag{1.6}$$

where $F_0$ is the area under the curve at the right of $\frac{d}{\sigma_s}$.

Neglecting the elastic interactions between the asperities, all summits that exceed a height $d$ are deflected by an amount $w = z - d$, which is called the "penetration depth". According to the Hertzian theory the contact area for a sphere of radius $R$, deflected by a magnitude $w$ is given by

$$A = \pi R w = \pi R(z - d), \quad z > d, \tag{1.7}$$

and the corresponding load on the asperity is

$$P = \frac{4}{3}E' R^{1/2} w^{3/2} = \frac{4}{3}E' R^{1/2}(z - d)^{3/2}, \quad z > d, \tag{1.8}$$

in which $E'$ is defined as

$$E' = \frac{1}{(1-\nu_1^2)/E_1 + (1-\nu_2^2)/E_2}, \tag{1.9}$$

where $E_i, \nu_i (i = 1, 2)$ are the Young's moduli and Possion's ratio of the plane and the rough surface.

Defining $D_{sum}$ as the number of peaks per unit area, then the average number of micro-contacts in any unit area is given by

$$n = D_{sum} F_0 \left( \frac{d}{\sigma_s} \right). \tag{1.10}$$

Using the number of peaks per unit area and integrating the Hertzian deformation in the contact area ($d$ to $\infty$), we obtain the expected summit contact area and total normal load per unit area

$$\frac{A_c}{A_0} = \int_d^\infty D_{sum} f(z) \pi R (z-d) dz, \tag{1.11}$$

$$\frac{P}{A_0} = \int_d^\infty D_{sum} f(z) \frac{4}{3} E' R^{1/2} (z-d)^{3/2} dz, \tag{1.12}$$

where $A_0$ is the total area in contact. After normalizing for use of the standard normal curve, the ratios are translated to

$$\frac{A_c}{A_0} = D_{sum} \pi R \int_{d/\sigma_s}^\infty \left( x - \frac{d}{\sigma_s} \right) \phi(z) dx \tag{1.13}$$

$$= D_{sum} \pi R \sigma_s F_1 \left( \frac{d}{\sigma_s} \right), \tag{1.14}$$

$$\frac{P}{A_0} = \frac{4}{3} D_{sum} E' R^{1/2} \int_{d/\sigma_s}^\infty \left( x - \frac{d}{\sigma_s} \right)^{3/2} \phi(z) dx \tag{1.15}$$

$$= \frac{4}{3} D_{sum} E' R^{1/2} \sigma_s^{3/2} F_{3/2} \left( \frac{d}{\sigma_s} \right), \tag{1.16}$$

in which

$$F_1(t) = \int_t^\infty (x-t)\phi(x)dx, \tag{1.17}$$

$$F_{3/2}(t) = \int_t^\infty (x-t)^{3/2}\phi(x)dx. \tag{1.18}$$

To extend the model for the case of two lubricated rough surfaces the minimum film thickness must be known, together with the GW model parameters ($R, Dsum, \sigma_s$). The minimum film thickness $h$ is now the distance that separates the two surfaces. The roughness of both surfaces are combined computing the composite rms value

$$\sigma = (\sigma_1^2 + \sigma_2^2)^{1/2}. \tag{1.19}$$

With this new roughness parameter the contact of two rough surfaces is translated into a equivalent contact for a plane and a rough surface. The ratio $h/\sigma$ is known as the lubricant film parameter and is represented by $\Lambda$. For $\Lambda > 3$, the surface is considered well lubricated since few contacts are occurring between the surfaces. The rest of the GW model parameters are translated using the following expressions

$$D_{sum} = \frac{m_4}{6\pi m_2\sqrt{3}}, \tag{1.20}$$

$$R = \frac{3}{8}\sqrt{\frac{\pi}{m_4}}, \tag{1.21}$$

where $m_2$ and $m_4$ are the second and forth spectral moments of a profile $z(x)$ in an arbitary

direction $x$. The spectral moments are defined as

$$m_0 = E(z^2) = \sigma^2 \tag{1.22}$$

$$m_2 = E\left[\left(\frac{dz}{dx}\right)^2\right] \tag{1.23}$$

$$m_4 = E\left[\left(\frac{d^2z}{d^2x}\right)^2\right]. \tag{1.24}$$

Once calculated the contact ratio $A_c/A_0$ using the minimum film thickness, is possible to combine the friction losses due lubricant shearing and asperity contact in sliding friction as $\phi_{bl}$ in the SKF 4S model (Equation 1.2). Recently, it has been found that the model is not an accurate representation of the real contact [42, 43]. However, it is difficult to relate the new theory with measurements of surface roughness.

More detailed information about surface roughness contact and the lubricated contact of rough surfaces could be found in [44] and [45], the material in this section was based on the information found in these sources.

## 1.5 Curvature and Relative Curvature

For further analysis of ball bearings is necessary to define the curvature parameters of two revolution bodies of different curvature in contact at a single point, as in the case of the ball and raceway contact or for two balls in contact. This section is summarized from [1].

Consider the case of two balls in contact aligned in the vertical axis as shown in Figure 1.2, these are refereed as body I and body II. Moreover, consider two perpendicular planes that intersect at the vertical axis where the bodies are aligned, these are named plane 1 and plane 2. Therefore, we name the radius of curvature of body 1 in plane 2 as $r_{I2}$.

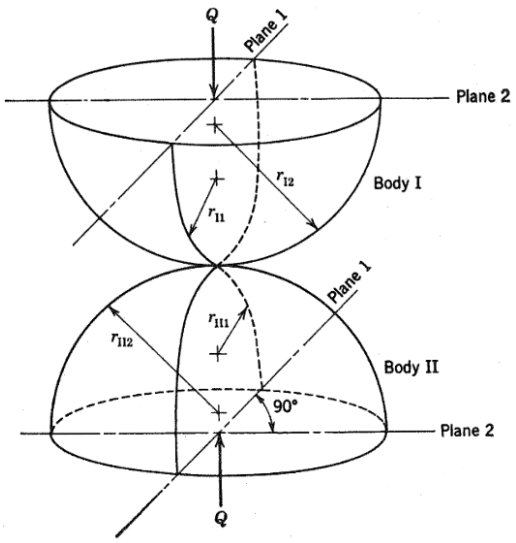


Figure 1.2: Revolution bodies in contact and curvature parameters (reprinted from [1], pag. 61)

Curvature is defined as

$$\rho = \frac{1}{r} \tag{1.25}$$

for concave surfaces the curvature sign is negative, while for convex surface the sign is positive. The radius of curvature is always positive.

The parameters to describe the contact between two revolution surfaces are:

1. Curvature sum:

$$\sum \rho = \frac{1}{r_{I1}} + \frac{1}{r_{I2}} + \frac{1}{r_{II1}} + \frac{1}{r_{II2}}. \tag{1.26}$$

2. Curvature difference:

$$F(\rho) = \frac{(\rho_{I1} - \rho_{I2}) + (\rho_{II1} - \rho_{II2})}{\sum \rho}. \tag{1.27}$$

It is important to respect the sign convention for convex and concave surfaces. The parameter $F(\rho)$ should always be positive.

## 1.6 Distribution of Internal Loading in Statistically Loaded Bearings

This section is a summary of the information found in [6]. The summary focus mainly on calculation of internal load distribution on ball bearings.

The internal load distribution of a statically loaded bearing determine the friction component en each ball. For a point contact (i.e. ball-raceway contact) the load $Q$ due a deformation $\delta$ is given by

$$Q = K\delta^{\frac{3}{2}}, \tag{1.28}$$

where $K$ for a steel ball in contact with a steel race is defined as

$$K = 2.15 \times 10^5 \left(\sum \rho^{-1/2}\right) (\delta^*)^{-3/2}, \tag{1.29}$$

and $\delta^*$ is a parameter to calculate Hertzian contact and could be found as function of curvature difference using Table A.1.

For a bearing under radial load and rigidly supported, the radial deformation of any ball located at a certain angular position $\psi$ is given by

$$\delta_\psi = \delta_r \cos\psi - \frac{1}{2}P_d, \tag{1.30}$$

in which $\psi = 0$ is the location of the ring radial shift $\delta_r$ and $P_d$ is the diametrical clearance. The maximum deformation $\delta_{max}$ that occurs at $\psi = 0$ could be used to rearrange Equation 1.30 as

$$\delta_\psi = \delta_{max}\left[1 - \frac{1}{2\epsilon}(1 - \cos\psi)\right], \tag{1.31}$$

where

$$\epsilon = \frac{1}{2}\left(1 - \frac{P_d}{2\delta_r}\right). \tag{1.32}$$

The diametrical clearance determine the extension of the load zone and could be ob-

tained by

$$\psi_l = \cos^{-1}\left(\frac{P_d}{2\delta_r}\right). \tag{1.33}$$

From Equation 1.28 we obtain

$$\frac{Q_\psi}{Q_{max}} = \left(\frac{\delta_{psi}}{\delta_{max}}\right)^{\frac{3}{2}} \tag{1.34}$$

and substituting Equation 1.31 into Equation 1.34,

$$Q_\psi = Q_{max}\left[1 - \frac{1}{2\epsilon}(1-\cos\psi)\right]^{\frac{3}{2}}. \tag{1.35}$$

Based on Equation 1.28 the maximum load could also be expressed as

$$Q_{max} = K\delta_{\psi=0}^{3/2} = K\left(\delta_r - \frac{1}{2}P_d\right)^{\frac{3}{2}}. \tag{1.36}$$

For a static equilibrium, the vertical components of the ball loads must equal the applied radial load on the ring

$$F_r = \sum_{\psi=0}^{\psi=\pm\psi_l} Q_\psi \cos\psi. \tag{1.37}$$

Substituting Equation 1.35,

$$F_r = K\left(\delta_r - \frac{1}{2}P_d\right)^{\frac{3}{2}} \sum_{\psi=0}^{\psi=\pm\psi_l}\left[1 - \frac{1}{2\epsilon}(1-\cos\psi)\right]^{\frac{3}{2}}\cos\psi \tag{1.38}$$

or in the integral form,

$$F_r = ZK\left(\delta_r - \frac{1}{2}P_d\right)^{\frac{3}{2}} J_r(\epsilon) \tag{1.39}$$

in which $Z$ is the number of balls and

$$J_r(\epsilon) = \frac{1}{2\pi} \int_{-\psi_l}^{+\psi_l} \left[1 - \frac{1}{2\epsilon}(1 - \cos\psi)\right]^{\frac{3}{2}} \cos\psi \; d\psi. \tag{1.40}$$

The integral could be calculated numerically or using Table A.2 to interpolate the desired value. Equation 1.39 could be solved iteratively for a given bearing with certain clearance and load. The process starts by assuming an initial $\delta_r$, then $\epsilon$ is obtained from Equation 1.32, the integral $J_r(\epsilon)$ is solved and the process repeats until Equation 1.39 is balanced.

Stribeck [46] approximate the following solution for the maximum load for the case when the ball bearing is under pure radial load and zero clearance.

$$Q_{max} = \frac{4.37 F_r}{Z \cos\alpha} \tag{1.41}$$

When nominal diametrical clearance is considered Equation 1.41 modifies to

$$Q_{max} = \frac{5 F_r}{Z \cos\alpha}. \tag{1.42}$$

Once the load and speed of each ball is calculated, Equation 1.3 could be used to to obtain the minimum film thickness $h$, which is the key to find the total friction moment $M_f$ of the bearing (Equation 1.1).

## 1.7 Ball Bearing Dynamic Model

The interaction of the bearing with the rest of the rotor behaves as a spring damper support for the lateral and axial motion and as a damper for the angular displacements. The damping effect in angular motion, as explained by EHL, GW, and SKF 4S models, depends on the load, speed and viscosity. In this section is developed the equation of

motion that represents the dynamics of a ball bearing.

Kramer [47] approximate the vertical stiffness $k_{vv}$ of the bearing as the slope of the nonlinear force-deflection relation, this could be used to simplify the bearing model in a rotor assembly. Assuming the static load is vertical, the horizontal stiffness $k_{uu}$ is proportional to the vertical stiffness. Kramer also find that the damping component ($c_{vv}$ or $c_{uu}$) is low in ball bearings and proportional to the stiffness component (vertical or horizontal). The dynamic parameters of the bearing for the lateral vibrations are shown here

$$k_{vv} = \kappa_b \, n_b^{2/3} \, D^{1/3} \, f_s^{1/3} \, \cos^{5/3} \alpha, \tag{1.43}$$

$$\frac{k_{uu}}{k_{vv}} = 0.46, 0.64, 0.73 \text{ for } 8, 12, 16 \text{ balls, respectively}, \tag{1.44}$$

$$c_{vv} = (0.25\text{~}0.5) \times 10^{-5} \times k_{vv}, \tag{1.45}$$

$$c_{uu} = (0.25\text{~}0.5) \times 10^{-5} \times k_{uu}, \tag{1.46}$$

where $n_b$ is the number of balls in the bearing, $f_s$ is the static force in the vertical direction and the constant $\kappa_b = 13 \times 10^6 (N^{2/3} m^{-4/3})$. The parameters are used to build the dynamic model of the bearing for three degrees of freedom $(x, y, \theta)$, the model is shown as

$$\begin{bmatrix} m_b & 0 & 0 \\ 0 & m_b & 0 \\ 0 & 0 & J_{zz} \end{bmatrix} \begin{Bmatrix} \ddot{u} \\ \ddot{v} \\ \dot{\omega} \end{Bmatrix} + \begin{bmatrix} k_{uu} & 0 & 0 \\ 0 & k_{vv} & 0 \\ 0 & 0 & 0 \end{bmatrix} \begin{Bmatrix} u \\ v \\ \theta \end{Bmatrix} + \begin{bmatrix} c_{uu} & 0 & 0 \\ 0 & c_{vv} & 0 \\ 0 & 0 & 0 \end{bmatrix} \begin{Bmatrix} \dot{u} \\ \dot{v} \\ \omega \end{Bmatrix}$$
$$= \begin{Bmatrix} f_x \\ f_y \\ \tau - M_f(f_x, f_y, \theta, \omega) \end{Bmatrix}. \tag{1.47}$$

The effect of the EHL lubrication on the dynamics of deep groove ball bearing was investigated by Wijnant et al. [48], it was found that in the presence of lubricant could be

modeled as a spring-damper system. These parameters could be added to the components of the stiffness and damping matrix. A complete review over bearing and rotor dynamics is provided by Friswell in [49].

## 1.8 Effect of Interference on Clearance

Clearance is the distance that the inner ring could move with respect to the outer ring. The distance is composed by the axial internal clearance and the radial internal clearance. A method to reduce clearance of bearing components is to increase the interference between the outer ring and the housing or between the inner ring and the shaft.

The effect of interference on the clearance is modeled using the elastic thick ring theory. Consider a shaft of diameter $D_S$ assembled with a bearing of same bore diameter at a specified interference $I_S$ as shown in Figure 1.3. The inner ring of initial external diameter $d_i$ will expand reducing the radial internal clearance a distance $\Delta_S$. Assuming a solid shaft the change in clearance $\Delta_S$ could be approximated by

$$\Delta_S = \frac{2\, I_S \left(\frac{D_1}{D_S}\right)}{\left[\left(\frac{D_1}{D_S}\right)^2 - 1\right]\left\{\frac{\left(\frac{D_1}{D_S}\right)^2+1}{\left(\frac{D_1}{D_S}\right)^2-1} + \xi_b + \frac{E_b}{E_S}\left[\left(\frac{D_S}{D_1}\right)^2 - \xi_S\right]\right\}}, \tag{1.48}$$

where the Young's moduli and the Poisson ratio are represented by $E$ and $\xi$ respectively.

Now consider the case of interference between a bearing housing of diameter $D_h$ assembled with a bearing of same outer diameter with a specified interference $I_H$ as shown in Figure 1.4. In this case the outer ring of internal diameter $d_o$ will contract and decrease the radial internal clearance by a distance $\Delta_H$. Assuming the housings outer diameter

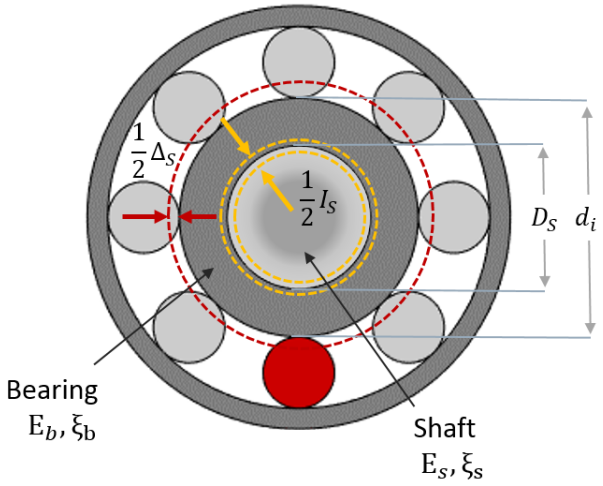


Figure 1.3: Inner interference and change in clearance

approaches infinity the clearance change could by approximated by

$$\Delta_H = \frac{2\, I_H \left(\frac{D_h}{D_2}\right)}{\left[\left(\frac{D_h}{D_2}\right)^2 - 1\right]\left\{\frac{\left(\frac{D_h}{D_2}\right)^2+1}{\left(\frac{D_h}{D_2}\right)^2-1} - \xi_b + \frac{E_b}{E_h}\left[1+\xi_h\right]\right\}}. \tag{1.49}$$

## 1.9 Common Bearing Fault Indicators

The characteristic signatures for bearing faults were presented by Tandon and Choudhury [50]. These signatures are used to diagnose localized cracks or spalls (metal breaking away from the raceway due to surface fatigue) in the raceways, rollers, or defects in the cage. Assuming the bearing components are rolling without slipping and that the outer

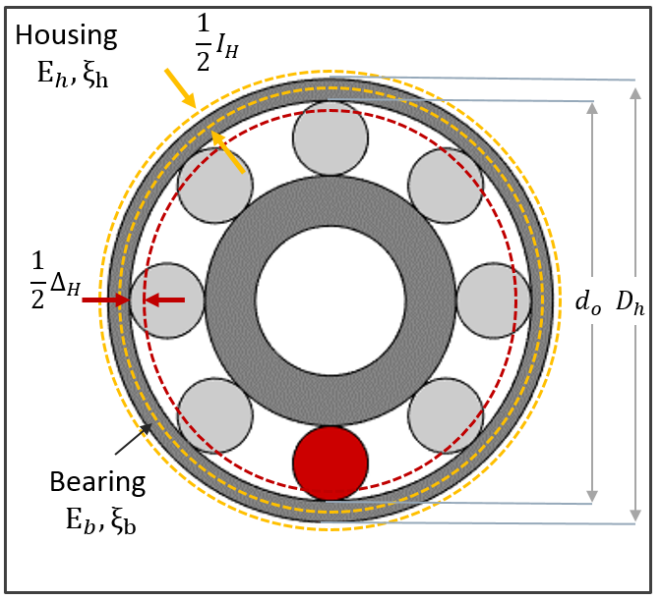


Figure 1.4: Outer interference and change in clearance

race is fixed, the characteristic frequencies are

$$FTF = \frac{\omega}{2}\left(1 - \frac{D\ \cos\alpha}{d_m}\right), \tag{1.50}$$

$$BSF = \frac{d_m}{D}\left(\frac{\omega}{2}\right)\left[1 - \left(\frac{D\ \cos\alpha}{d_m}\right)^2\right], \tag{1.51}$$

$$BPFI = n_b\frac{\omega}{2}\left(1 + \frac{D\ \cos\alpha}{d_m}\right), \tag{1.52}$$

$$BPFO = n_b\frac{\omega}{2}\left(1 - \frac{D\ \cos\alpha}{d_m}\right), \tag{1.53}$$

where $\omega$ represents the angular speed of shaft, $D$ the ball diameter, $\alpha$ the contact angle, $d_m$ the pitch diameter, $n_b$ is the number of balls in the bearing.

For a fault localized at the train or cage the FTF frequency will appear in the vibration spectra and for the case of a fault located in the surface of a ball is expected a vibration signal of frequency $2 \times BSF$ with and amplitude modulated by the FTF. In the case of a

defect located at the inner or outer raceway, the ball pass frequency of inner ring (BPFI) or ball pass frequency of outer ring (BPFO) will appear in the spectra. The BPFI signal will be amplitude modulated by the load zone, since the impacts will increase in magnitude when the defect enters the load zone

These four frequencies are critical to diagnose bearing problems in a rotating machine. The origin of these frequencies is an impulse response created each time the spall or local defect is hit by a ball. The frequency of the impulse response is for all cases the natural frequency of the bearing-housing assembly, but the frequencies at which these hits occurs are the ones specified by Tandon and Choudhury.

Before describing the diagnosis methods used for rolling bearings is necessary to first the describe detection or screening methods. Some of the most common indicators are high frequency RMS [51], Crest Factor (CF), and Kurtosis [52].

### 1.9.1 RMS

RMS is used to measure the energy content of a signal, this is one of the most common vibration indicators [3]. ISO 10816-1 [51] uses the RMS value of vibration velocity to specify the range of recommended vibration limits for rotating machines of different types. Moreover, RMS can characterize the intensity of the signal.

$$x_{rms} = \sqrt{\frac{1}{T_2 - T_1}\int_{T_1}^{T_2}[x(t)]^2 dt} \;\Rightarrow\; \sqrt{\frac{1}{N}\sum_{n=1}^{n}|x_n|^2} \tag{1.54}$$

### 1.9.2 Crest Factor

Crest Factor (CF) is the ratio between the absolute-maximum peak value and the RMS value of a given waveform, the value for a sinusoidal signal is 1.414. This indicator is good for initial faults but it has been shown that Crest Factor decreases as the fault increases [52].

$$CF = \frac{|x|_{peak}}{x_{rms}}. \tag{1.55}$$

### 1.9.3 Kurtosis

Kurtosis is a statistical analysis called “fourth moment" and is a measure of the tails on a distribution (Equation 1.56). Kurtosis value of a normal distribution is 3. Kurtosis has been used as fault indicator for more than 30 years [53] and Pachaud [54] shows that kurtosis is a more sensitive indicator than CF but also is highly sensitive to noise. Due the noise sensitivity kurtosis requires a pre-treating process. Kurtosis could also be defined as the “fourth cumulant” or the excess kurtosis, which is computed by subtracting 3 from Equation 1.56.

$$Kurt = \frac{E\left(x-\mu\right)^4}{\sigma^4} \Rightarrow \frac{\frac{1}{n}\sum_{i=1}^{n}(x_i-\overline{x})^4}{\left(\frac{1}{n}\sum_{i=1}^{n}(x_i-\overline{x})^2\right)^2} \tag{1.56}$$

### 1.9.4 Spectral Kurtosis, Kurtogram and Fast Kurtogram

This section is based on [2], that explains in a simple form the Spectral Kurtosis, Kurtogram, and Fast Kurtogram.

Spectral Kurtosis (SK), which was introduced by Dywer in 1983 [55], is a tool to find the frequency bands with the highest content of impulsivity. SK is based on a time-frequency domain transformation function $H(t, f)$ as the Short Time Fourier Transform (STFT) or Wavelet Analysis [56]. The kurtosis is calculated at each frequency $f$ by taking the average of fourth power of $H(t, f)$ at each time and then normalize it by the square of the mean square value. By subtracting two from this ratio the results is zero for a Gaussian

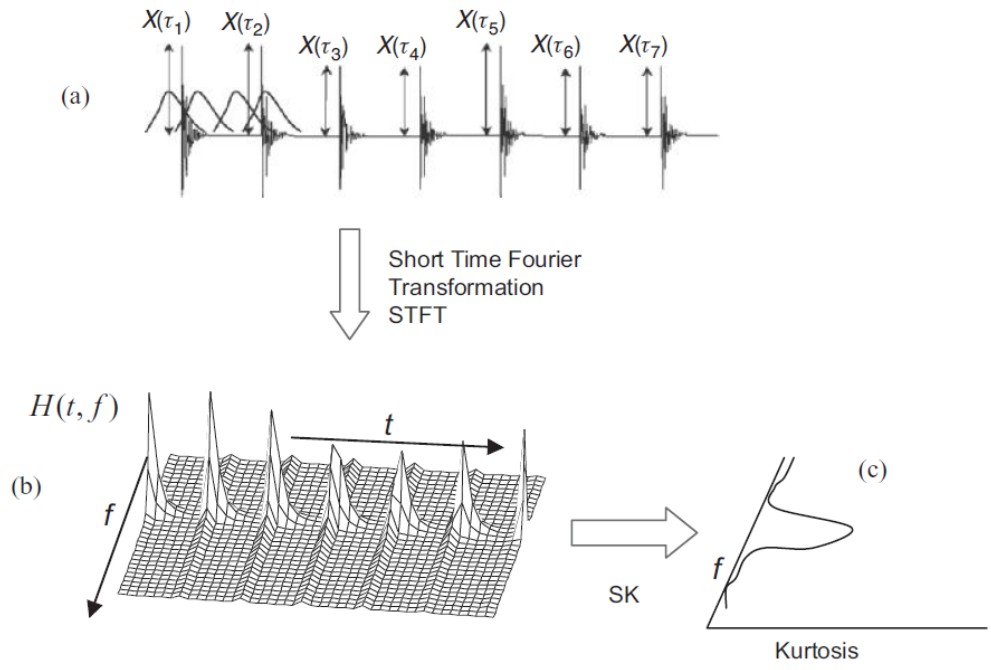


Figure 1.5: Calculation process of spectral kurtosis. (a) Simulated bearing fault; (b) STFT; (c) SK as a function of frequency (reprinted from [2], pag. 173)

signal as given by

$$K(f) = \frac{\langle H^4(t,f)\rangle}{\langle H^2(t,f)\rangle^2} - 2. \tag{1.57}$$

In Figure 1.5 is shown the process to obtain the SK for a simulated fault in a ball bearing, where $X(\tau_k)$ represent the impulses at times $\tau_k$ followed by the impulse response of the system.

The frequency bands with high value of kurtosis are used to filter the signal and extract the part dominated by impulses from the part dominated by stationary components. The problem with SK is that do not provided information of the best band-width for the filter and it requires an iterative procedure to find the optimal results. A map could be used where the SK is calculated for range of bandwidths, this map is called 'Kurtogram'. For the case of the STFT the bandwidths are directly related to the window length $N_W$ which

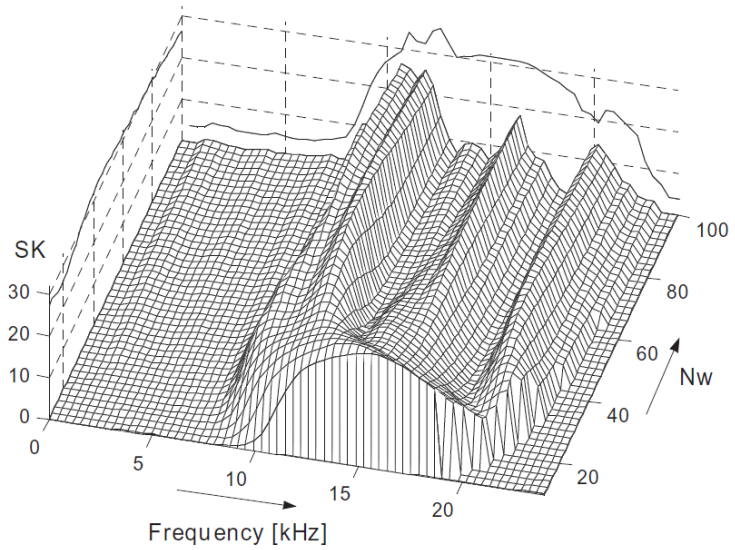


Figure 1.6: Kurtogram of simulated bearing fault with noise content (reprinted from [3], pag. 326)

defines the spectral resolution as shown in Figure 1.6.

The disadvantage of this method is computation time; is expensive for online systems. One solution for this problem is called 'Fast Kurtogram' (FK) and was presented by Antoni in 2007 [57]. The technique is based on a series of digital filters instead of time-frequency analysis and the decomposition of the signals is based in a dyadic decomposition similar to the discrete wavelet packet transform.

The FK creates a map where one of the axes is a progressive split of the frequency range in bands and the other axis is the center frequency of the band. Is recommended to do it with a 1/3-binary tree where the division is a sequence of $1/2, 1/3, 1/4, 1/6, 1/8$, and so on. FK is commonly used to select the best filter bandwidth for the signal together with Spectral Coherence [12]. Figure 1.7 shows the comparison between the FK and the kurtogram.

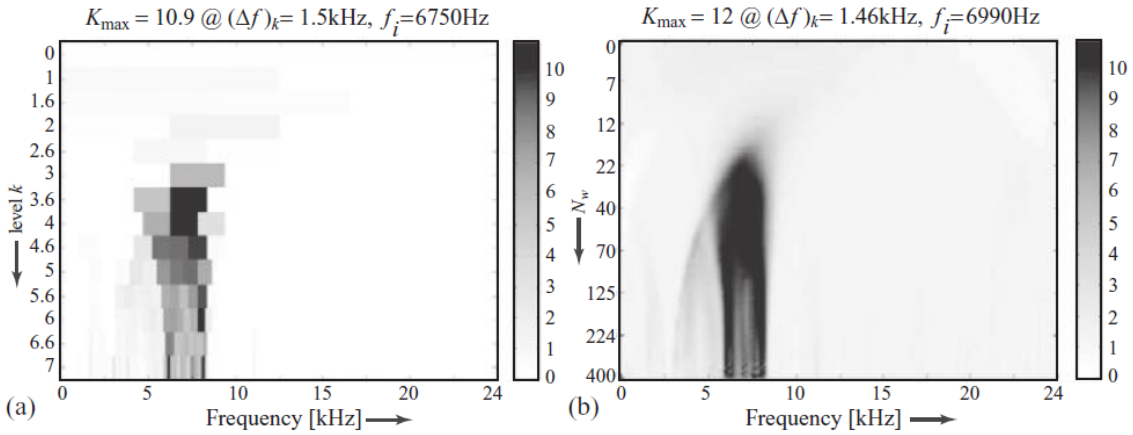


Figure 1.7: Comparison between FK and Kurtogram (reprinted from [2], pag. 178)

### 1.9.5 Envelope Analysis

Envelope analysis has become the 'benchmark method for bearing diagnostics' [58]. To apply this method is necessary to filter the high frequency band that amplifies the fault impulses, as mentioned before this frequency band is the structural frequency of the housing and bearing assembly. After the filtering procedure, the amplitude is demodulated using the Hilbert transform to obtain the envelope of the signal. The envelope contains information about the frequency of impact repetition and the modulation due the load zone (Figure 1.8).

The Hilbert transform relates the imaginary and real part of a one-sided function [59] and for a time signal is defined as

$$\overline{x}(t) = \frac{1}{\pi} \int_{-\infty}^{\infty} x(\tau) \frac{1}{(t-\tau)} d\tau. \tag{1.58}$$

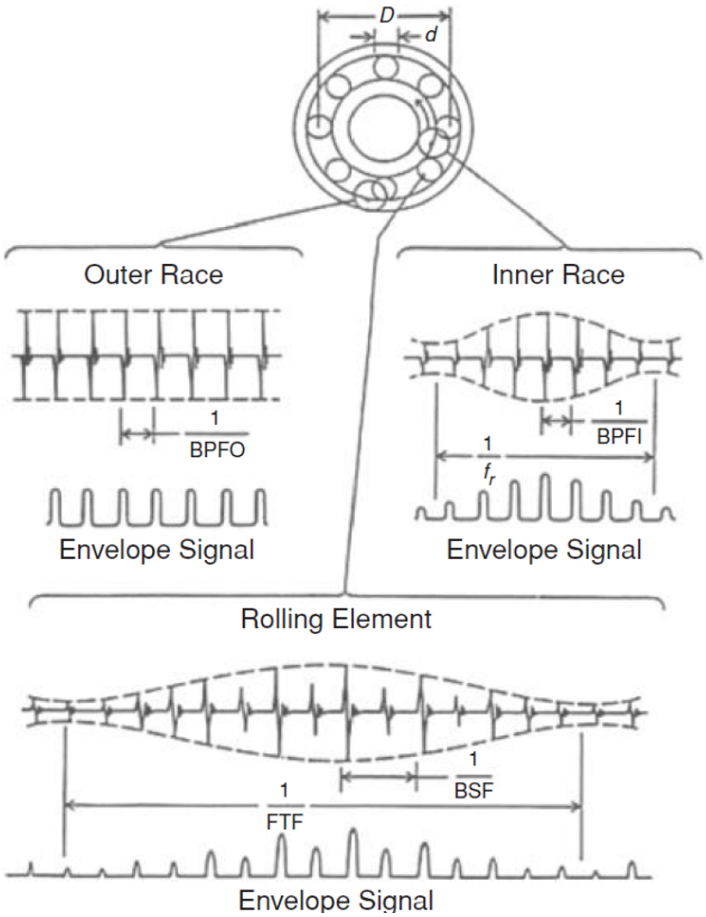


Figure 1.8: Envelope analysis (reprinted from [2]), pag. 49

Using the time signal as the real part of a complex valued signal and the Hilbert transform as the imaginary part is obtained the known 'Analytic Signal'

$$X(t) = x(t) + j\overline{x}(t). \tag{1.59}$$

which could also be expressed as a rotating vector in the complex plane with amplitude and frequency modulation.

$$X(t) = A(t)e^{j(\omega t + \phi(t))}. \tag{1.60}$$

where $\omega$ is the carrier frequency of the time signal, $\phi(t)$ is the frequency modulation and $A(t)$ is the amplitude modulation that includes a DC offset to avoid negative values. By obtaining the analytic signal of the timed function is possible to demodulate the amplitude by computing the magnitude of the analytic signal and hence obtain the envelope.

To simplify the Hilbert transform operation is possible to obtain the Fourier Transform (FT) of Equation 1.58 (that is a convolution operation), solve in the frequency domain (Equation 1.61), and return to the time domain using the Inverse Fourier Transform (IFT).

$$\overline{X}(f) = X(f)(-j\ sgn(f)) \tag{1.61}$$

After obtaining the envelope or magnitude of the Analytic Signal, is necessary to obtain the Fourier Transform to extract the frequency of the interval between impacts. The main frequency is then compared to the characteristic frequencies (Equations 1.50, 1.51, 1.52, 1.53) to identify the faulty component.

### 1.9.6 Order Tracking

To use envelope analysis in situations where the speed shaft is fluctuating or in a transitory state, a technique called order tracking could be used. In rotating machinery when the signal is sample at a fixed time and the shaft speed is fluctuating a smearing of discrete frequencies occurs in frequency domain. To avoid this problem is desirable to use order tracking, which changes the x-axis from frequency to orders or harmonics of shaft speed. With this technique any signal that is synchronous of shaft speed will be a discrete peak or line in the spectrum, as in the case of the characteristic frequencies. Order tracking is obtained by re-sampling the signal using a tachometer or encoder to generate a sampling signal synchronous to shaft speed.

## 1.10 Review of Lateral Vibrations Measurement Techniques

Lateral vibrations are oscillations which could be measured by distance, velocity and acceleration transducers. In some applications where the vibrations modes are important for condition monitoring the strain gauges could be used. Distance is usually measured by proximity probes which measure a relative value. For journal bearings these sensors are installed on the stator to monitor the vibrations of the shaft and detect problems on the rotor.

Velocity and Acceleration transducers measure absolute values, which are more proportional to the forces applied on the rotor compared to the proximity probes. Velocity is directly related to the energy hence to the stress suffered by the machine. That is the main reason why the standards are based on velocity units (ISO 10816). The problem with velocity transducers is that they are heavier than accelerometers hence they could affect the measured mass and hence the natural frequency.

The most common accelerometer transducer is based on a piezoelectric crystal and they could either have an integrated amplifier or just output the raw signal, which requires to have a signal conditioning module. Velocity measurements could be obtain by integrating the accelerometer signal, but is recommendable to first use a high-pass filter to eliminate the DC or mean value component that generates drift. Accelerometers are light and robust, hence they are the best option for vibration-based condition monitoring.

Recently the increase on MEMS (Microelectromechanical systems) sensors technology has decrease the cost of MEMS-based accelerometers to the point that most modern cellphones have one integrated. This development is reaching the industry standards and now is possible to find high-frequency accelerometers powered by batteries and with the signal processing embedded in the same sensors. The low cost and advantages of these new accelerometers will benefit the condition monitoring sector by allowing to perma-

nently install the sensors on all critical equipment,collect the data via wireless transmission, and allow the experts to remotely diagnose the machines that presents high-level of vibrations.

With the development of optics, the use of lasers is impacting all fields including vibration measurements. This method measures velocity based on the Doppler phase shift of a laser beam when is reflected from a moving surface. This method provides the advantage of measuring different points on a machine from a far distance in a matter of seconds. The current disadvantage is the high-cost of the equipment, but is expected that in a near future the technology will be accessible for a low-cost and in a small device.

A new technology that is being used to measure lateral vibrations is the vibration image camera, which is a high-speed camera. When the frame rate is synchronized with one of the vibration modes or the rotation frequency is possible to visualize the vibration effects and measure the vibration displacement levels. The disadvantages of this technology is the high cost and that the measurements are affected by the vibrations on the camera.

## 1.11 Review of Torsional Vibrations Measurement Techniques

Torsional vibrations are hard to measure in rotor-machinery since these are angular oscillations in the shaft along the axis of rotation. One of the most traditional methods to measure torsional vibrations is through strain gauges attached to the shaft measuring at $45°$. The data is transmitted through wireless devices or slip-rings . These provide a high accuracy but it has problems as the high cost of installation, wearing of slip-rings, low-batteries and corruption of the raw signals when there is an electric motor.

Torque oscillations could also be used to measure torsional vibrations. By measuring the angular deflection of a shaft of known properties is possible to obtain the torque. The disadvantage is that the sensor should be mounted in between a shaft section, which is feasible only for a permanent condition monitoring systems.

Other methods use a non-contact sensor (magnetic, optical, capacitive) and a shaft incremental encoder (toothed-gear, magnetic strip, zebra tape) [60]. When a shaft is rotating without torsional vibrations the sensor generates a periodic signal with no modulation, this is called the carrier signal. Depending of the type of sensor and electronics the signal could be sinusoidal or squared. Under torsional vibrations the frequency of the carrier signal is modulated and for the case of sinusoidal signals the amplitude is also modulated. Some methods that use the modulation are the Frequency Modulation (FM), Amplitud Modulation (AM) and the SideBands.

The time interval measurement system (TIMS) is a method that measures the time period of each pulse on the encoder using a high frequency clock to calculate the instantaneous shaft speed '$\omega$'. Vance [61] introduce this method in 1986 by using a zebra tape attached to the rotor and a optic transducer as an encoder. A digital circuit at 10Mhz was used to count the number of clock cycles over a pulse period. When the clock cycles are used as reference the speed is obtained by

$$\omega = \frac{d\theta}{dt} = \frac{2\pi/N}{T_{clk} \times n_C} \left( \frac{rad}{s} \right), \tag{1.62}$$

where $N$ is the number of pulses per revolution (ppr), $n_c$ is the counted number of clock cycles, and $T_{clk}$ is the clock period which is the inverse of clock frequency $f_c$. Since the obtained digital speed is not timed-sampled but instead is sampled by the angular position this is known as 'Synchronous or Angular Sampling' , which is the same as performing order tracking on a time-sampled signal, but with a higher resolution. The advantage of synchronous samplings is that by directly computing the FFT on the synchronous signal, the spectrum is in the order-domain.

Synchronous sampling has the problem of aliasing, Nyquist ratio is defined as $ppr/2$, the problem with this method is that there is no spatial filters to avoid aliasing so an encoder

with sufficient ppr should be used. Schomerus in his tesis [60] identify a number of noise sources when using TIMS and geometrical imperfect encoder, in his results he proposed the use of high frequency counters to reduce noise.

Laser Torsional Vibrometer (TLV) is based on the Doppler effect and it uses two lasers beams directed to the rotating shaft. The advantage of this method is that is non-contact, the cross-section shaft shape could not be circular and provides high accuracy measurements. The disadvantages are the current high-cost and the high noise level due the speckle noise [62].

Another common method for situations where encoders or strain gauges could not be used is to estimate either the torque or the speed. The speed and torque could be estimated using the current and voltage on the motor that drives the rotor and a model that contains the dynamics of the rotor [63–68].

Table 1.1 summarizes some of the most relevant works related to torsional vibration measurement techniques. Attention was focused on the type of technique which could be classified in two groups, contact and non-contact techniques. Other important aspects considered in this review were the velocity of the motor used in the experiments, if load change was evaluated and if the test was performed in transient or steady-state. A brief explanation of the purpose of the documents is presented to clarify the intentions of the author.

Table 1.1: Review of torsional vibrations measurement techniques.

| Cite | Vibration measurement technique | Transducer category | Contact | Year | RPM | Variable Load | Transient or steady-state | Purpose |
|---|---|---|---|---|---|---|---|---|
| [64] | Electronic model analog to torsional dynamics | Pressure Voltage and Current. | Yes | 1980 | 1500-3000 | Yes | Both | Monitor the mechanical impact of all electrical disturbances and predict fatigue accumulation and expected life. |
| [61] | FM AM Sidebands TIMS | Strain gauges proximity probe magnetic zebra tape and optical sensor | Yes | 1986 | 2500 | No | Both | Comparison and recommendations between techniques and introduction to TIMS method. |
| [69] | TIMS variation | Zebra tape and optical sensor | Yes | 1992 | 20-3400 | No | Steady-state | To measure vertical and horizontal vibration and uncouple it from torsional. |
| [70] | Laser Doppler Velocimetry | Laser | No | 1994 | - | No | Steady-state | Measurements of lateral vibrations, considering scattered light. The effect in measurements due speed variations or torsional vibrations is also addressed. |
| [71] | Laser torsional vibrometer | Laser | No | 1996 | - | Yes | Steady-state | Development of a laser torsional vibrometer. |

Continuation of Table 1.1

| Cite | Vibration measurement technique | Transducer category | Contact | Year | RPM | Variable Load | Transient or steady-state | Purpose |
|---|---|---|---|---|---|---|---|---|
| [72] | TLV | Laser | No | 1999 | 750 | No | Steady-state | The instrument's measurable sensitivity to angular lateral vibration is examined. A pure torsional vibration measurement and bending vibration are evaluated. |
| [65] | Torque estimation | Proximity sensor Torquemeter | Yes | 2003 | - | Yes | Transient | Development of a new innovative concept for a monitoring system which solves the problems of previous monitoring systems. |
| [66] | Extended state observer | Tacometer, Torquemeter | Yes | 2006 | - | Yes | Both | First time a ESO and LQ was used to control torsional vibration of the main drive system of a rolling mill. |
| [73] | TLV | Laser, Torque Sensor | No | 2006 | 50-500 | No | Steady-state | Measurement of torsional vibration using laser Doppler technology for torque estimation. |
| [60] | TIMS | Proximity probe Magnetic Zebra tape Optic sensor | Yes | 2007 | 300-2300 | No | Both | Develop and test different error reducing techniques in order to eliminate the noise generated in measuring torsional vibration using the TIMS method. |

Continuation of Table 1.1

| Cite | Vibration measurement technique | Transducer category | Contact | Year | RPM | Variable Load | Transient or steady-state | Purpose |
|---|---|---|---|---|---|---|---|---|
| [67] | Electromagnetic torque estimator | Voltage and current sensor | No | 2008 | 1500 | Yes | Steady-state | Measure only the phase voltage and currents in order to compute the electromagnetic torque without knowing any information about the drive system configuration. |
| [74] | TLV | Laser | No | 2012 | - | No | Steady-state | Use the laser torsional vibrometer to measure the torsional vibration of a shaft of a turbo generator under electrical network impact. |
| [68] | Torsional stress level amplitude estimation | - | No | 2014 | 91 | - | - | Two estimation methods to calculate the natural torsional vibration mode of marine power transmission system. Development of a simple method to estimate the torsional stress level. |
| [62] | Various | TLV<br>Angular accelerometer<br>Encoders<br>Optical sensor with zebra tape<br>Inductive | Both | 2014 | 1200 | No | Steady-state | Comparison of noise-floor levels of various sensors. |

## 1.12 Energy Efficiency

Lubrication starvation is a problem that decreases the remaining life time of the bearing but also impacts the energy efficiency of the machine. The increase of friction will require more energy at the input to compensate the energy dissipated as heat in order to maintain the same operation conditions. The efficiency of the machine is a ratio that represents how effective is a machine to transfer all the energy at the input to the output. Equation 1.63 shows how to calculate the efficiency $\mu$ in an electrical machine. For the case of an induction motor the electrical power at the input $P_{in}$ is calculated by measuring the voltage $V(t)$ and current $I(t)$, while the mechanical power output $P_{out}$ could be obtained by measuring the torque $\tau(t)$ and the shaft speed $\omega(t)$.

$$\mu = \frac{P_{in}\left(V(t), I(t)\right)}{P_{out}\left(\omega(t), \tau(t)\right)} \tag{1.63}$$

An accurate method to obtain the electrical power input of a three phase motor is to calculate the RMS of the instantaneous power (Equation 1.64) in each voltage line and add them to obtain the total electrical power input (Equation 1.65). The power on each line and the total power input are described as

$$P_l = \frac{1}{T}\int_{-\frac{T}{2}}^{\frac{T}{2}} V_l(t) \cdot I_l(t) \cdot dt, \quad l = a, b, c\,, \tag{1.64}$$

$$P_{in} = P_a + P_b + P_c, \tag{1.65}$$

where $T$ is the period of the synchronous frequency or an integer multiple this period. It is important to remark that $V_i$ represents the voltage from the line to neutral. When the voltage is measured line to line is necessary to transform it to voltage line to neutral. Assuming balanced voltage from the phasor diagram shown in Figure 1.9 it is possible to observe that the voltage from line to line $V_{l-l}$ lags $30^\circ$ the voltage line to neutral $V_l$ and the

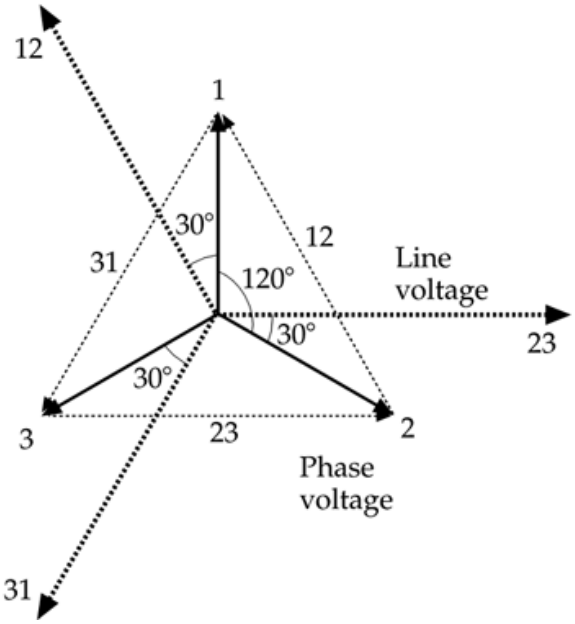


Figure 1.9: Phase diagram (reprinted from [4])

magnitud is scaled by a factor of $\frac{1}{\sqrt{(3)}}$. The transformation equations are shown as

$$V_a = \frac{V_{ab}^{\angle \phi_a - 30^\circ}}{\sqrt{(3)}} \tag{1.66}$$

$$V_b = \frac{V_{bc}^{\angle \phi_b - 30^\circ}}{\sqrt{(3)}} \tag{1.67}$$

$$V_c = \frac{V_{ca}^{\angle \phi_c - 30^\circ}}{\sqrt{(3)}}. \tag{1.68}$$

The mechanical power output is calculated by the R.M.S of the instant power and is given by

$$P_{out} = \frac{1}{T_s} \int_{-\frac{T}{2}}^{\frac{T}{2}} \omega(t) \cdot \tau(t) \cdot dt, \tag{1.69}$$

where $T_s$ in this case is the period of one shaft turn or an integer multiple of turns. It is important to use the same units as electrical power input (watts or HP) to avoid any problem.

# 2. EXPERIMENAL SETUP

The experimental setup is separated in three sections. The first sections describes in detail the development of the TIMS (Time Interval Measurement System) sensor and the preliminar test-bench used to test the sensor. The second section focus on the main test-bench located at Texas A&M University. The test-bench has the necessary components to control the critical parameters for experiments of lubrication starvation.The last section deals with the upgrades to the test-bench for the study of lubrication starvation effects on energy efficiency.

## 2.1 TIMS Sensor Development

During the literature review the most common method for measuring torsional vibrations was found to be the TIMS method or similar methods. The TIMS method requires only an encoder and a circuit that counts the number of clock cycles between pulses of the encoder. Some signal condition and software interface are added to complement the TIMS system. Figure 2.1 shows the overall parts of the TIMS systems.

One of the requirements of the TIMS method is to have an encoder with high number of pulses per revolution to avoid spatial aliasing as described in Section 1.11. The selected

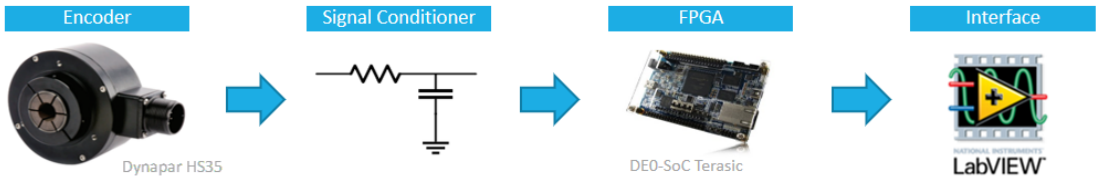


Figure 2.1: General description of TIMS system

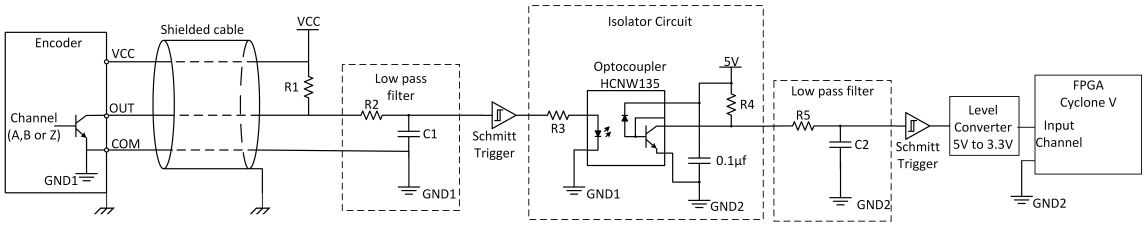


Figure 2.2: Signal conditioner circuit for the coupling between the encoder output and the FPGA input

encoder[1] has 2400 ppr and is a relative encoder with A, B and Z outputs while the selected FPGA[2] has a clock source of 50 MHz that could be increased uo to 200 MHz through a Phase Locked Loop (PLL) module. The parallel architecture of the FPGA is capable of acquire high speed signals and perform parallel tasks without the risk of missing encoder pulses as in the case of microcontrollers that perform tasks in a serial structure.

The complete circuit that couples one of the channels of the encoder with the FPGA is shown in Figure 2.2. In the first section of the circuit is shown the encoder output, which is an open collector configuration. The resistor used in the open collector should limit the current that circulates through the transistor according to the manufacturer specifications. Since the direction of rotation is not important for torsional vibration measurements the TIMS method could use either output A or B. The output Z is used to calculate a RMS speed measurement that is displayed through a LCD.

To attenuate high frequency perturbations as the one induced by the Variable Frequency Drive (VFD) a low-pass filter is used. The cut-off frequency $f_c$ must be calculated above the signal frequency produced by the encoder under a shaft speed $\omega$ (Hz), as shown here

$$f_c = \frac{1}{2\pi R_1 C_1} > ppr * \omega. \tag{2.1}$$

[1]Dynapar HS35

[2]Cyclone V embedded in a DE0-Nano-SoC kit

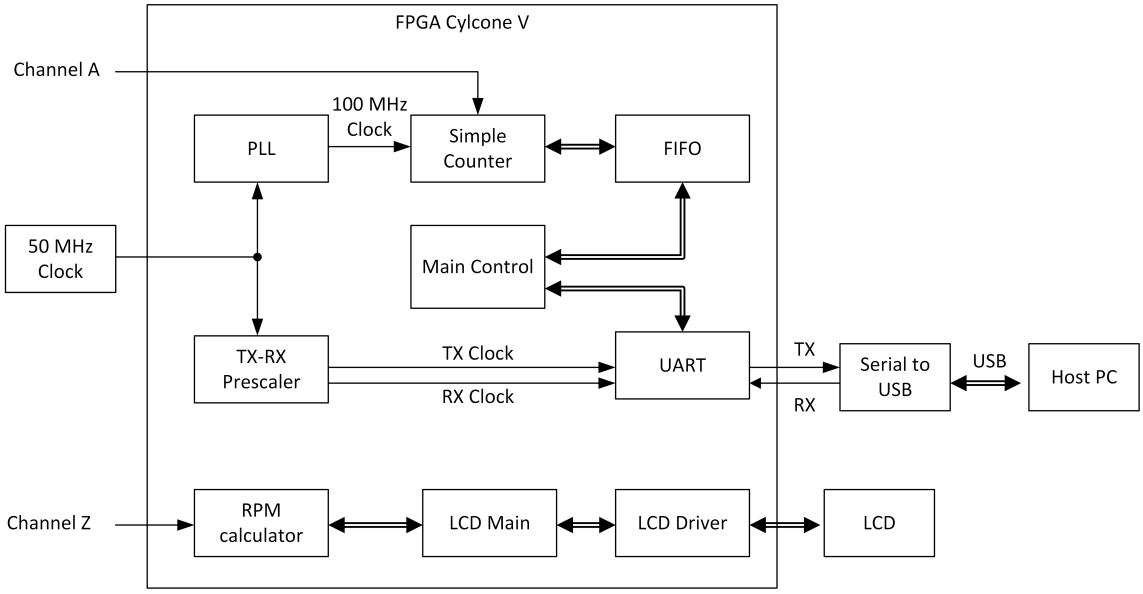


Figure 2.3: FPGA program structure

The output of the filtered signal is connected to a Schmitt trigger to generate a square pulse since the low pass filter attenuates the high frequency components of the original square signal. An opto-coupler is used to isolate the encoder from the FPGA, the circuit HCNW135 is used due the high bandwidth. During the transition of voltages the opto-coupler induces a high frequency oscillation at the mid-voltage region that is detected as a change of state in the FPGA. A low-pass filter is used at the output to eliminate this problem before inputing the signal to the rectifier that creates a TTL 5V signal. Finally the signal is sent to a voltage convertor that adapts the voltage from TTL 5V to 3.3V, which is the operating voltage of the FPGA.

The FPGA program is structured as shown in Figure 2.3. The Phase Loop Lock (PLL) duplicates the clock cycle from 50MHz to 100MHz in order to increase the resolution of the TIMS sensor. This new clock signal is used by the the acquisition module called *simple counter* which is always counting the number of cycles between the rising edges of the input signal (Channel A or B). Inside the simple counter module the counter is increased

in the rising edge of the input clock and during the negative edge the condition for end of period is evaluated to output the final count in a buffer and trigger the write requirement signal. The write requirement signal is enabled or disabled by the main module that controls the flow of data from the simple counter to the FIFO.

The FIFO is capable to store 16 bit words and a total of 131072 registers which are the number of pulses that could be stored in the FPGA. Increasing the size of the word allows to acquire slow speeds without overflowing the counter, after overflowing the counter the shaft is considered to be stopped. The minimum speeds that could be acquired by the sensor is

$$\omega_{min} = \frac{f_{clk}}{2^n * ppr}, \tag{2.2}$$

where $f_{clk}$ is the clock frequency and. $n$ is the number of bits in the word. The total number of registers $n_{FIFO}$ divided by the $ppr$ of the encoder defines the total number of shaft turns that could be acquired by the sensor. As an example for the case of 2400 ppr we have

$$N_{turns} = \frac{n_{FIFO}}{ppr} = \frac{131,072\ (pulses)}{2,400 \frac{pulses}{revolution}} = 54.61\ turns. \tag{2.3}$$

In order domain analysis, the number of turns acquired determines the spectrum resolution (lines between orders) and the number of registers is usually fixed once the firmware is downloaded to the FPGA. This limitation implies that to increase the order resolution is convenient to reduce the $ppr$ via an algorithm inside the FPGA, as long as the spectrum of interest is below $ppr/2$ (nyquist ratio). For this reason the TIMS sensor includes a divisor controlled by a DIP switch that allows to divide the ppr by 2, 4 or 8. Decreasing the ppr also increases the maximum and minimum speed that could be sampled by the sensor. It could be observed that the TIMS method is not adequate for cases where the rotational speed is slow but the torsional vibrations are in the high frequency range.

The UART module is in charge of receive and send bytes using the RS-232 commu-

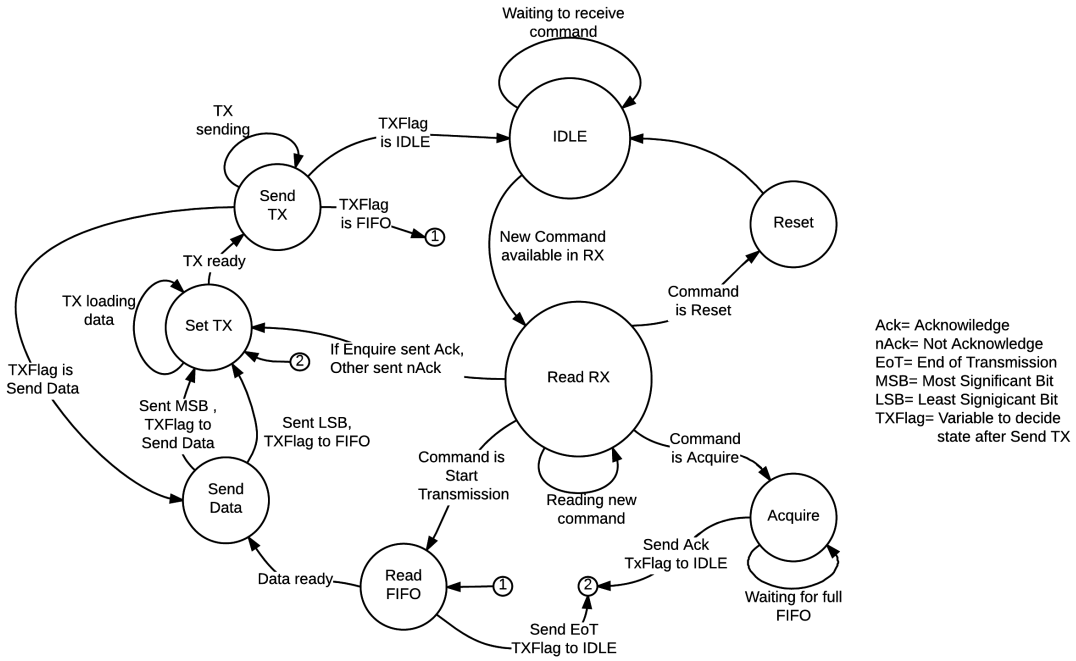


Figure 2.4: State machine for main control module. IDLE is the initial state.

nication protocol. The receiver (RX) and transmission (TX) modules work in parallel and each module has its own transmission clock which is generated in the pre-scaler module. The receiver module will trigger a flag each time new data is available while the transmission module will send any data in the buffer when the enable flag is triggered by the main control.

The main control module is in charge of the communication protocol using the UART module to transmit and receive data from a host and also is in charge to write or read the data in the FIFO. A state machine is used to manage all the tasks of the module as shown in Figure 2.4. Each of the states is designed to perform a specific task during the rising edge of the clock while during the falling edge, the transition for the next state or states is computed. The tasks performed by the states are described in detail:

- *Idle*: This is the initial state of the module. During this state the module monitors

the flag of the receiver module waiting for new incoming data.

- *Read RX*: Once new data is received this state identifies the hexadecimal control instruction: enquire state of FPGA, start Acquisition, start transmission, and reset. For the case of enquire state it start the process to send an Acknowledge (Ack) command through the TX module. If the received data do not match any of the control instructions a Not Acknowledge (nAck) command is send through the TX module.

- *Read FIFO*: Read a register from the FIFO, if the FIFO is empty it it start the process to send an End Of Transmission (EoT) command to the TX.

- *Send Data*: Since the register is a 16bit word and the RS-232 only allow to send 8bits per package this state split the register in Most Significant Bits (MSB) and Least Significant Bits (LSB) and load 8bit per time to the TX buffer.

- *Set TX*: Wait for the TX module to load the data package.

- *Send TX*: Enables the start of transmission and wait for the process to be completed.

- *Acquire*: Enables the write request of the simple counter to load data in the FIFO and wait until the FIFO is full.

- *Reset*: Performs a hard-reset on all modules. All buffer are cleared and the FIFO is empty, the next state is always IDLE.

A digital tachometer is running in parallel to the acquisition and communication. The velocity is calculated in the RPM calculator module and sent to the LCD main module which converts the number into characters and send the message to the LCD driver module. The driver module is in charge to configure the LCD display and write new characters or execute control commands.

The FPGA only acquire the number of cycles per pulse of the encoder, the processing is performed offline after downloading the data in a host. A LabVIEW interface is used to communicate with the sensor to request an acquisition or to download the stored data from the FPGA. The data is stored in an excel file and in a TDMS file. The post-processing program is implemented in Matlab. In this program the data (number of clock cycles per pulse) is converted to instantaneous angular velocity using Equation 1.62.

### 2.1.1 TIMS Sensor Test

To test the functionality of the TIMS sensor a simple test-bench was designed. The test bench is shown in Figure 2.5, it consists of a drill moving a shaft that connects an encoder and a bearing.

During the test the speed was difficult to keep constant as observed in Figure 2.5c but the benefits of using the TIMS method is that the spectrum is not affected by speed fluctuations as it will be shown in the preliminary tests of Chapter 4.

The frequency spectrum of interest was found to be below the 600 orders. hence the ppr of the encoder where set to 1200 using the divider switchs of the TIMS sensor. By decreasing the ppr of the encoder the number of turns are increased up to 109 turns as given by Equation 2.3 and hence the spectral resolution refines to 109 lines per order. To understand this better, lets assume a synchronous motor speed is set to 60 Hz, then the equivalent frequency resolution will be 60/109 since each order is a multiple of the shaft speed. In case the motor speed is set to 30 Hz the equivalent frequency resolution will be 30/109. Now we could see that the selection of the ppr depends of the spectrum of interest and the resolution we need based on the expected speed of the motor.

## 2.2 Rotor Kit Test Bench

Research of the effects of lubrication starvation in ball bearings require basic experimentation since the mathematical models are not yet well developed. The experimental

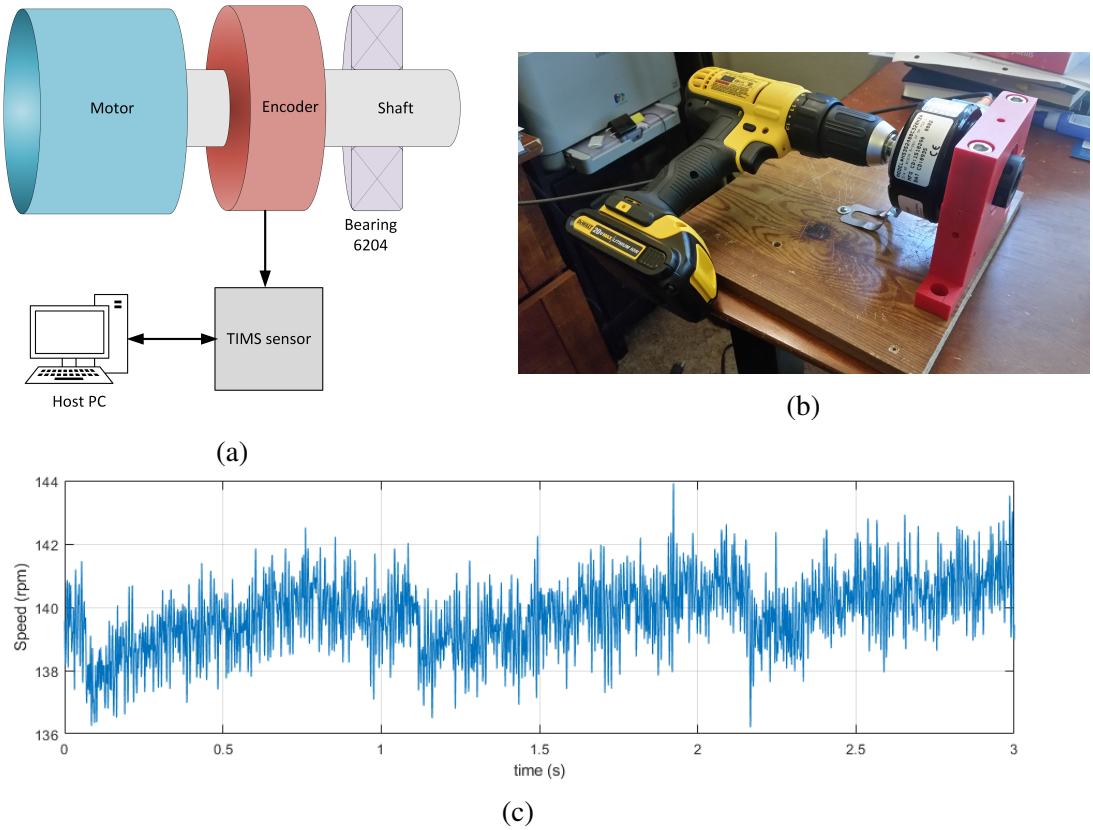


Figure 2.5: (a) Scheme of preliminary test-bench. (b) Photo of preliminary test bench used to test TIMS sensor. (c) Sample of speed data acquired with TIMS sensor.

results will help to improve and validate mathematical models and numerical simulations results. In order to provide valid results is necessary to control the parameters that affect lubrication, as reviewed in Section 1.2 these parameters are speed, load, viscosity and material properties.

The test-bench called *Rotor-Kit* is prepared to realize the experiments of lubrication starvation (Figure 2.6b). The machine is equipped to test bearings under dry and lubricated conditions while measuring vibrations at bearing housings, motor torque, shaft speed, voltage, current, and torsional vibrations. The bearings used for experiments are of the standard series 6204-2rs-10, information about dimensions and characteristic fre-

quencies could be found in Appendix B.2. To control the velocity of the experiment a Variable Frequency Drive (VFD) is driving a 3 HP induction motor while to control the load multiple metal disks could be added between the bearing housings. The parameter of viscosity is controlled by removing the lubricant from all tested bearing to later use the grease LGMT2.

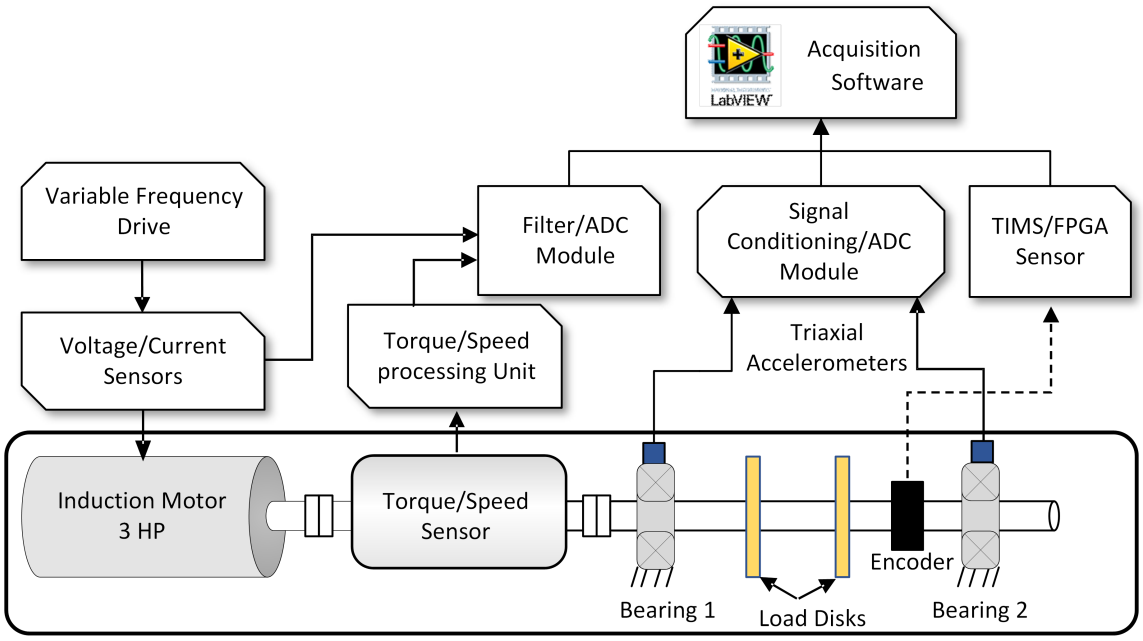


(a)

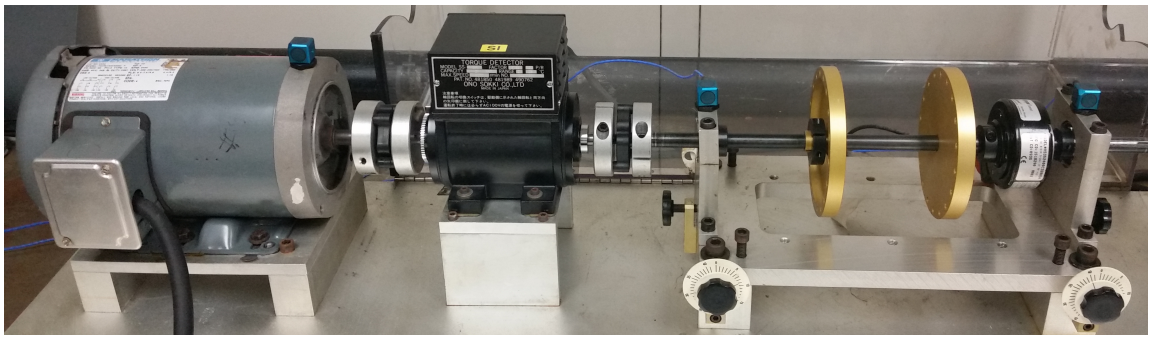

(b)

Figure 2.6: (a) Diagram of Rotor-Kit system. (b) Picture of experimental setup Rotor-Kit.

To measure lateral vibrations two tri-axial accelerometers[3] are installed at each bearing housing of the rotor. The speed and torque are measured by a torquemeter[4] coupled between the motor and the rotor. The encoder for the TIMS sensor is mounted on the shaft close to the bearing #2 since is the one selected for all experiments. Bearing #2 showed lower frequency perturbations from the VFD and motor than bearing #1.

For the energy analysis is necessary to measure the voltage and current at the motor power lines. Voltage sensors[5] are connected from phase to phase while currents sensors[6] are mounted in each phase. The calibration procedure for the voltage and current sensors is found in Appendix B.1.

The data acquisition system is configured to sample at the frequency of 60kHz based on a structural impact test where the bearing shows frequency activity between 10-20 kHz. To attenuate the aliasing effect an analog low-pass filter is calibrated for a cut-off frequency of 20kHz.

To determine the location of the VFD frequency perturbation the motor was uncoupled from the rotor and a ramp-up and coast-down test were performed from 1200 to 1800 rpm. In Figure 2.7 is shown the perturbations from the VFD located around 5kHz, 15kHz and 20kHz. Since the frequency of interest is between 10kHz and 20kHz the data is filtered using a notch filter at the 15kHz frequency.

Three LabVIEW interfaces are created to acquire the data. The lateral vibrations interface acquires the accelerometers and rotor speed, the torsional vibration interface only acquires the TIMS sensor data, and the energy efficiency interface acquires the three voltages and three currents of each phase besides the torque and speed from the torquemeter.

The lateral vibration interface besides acquiring and logging the data performs the FFT

[3]PCB Piezotronics model 356B08
[4]ONO SOKKI model SS-200
[5]LEM LV25-P
[6]LEM LAH25-NP

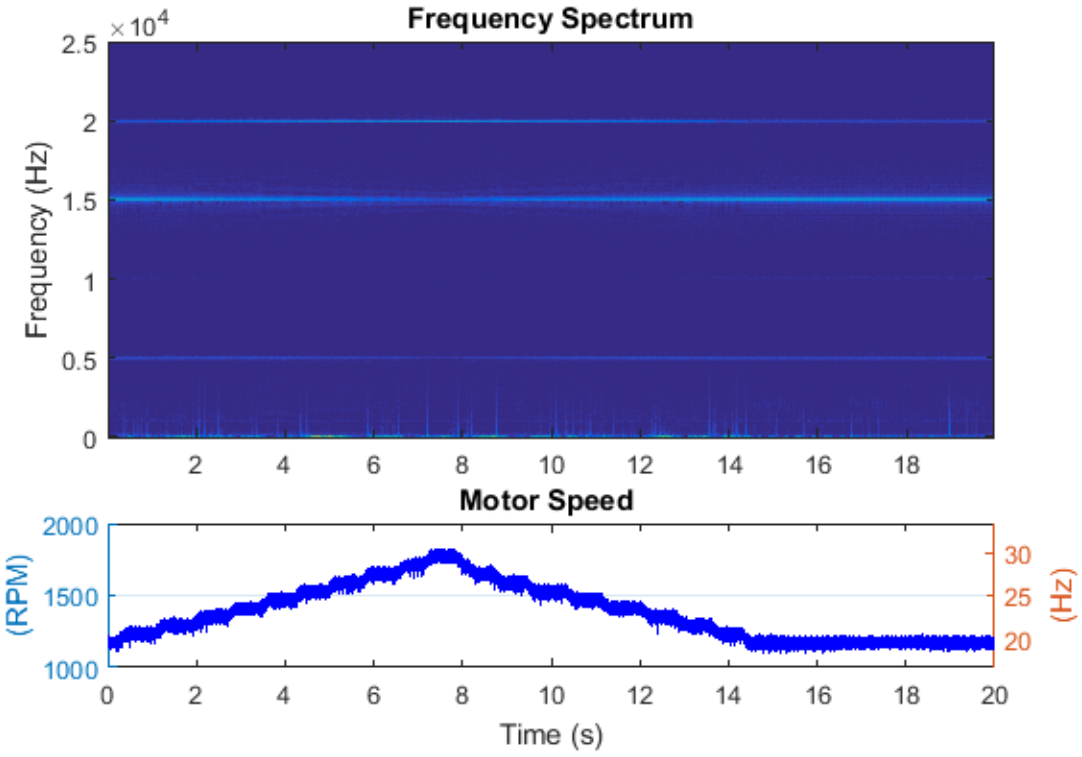


Figure 2.7: VFD perturbations

for each axis on each accelerometer and calculate the fault indicators rms, crest factor and kurtosis. Moreover, the ISO standard 10816 is implemented to monitor the severity of vibration on the system. Finally a monitor for unbalance, misalignment and looseness is also included. In general the lateral vibration interface and the acquisition system could be used as a permanent condition monitoring system for the Rotor-Kit. The Rotor-Kit is prepared to simulate several other common failures as unbalance, misalignment, bearing spalls, shaft bending, motor electrical problems, and gear damage.

## 2.3 Rotor-Kit Upgrades for Energy Analysis

For the last part of the experiments that concerns to energy efficiency, the Rotor-Kit need some modifications to optimize the results and control the variables. The two main

| Levels | Description | Levels | Description |
|---|---|---|---|
| 0 | No generator coupled | 10 | Generator + 460 Watts lamps |
| 1 | Generator connected no lamps | 11 | Generator + 500 Watts lamps |
| 2 | Generator + 60 Watts lamp | 12 | Generator + 560 Watts lamps |
| 3 | Generator + 100 Watts lamp | 13 | Generator + 600 Watts lamps |
| 4 | Generator + 160 Watts lamps | 14 | Generator + 700 Watts lamps |
| 5 | Generator + 200 Watts lamps | 15 | Generator + 800 Watts lamps |
| 6 | Generator + 260 Watts lamps | 16 | Generator + 900 Watts lamps |
| 7 | Generator + 300 Watts lamps | 17 | Generator + 1000 Watts lamps |
| 8 | Generator + 360 Watts lamps | 18 | Generator + 1100 Watts lamps |
| 9 | Generator + 400 Watts lamps | 19 | Generator + 1200 Watts lamps |

Table 2.1: Load levels

modifications done to the plant is the design and manufacture of a new shaft that could carry a heavier static load of 7 Kg and allows a quick change of bearing by replacing the heat-mounting procedure by a lock nut and shoulder method. The upgraded Rotor-Kit will allow to perform energy research on rotors components as bearings, couples, gear trains and induction motors.

Load factor is the main parameter to control for motor efficiency tests. A 3 hp generator/motor is coupled to the end of the rotor to be used as a variable load. An induction motor is used for generation, hence a capacitor bank must be connected to each phase to excite the magnetic field in the stator to start the generation. The capacitors are rated for 440VAC with a value of $22muF$.

The load is controlled by connecting lamps to each phase. Different levels of load are shown in Figure 2.8 and the levels are described in Table 2.1, the load factor generated by each lamp is calculated using the torque and speed sensors. To minimize the number of tests, the selected levels are 0, 13, 15, 17, and 19. Figure 2.9d shows the diagram of connection for the generator, in the diagram is shown level 13 controlled by a fuse-box switch and level 15 to 19 controlled by individual switches.

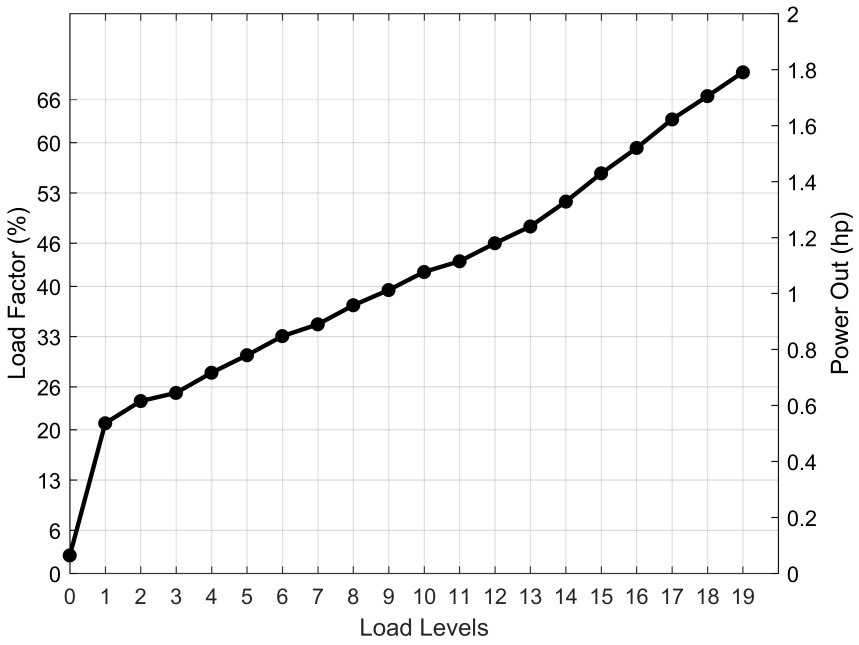


Figure 2.8: Generator load depending on the number of lamps used

The upgraded plant is shown in Figure 2.9. The generator starts producing energy at 35 Hz but to increase the load the speed is increased to 40 Hz. Some other conditions for the generator is that its rotor must rotate in the same direction as when connected directly to the power line, hence the VFD is configured to rotate the motor in the reverse direction. Moreover, the lights should be off during the start-up to allow the capacitors to generate the magnetic field. If the generator has been unused for a long time the capacitors must be quickly charged with a DC power supply, in our case the capacitors where charged with 50 Volts DC before the first test, after that the charge was no longer needed. In the same way as the start-up, the lights should be off when the motor is stopped to avoid draining the energy of the capacitors or the stored magnetic field in the coils. Finally, the acceleration/deceleration time on the VFD is configured to 30 seconds to protect the motor.

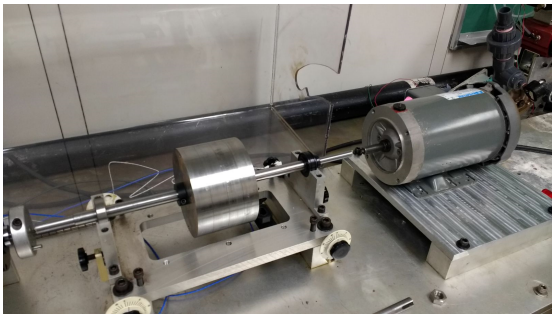

(a)

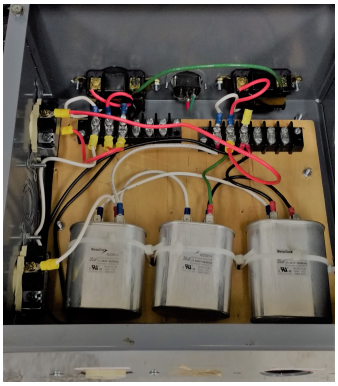

(b)

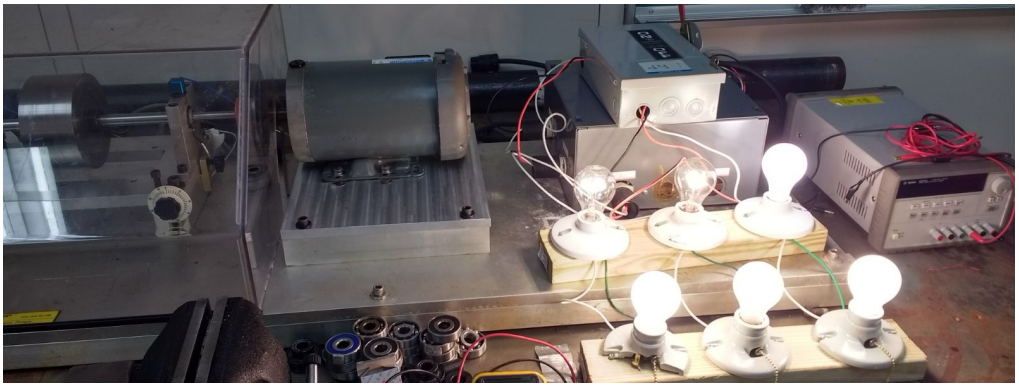

(c)

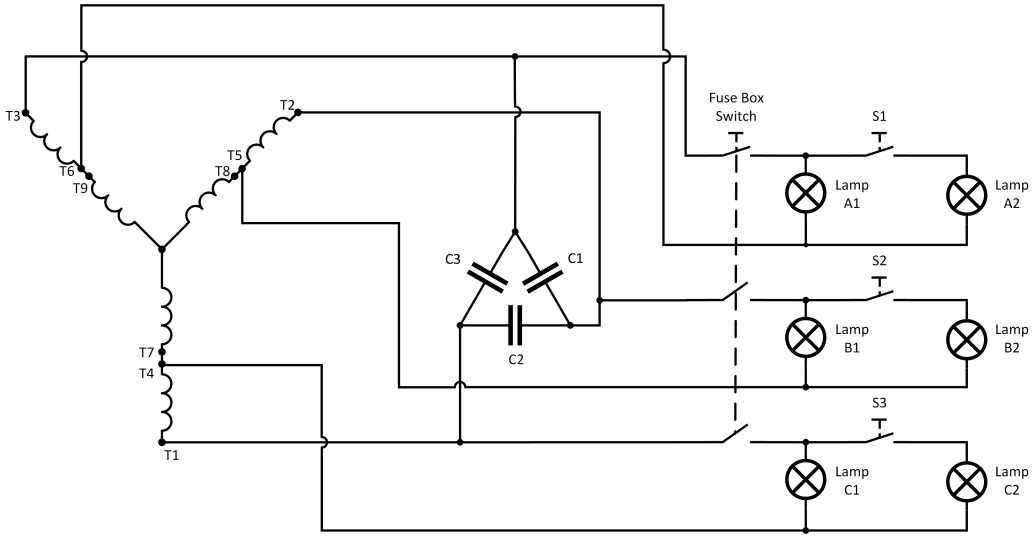


(d)

Figure 2.9: (a) New shaft with increased load; (b) Capacitor bank; (c) Generator and lamps to increase load; (d )Circuit diagram for generator

# 3. LATERAL VIBRATIONS

In the research of lubrication starvation lateral vibrations has been the main source of diagnostic methods. As mention in Chapter 1 the research effort conducted in these area has been based on experimental results that provide indicators in the frequency domain. The problem with this approach is that there is no explanation of the source of these frequencies or the increase of vibration activity in the signal. In this work is presented an approach to explain the effect of lack of lubrication on a ball bearing, which are the excess of clearance and lack of damping mechanism to dissipate the impacts in the load zone.

Boškoski et al. [12] proposed that in the absence of lubricant, the gaps previously filled by the grease or oil will be empty, hence increasing the clearance and the restrictions between the cage and the balls. Moreover, Wijnant in 1999 [48] proves that the lubricant behaves as a spring damper system that dissipate the energy of impact between components. Combining the lack of restriction and damping mechanics is expected and increase in the vibration activity due the bouncing of components around the bearing.

The first section of this chapter is focus on explaining the temperature effects on the bearing to study the impact that this secondary parameter will have on the experiments of the following sections. The second and third section will cover the experimental procedure and results of reducing the clearance which is used to corroborate that the increase in gap was the source of the characteristic vibrations that identify lubrication starvation. As previously covered in Section 1.8 the clearance could be reduced by increasing the interference between the housing and the outer ring, the temperature effects covered in the first section should be considered for the clearance reduction. The sections of experimental setup and fault detection are based on the work presented in [75] by the author of this work. The last section will discuss fault diagnosis results which are the extension of the

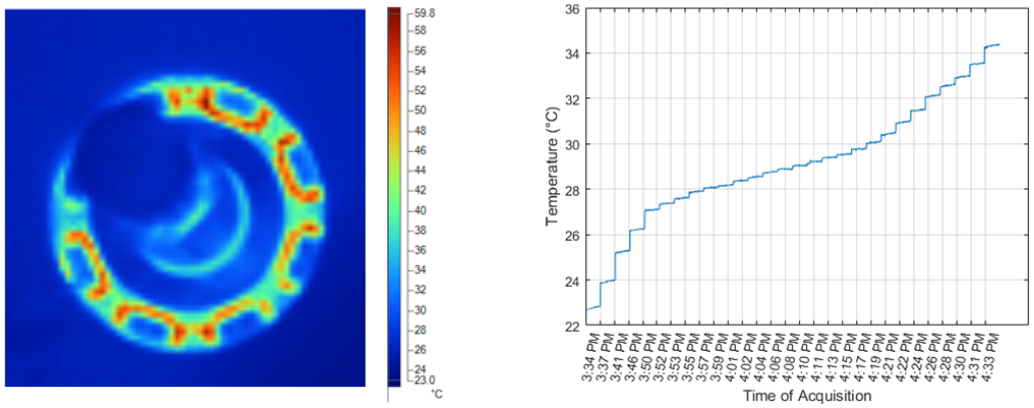


(a) (b)

Figure 3.1: (a) Thermal image of inner components. (b) Temperature measured at outer ring.

fault detection section.

### 3.1 Temperature and Interference Effect on Clearance

To study the effect of thermal expansion it was necessary to determine the temperature increase that the bearing is subject under dry conditions. A thermocouple sensors is placed between the outer ring and the housing of the bearing and a thermal camera is used to measure the temperature of the inner ring and rollers. Figure 3.1a shows the results for the inner components temperature while Figure 3.1b shows the results for the outer ring temperature. An assumption that could be done based on the experimental results is that the inner ring temperature is the same as the outer ring. The balls present the higher increase on temperature due the absent of lubricant to dissipate the heat through the cage. As an alternative to lateral vibrations the temperature monitoring of bearing elements could also be used to detect lubrication starvation in the last stages of the fault, probably just to trigger an emergency stop.

The study of thermal expansion is based on the measured temperatures, geometries ,and material properties of the bearing components. The two geometries of interest found

in the bearing are the ring and the sphere. The thermal expansion is due an increase of temperature $\Delta T$ with respect to a reference, in our case is the ambient temperature $T_a$. For a ring of outsite diameter $d_o$ the thermal expansion for a difference of temperature $\Delta T_O$ will increase the outer circumference approximately by

$$u_{toc} = \Gamma_b \pi d_o \Delta T_o, \tag{3.1}$$

in which $\Gamma_b$ is the thermal expansion coefficient of the ring material. Converting the circumference to a diameter we obtain

$$u_{to} = \Gamma_b d_o \Delta T_o, \tag{3.2}$$

Using a similar analysis we obtain the inner ring thermal expansion and subtracting the difference between the two changes of diameters we obtain the change in clearance due ring expansion

$$\Delta_{Ring} = \Gamma_b \left[ d_o \Delta T_o - d_i \Delta T_i \right]. \tag{3.3}$$

The thermal expansion of the housing will also impact the interference $I$ between the housing and the outer ring by reducing or increasing it depending of the coefficient of the housing. The change in interference is given by

$$\Delta I_h = (\Gamma_b - \Gamma_h) D_h \Delta T_o, \tag{3.4}$$

where $\Gamma_h$ is the expansion coefficient of the housing and $D_h$ is the nominal housing diameter. For the case of the interference between the inner ring and the shaft the equivalent of Equation 3.4 is

$$\Delta I_s = (\Gamma_s - \Gamma_b) D_s \Delta T_i, \tag{3.5}$$

Using the change in interference for the outer and inner ring on Equations 1.48 and 1.49 we obtain a new $\Delta_s$ and $\Delta_h$ respectively. To complete the analysis, the change of ball diamater $\Delta D_{ball}$ should be consider. The change on clearance due to balls thermal expansion is given by

$$\Delta_{ball} = 2\Delta D_{ball} = 2 \cdot (D_{ball}\Gamma_{Ball}\Delta T_{ball}) \tag{3.6}$$

where $\Gamma_{Ball}$ is the linear coefficient of the balls. The linear thermal coefficient for each of the components is listed in Table B.2. The total change on clearance considering the thermal expansion is given by

$$\Delta P_d = \Delta_{Ring} - \Delta_s - \Delta_h - \Delta_{Ball}. \tag{3.7}$$

Figure 3.2 shows the effect of interference and the change on clearance. In the top section is possible to observe a decrease in the interference for the housing. In the case of the shaft there is a decrease of interference for a shaft made of steel 1040 while for a shaft of stainless steel 303 the interference increases. The plot at the bottom shows each of the component effects on the clearance and the result on the total change of the clearance. The most relevant components are the rings, housing, and ball. As a results there is an increase of clearance as the temperature rises.

The change on clearance due thermal effects is included in the calculations of clearance due bearing-housing interference, which is used to compensate the extra gaps created by the lubricant absence. A shim of 0.001 in is used to create this reduction on clearance. Figure 3.3 shows the comparison between the normal and the increased interference considering the temperature increase effects. Due the small variation of clearance due temperature effects compared to the shim effect, is possible to assume that the results will

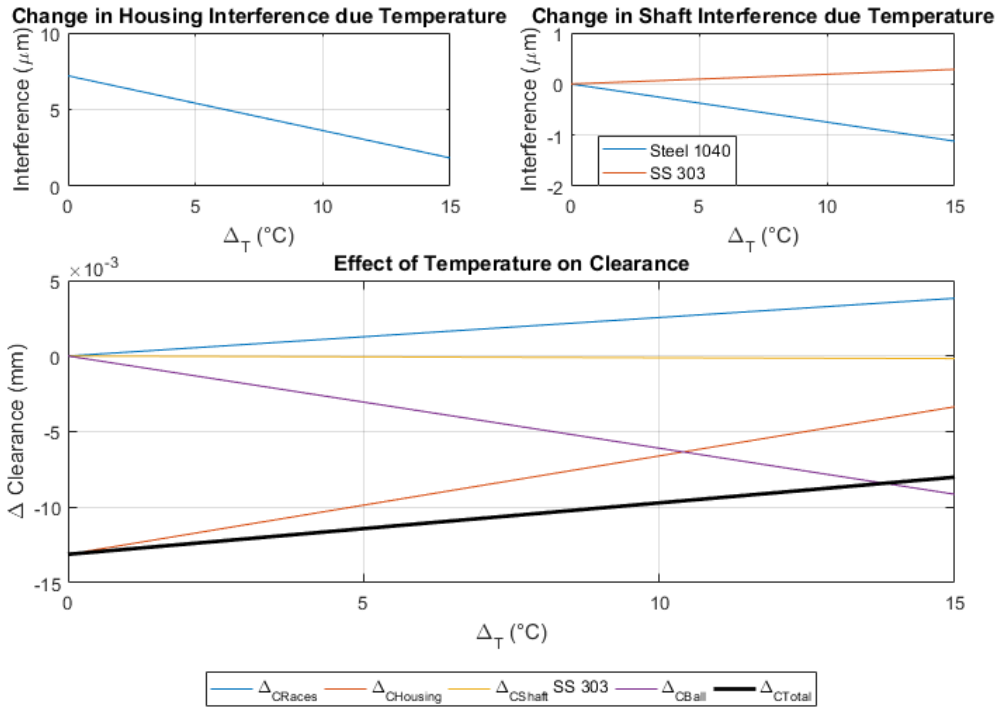


Figure 3.2: Interference and clearance change due thermal effects

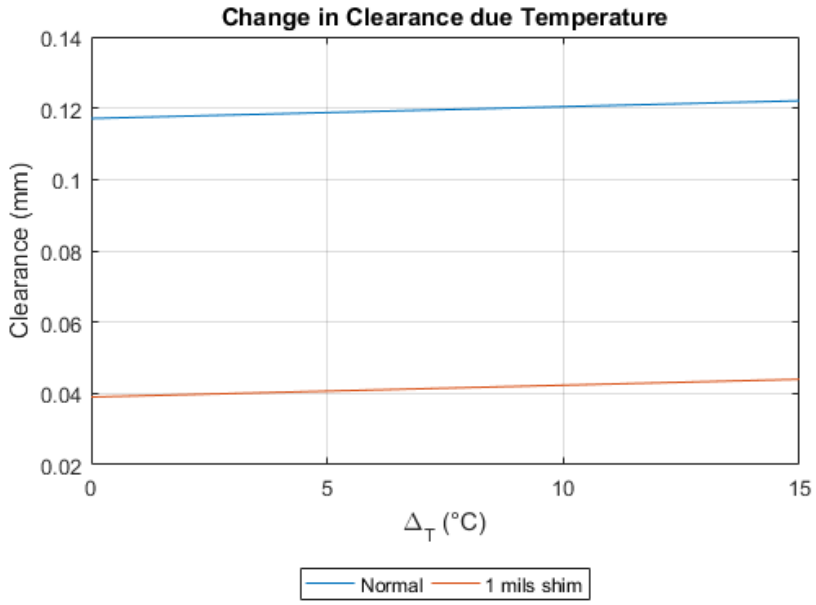


Figure 3.3: Clearance reduction due shim interference

not be vary drastically with time as the machine increases its operating temperature.

## 3.2 Experimental Procedure

A total of six experiments were conducted and each experiment consisted on testing a new bearing under four different conditions. The *dry* test is the first of the tests on each experiment, a careful and systematic procedure was done during the preparation of the bearings; mineral spirit was used to remove the lubricant and completely clean the bearings, special attention was made to avoid any foreign particles from entering the bearing and affecting the experiments. The bearing was temperature-mounted on the shaft. To mount the rotor on the bearing housings all screws were tightened to 15 lb-ft with the objective to control the interference on all tests.

Once the test under dry conditions was completed, the testing was repeated but with a shim to increase the interference on the bearing as detailed in the previous section, this

test condition is called *interference* test. For the final two condition tests, the shim was removed from the bearing and two levels of lubricant were tested (5% level and 100%) to evaluate the efficiency of the methods on detecting dry, low, and fully lubricated conditions, these test where called *min and full lubricated* tests. Grease LGMT/2 was added to the bearing using a syringe, distributing even quantities around all rollers. The total amount of grease (1.2 g) was determined previously by weighting five bearings before and after removing the lubricant, the procedure and data is found in B.4.

The machine was warmed up for two minutes before starting to acquire data, and ten continuous acquisitions were taken for each test. In all analysis, a 95% confidence interval was used to obtain the uncertainty of the ten measurements. All acquired signals were processed with a digital filter to remove a VFD perturbation at 15 kHz and band-passed between 1 kHz to 20 kHz, in order to keep only high frequency content and remove any residuals of the analogue filter.

### 3.3 Fault Detection*

The procedure presented in the previous section is used to compare the level of vibrations under different conditions. The vibration levels are compared using three of the most common indicators presented in Section 1.9: RMS, Crest Factor and Kurtosis. A comparison of the three indicators is also discussed to determine the most effective method to detect lubrication starvation. Figure 3.4 shows the characteristic signal of lubrication starvation vs a lubricated bearing, in the plot is possible to observe an increase in the impulsivity of the signal.

*Reprinted with permission from "Detection of lubrication starvation in ball bearings and preload effects" by Jorge Mijares, Bryan Rasmussen and Alexander Parlos, 2017, Proceedings of The Society of Machinery and Failure Prevention Technology, pp. 1-10, Copyright 2017 by MFPT.

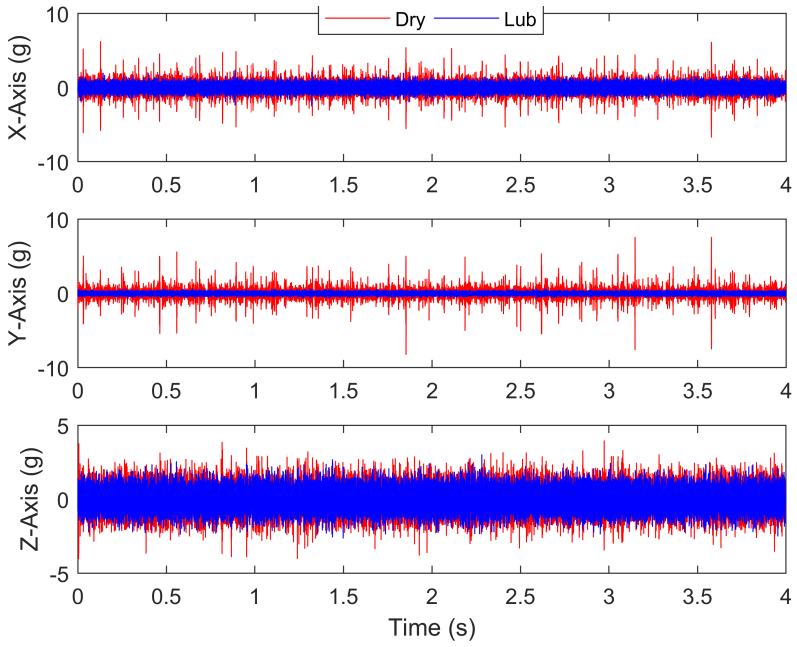


Figure 3.4: Comparison between a bearing running on lubricated and dry condtions.

### 3.3.1 RMS

As mention before RMS is a way to measure the energy content in the signal. Figure 3.5 compares RMS values at the different conditions for all experiments, for each experiment the value on dry conditions is higher than at lubricated conditions, but the range is different for each bearing, thus, a limit to detect lubrication starvation for all bearings cannot be established without compromising the indicator with false alarms or missed faults. Besides, the indicator increases under interference conditions even if the impulsivity of the signal decreases as shown further by the other indicators. The problem associated with interference is the change of resonance frequencies due a change in stiffness, and the possible excitation of the bearing housing due the increase in dry friction, which is random excitation generated from surface roughness. Hence, even if the impulsivity of the signal decreases the RMS cannot detect the change when an increase on interference is applied.

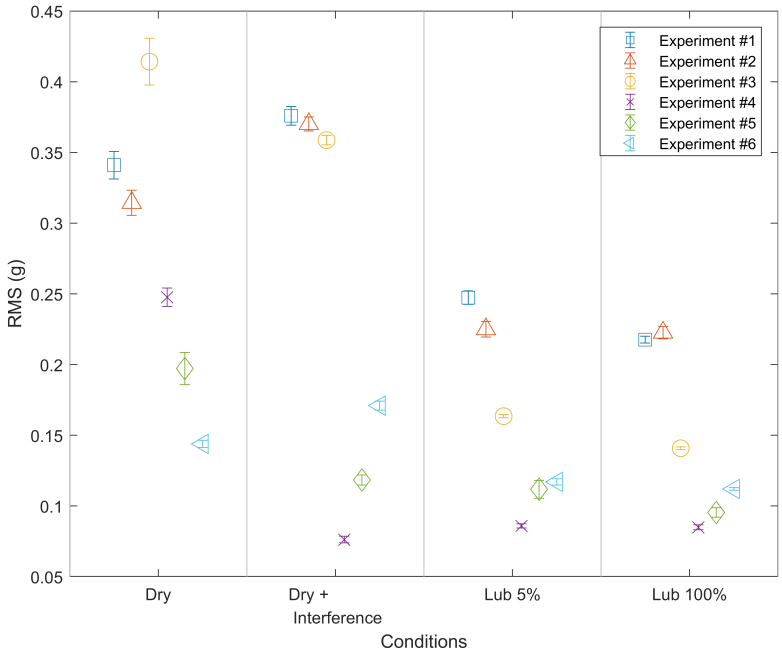


Figure 3.5: RMS performance comparison for test conditions

Figure 3.6 shows a cascade comparison for experiment #2, in which a switch of frequency is observed due increase of stiffness from 4 to 6 kHz (frequency range associated with the rotor-assembly resonance frequency), and an increase in activity at 11 kHz (vertical resonance of house bearing).

### 3.3.2 Crest Factor

The crest factor of the vibration signal, shown in Figure 3.7, is a better indicator than RMS when applied to detection of bearing starvation, since is more sensitive to impulsivity. The problem is the similarity between lubricated and dry conditions, as shown in Figure 3.8, if a severity level is established based on dry condition results, some of the full lubricated results may trigger a false alarm. An advantage of CF is the high sensitivity for low lubrication levels.

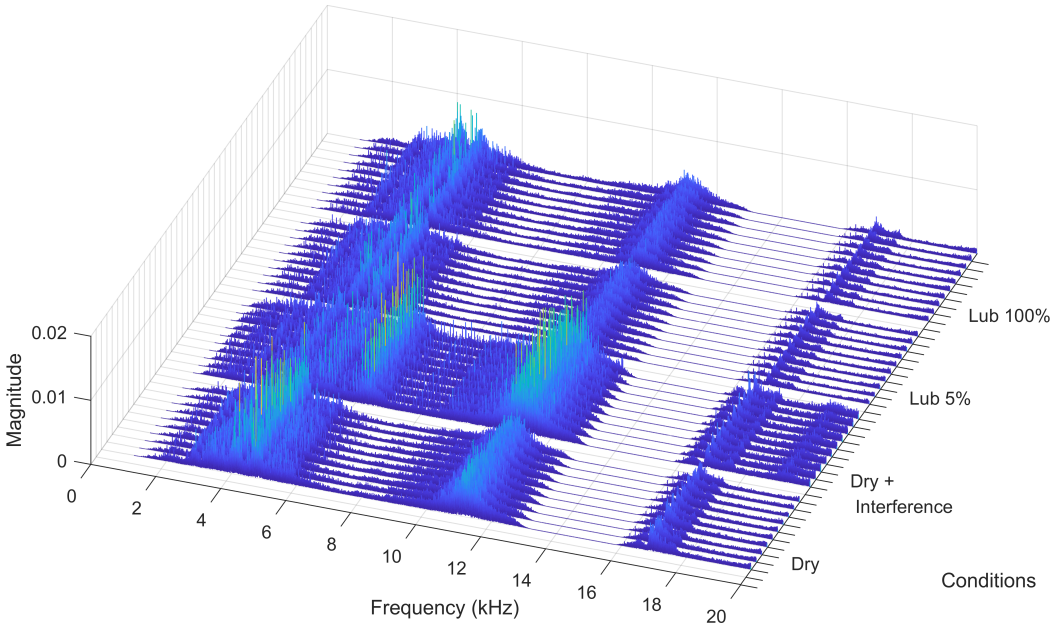


Figure 3.6: Stiffeness change due increase in interference

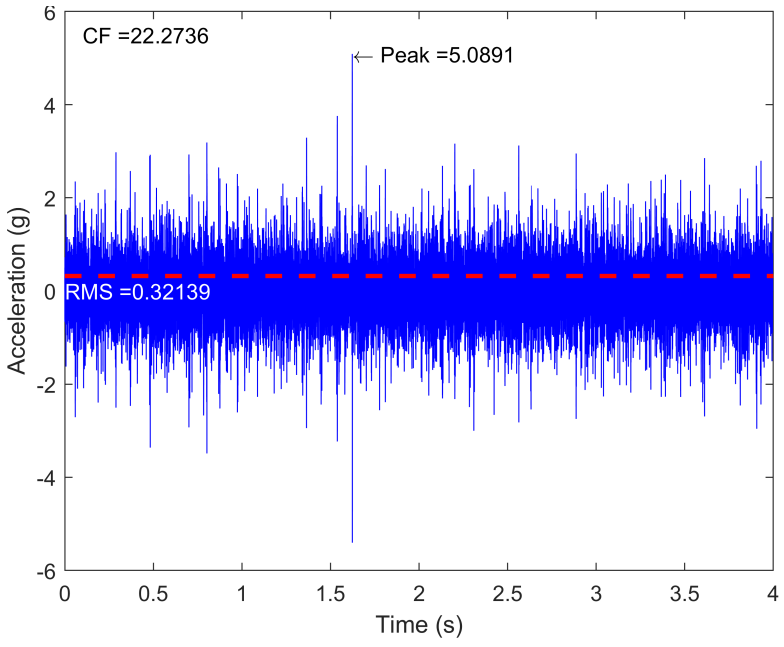


Figure 3.7: Crest Factor in a vibration signal

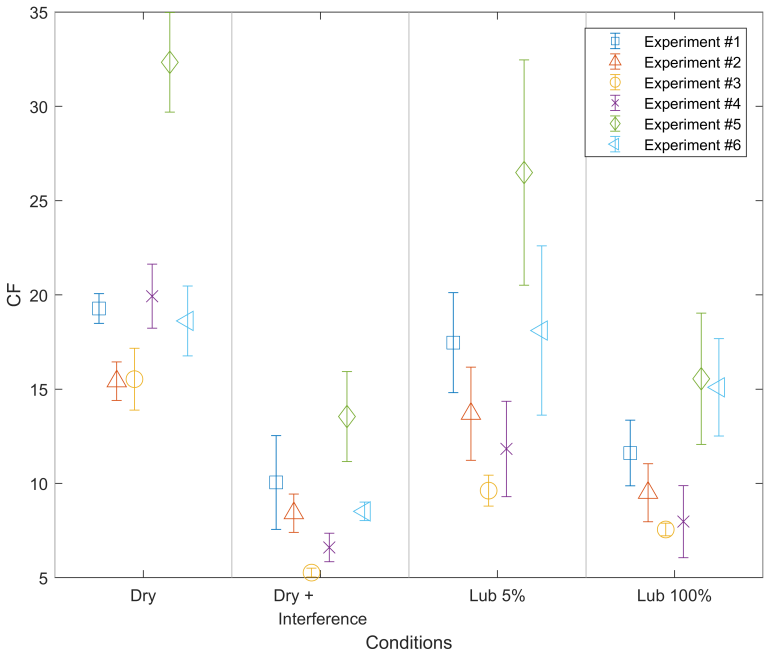


Figure 3.8: Crest Factor performance comparison for test conditions

### 3.3.3 Kurtosis

Kurtosis results, presented in Figure 3.9, show a better performance than RMS and CF to detect lubrication starvation, the consistency between experiments allow proposal of severity levels: 0-3 good, 3-7 satisfactory, 7-10 unsatisfactory, 10- unacceptable.

The main disadvantage is the variability between acquisitions of the same experiment, therefore more than one acquisition is recommended for an effective evaluation, which could be a problem when a large number of machines must be assessed. A decrease in impulsivity of the signal, when a interference is increased, is observed in both CF and Kurtosis indicators, as explained by Sawalhi and Randall [15], the impulsivity could be attributed to each time a ball enters the load zone and a small impact is produced, generally these excitation are small and quickly damped by the lubricant which also acts as an isolation mechanism between the balls and the bearing structure, but with the absence

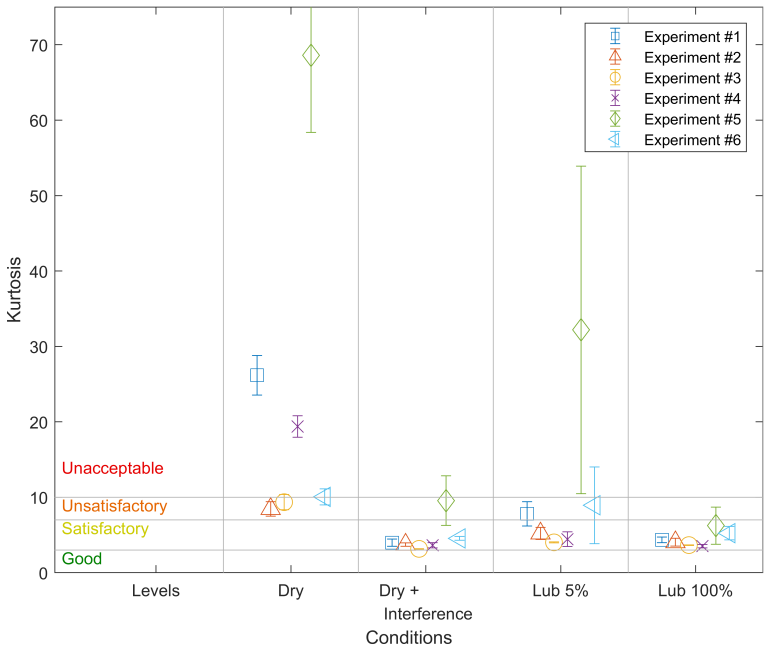


Figure 3.9: Kurtosis performance comparison for test conditions

of lubricant and the increase in clearance, the impact amplitude increases and the wave is propagated to the bearing housing, hence the increase in FTF and BSF. When a sufficient interference is applied, the clearance between the balls, train, and the races is reduced as an effect of load deformation and in the case of light loads the deformation due preload dominates over the deformation due to dynamic or static load, therefore the ball never enters or leaves the 'load zone'. Both factors reduce the source of impacts that characterize the lack of lubrication.

### 3.3.4 Fast-Kurtogram as Method to Increase Kurtosis Performance

The results of FK exhibit a predominant central frequency ($F_c$) at 17.8 kHz with a bandwidth ($B_W$) of 1.8 kHz (level 4), the region is associated with a resonance frequency of the bearing housing. Figure 3.10 shows the results for dry conditions of experiment #1, these parameters could be used to filter all signals and apply an envelope analysis to

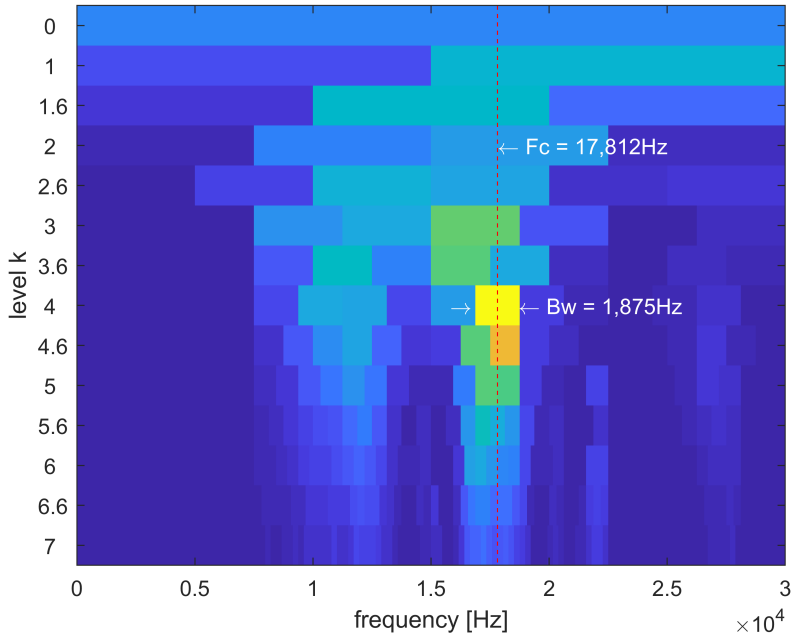


Figure 3.10: Fast-Kurtogram results for Experimenet #1 under Dry Conditions

find the origin of the impulses and how the amplitude reduces, but in these section only the maximum level of kurtosis is used as a fault indicator. This work presents the advantages of using FK analysis to improve kurtosis as a fault detection method for lubrication starvation. Figure 3.11 compares the results of using the maximum kurtosis value found in the Fast-Kurtogram for each of the conditions. The mayor improvement is the sensitivity to detect low levels of lubricant where the kurtosis of the entire high frequency spectrum does not differs from full to low lubrication. Moreover, a decrease of impulses on the signal is corroborated on these results as well.

The mayor disadvantage of FK vs Kurtosis of the entire signal is the processing time for an online condition monitoring this factor should be considered for the selection of the method of fault detection. The factor of the speed is because the FK performs a filtering of the signal on each of the levels of decomposition across several frequency bands. These burden could be decreased by using a DSP device to improve the filtering speed.

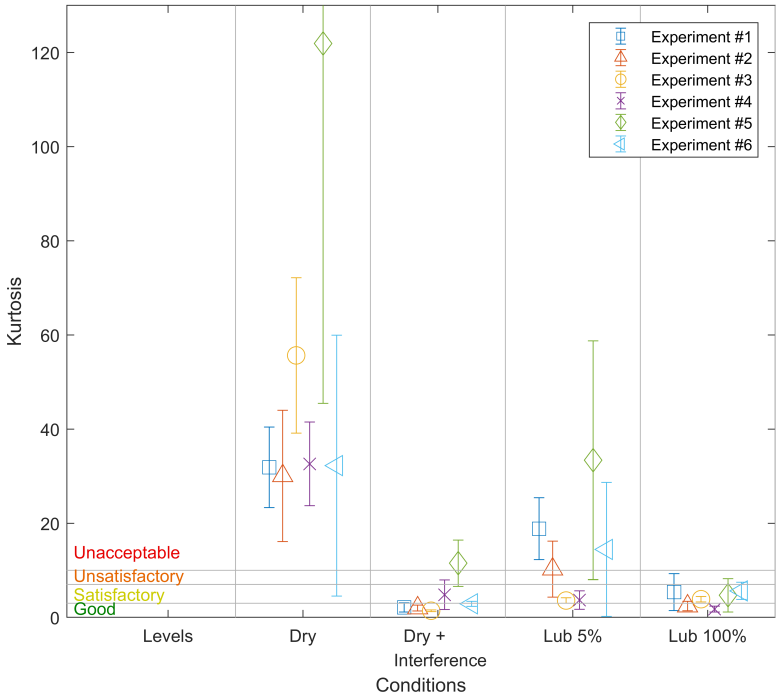


Figure 3.11: Kurtosis performance using the maximum kurtosis value localized by FK

The levels proposed for the kurtosis of high frequency spectrum were also used in the kurtogram results. Experiments 1,2,5, and 6, detected low lubrication as an unacceptable fault. For condition monitoring is important to minimize false alarms without compromising the sensitivity of the method to detect a problem which, as in this case, is low levels of lubrication.

### 3.3.5 Run Until Failure Test

A run until failure experiment is shown in Figure 3.12a to test the performance of the three indicators. The experiment is separated in five conditions, starting with a lubricated test to establish a base line. After removing the lubricant the bearing is test under dry conditions, here is possible to observe the increase in the indicators as the bearing warms up. Following the dry conditions a shim of 5 mils is used to increased the interference and is possible to observe the decrease of impulsivity in kurtosis and crest factor although the

rms value remains high due the increase in the friction excitation. To accelerate the failure of the bearing a shim of 10 mils is used to increase the interference and the friction. In this level the RMS and the indicators increase due the excessive level of interference and the lack of lubrication. Finally, a shim of 15 mils is used to accelerate further more the wear on the bearing.

In the last condition is interesting to observe that although RMS increases up to 2 g, the level of kurtosis and Crest Factor decrease under the values of the previous test. This phenomena is due the nature of the indicators. In the case of kurtosis the noise levels are high enough to cover the impulses due the impacts on the load zone, by applying the FK method as a filtering technique as shown in Figure 3.12b, the noise is separated from the signal and the kurtosis performance increases for the critical case from 10 to 130.

The accelerometer used in this experiment is limited up to $\pm 5g$ intentionally demonstrate the problems of Crest Factor in real applications. Therefore in the case of Crest Factor the levels of peaks reach the saturation levels of the sensor while the RMS keep increasing, hence the ratio between peak and RMS decreases. As a recommendation Crest Factor is sensitive for low levels of vibrations, but CF should be ignored as the fault develops and the sensor reaches its saturation levels.

### 3.3.6 Discussion of Indicators Performance

Three main indicators, RMS, CF, and Kurtosis were evaluated to detect lubrication starvation in a ball bearing under light load. While RMS detects the presence of a fault in the system, is not recommended to be used alone to isolate faults related to bearings. It must be used with an additional indicator, sensitive to impulsivity, such as kurtosis or CF. Kurtosis proves to be a more consistent indicator than CF to discriminate between lubricated and dry conditions. Levels of severity are proposed for kurtosis, the levels are based on experimental results, but a formal methodology to select levels is needed. Instead

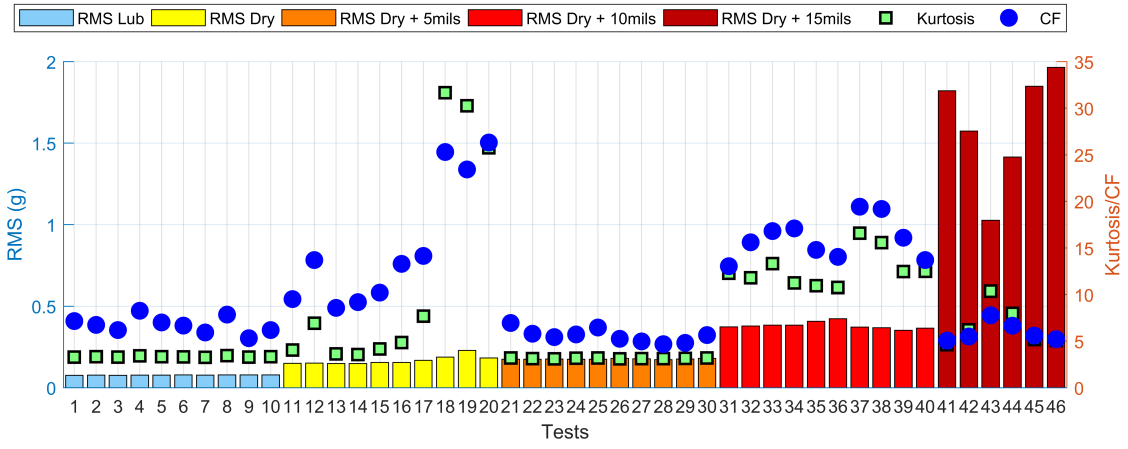


(a)

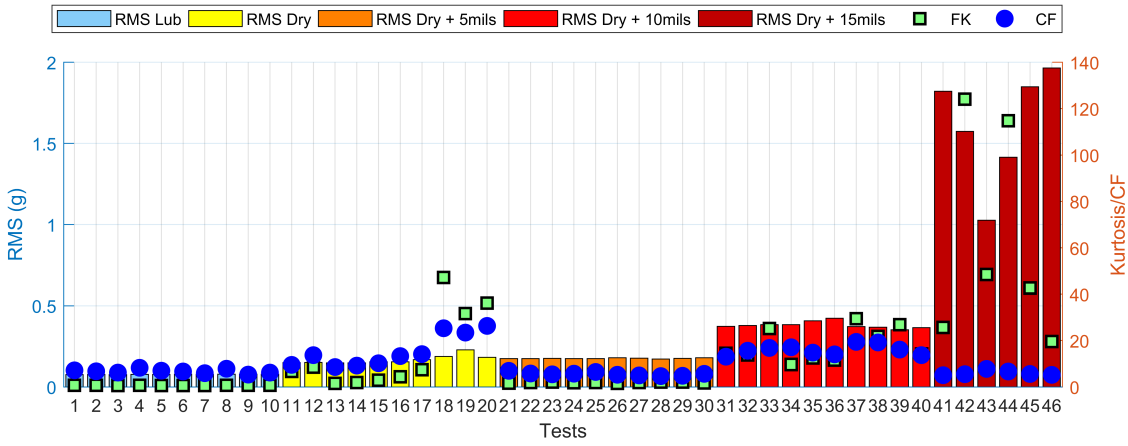


(b)

Figure 3.12: (a) Indicators performance comparison for a run until failure test. (b) Improved performance of kurtosis using Fast-Kurtogram.

of using fixed levels based only on kurtosis values a machine learning technique could be applied to include RMS and CF to improve the fault detection for lubrication starvation.

A Fast Kurtogram was used to improve the fault detection based on kurtosis. An increase in sensitivity to low lubrication levels and a better discrimination between dry and lubricated conditions are some of the benefits. In future work, determining if FTF value decreases with preload is important as it supports the idea that the characteristic signal of lubrication starvation is generated due to the increase of clearance gap between bearing components. This could be done by applying an envelope analysis to the predominant frequency detected by the fast-kurtogram as explained previously by Boškoski.

### 3.4 Fault Diagnosis

The methods cover until now are used for just detecting the presence of a failure in the system, but for a complete condition monitoring system is necessary to include a diagnosis stage to determine the origin of the fault. Diagnosis methods for bearings are based on the characteristic frequencies reviewed in Section 1.9, although this frequencies are used more commonly for detecting localized faults as spalls or dents. In the case of starvation lubrication the fault is considered to be a non-localized fault since the fault is spread around the circumference. Usually these type of faults create and increase in the noise level due the randomness of the surface and a increase in two or more of the characteristic frequencies. Salwalhi and Randall [76] proposed a model of the bearing where they consider the frequency of impacts when the balls enter the load zone and causes a shift on the inner ring with respect to the outer ring. In lubricated conditions the movement is restricted and the impact is dissipated through the spring damper effect of the grease but in a critical stage as a complete dry bearing the impact is transmitted through the housing.

The frequency at which each balls will enter the load zone is the same as the cage frequency given by Equation 1.50, but considering the impact of all balls in the bearing the

expected frequency is the BPFO (Equation 1.53) (FTF multiplied by the number of balls). In the experiments of Boškoski et al. [12] the FTF frequency appears in the spectrum but not the BPFO, the reason is that the used experimental setup was a motor installed vertically. Therefore, it is expected that the load zone is the entire circumference of the bearing.

In the experiments presented in this work the motor is installed horizontally, hence is expected to have a load zone. The methodology used by Boškoski is repeated by starting with analyzing the data using the Fast-Kurtogram, which in the previous section proves to be an efficient method to separate the noise and non-impulsive components from the signal of interest. Later, an envelope analysis is used to extract the periodicity of the impacts to finally used the FFT to find the characteristic frequency associated with lubrication starvation.

### 3.4.1 Experimental Results of Lateral Vibrations

The results of FK for the experiments of fault detection provide the optimal central frequency and bandwidth to filter the raw signal and obtain a signal that contains only the impacts produced by the balls. Figure 3.13 shows the difference between the raw signal and the filtered signal selected by FK. It is interesting to observe that the impacts are preserved but the signal to noise ratios is improved and other vibrations that are not a product of the impacts are separated. In the impulse response is possible now to observe the transient response oscillations or the damped natural frequency of the bearing housing assembly. It is important to note the decrease in the amplitude of the signal. This is a drawback in the method but the important feature in the case of bearings is the frequency at which the impulses occur which is preserved.

After extracting the amplitude of the analytic signal using the Hilbert transform the transient of the impulse response is removed as shown in Figure 3.14. The FFT is applied

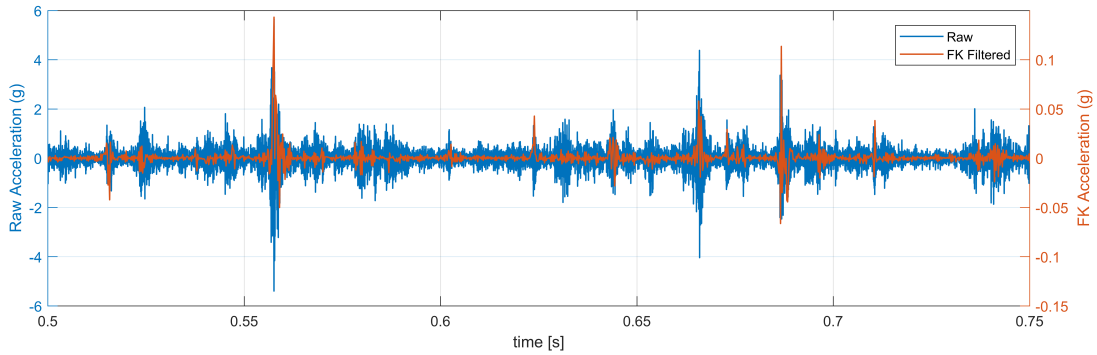


Figure 3.13: Comparison between the filtered signal and the original signal

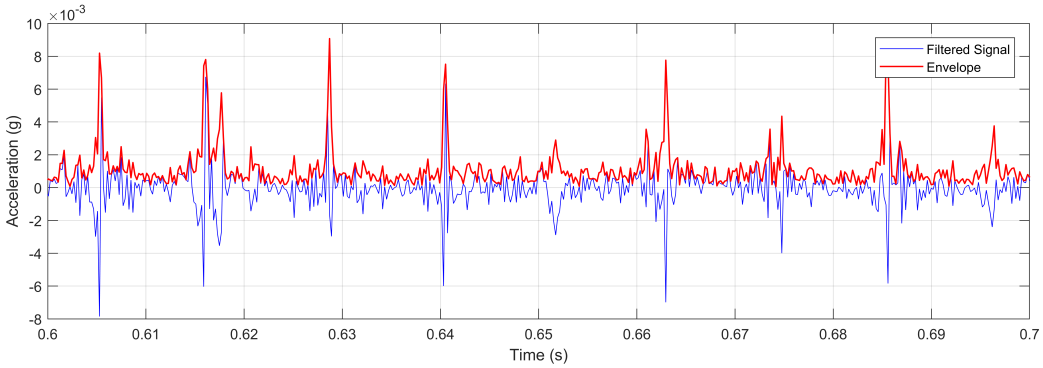


Figure 3.14: Envelope Results

to the envelope to obtain the frequency content. In order to attenuate the random components each condition is acquired at least ten times and the spectral results are averaged.

The frequency of impacts varies due slippage or change in the contact angle, hence the FTF frequency is located manually by matching all the harmonics as shown in Figure 3.15, the calculated FTF frequency is used as a base to start the matching. Once the FTF is found, BPFO is located by multiplying FTF by the number of balls as described in Equation 1.53. A similar manual method is used to find BSF while BPFI is disregarded due the lack of matching frequencies in all tests. Table 3.1 presents the final FTF values and the error with respect the calculated FTF, the maximum error was found to be 16.4%.

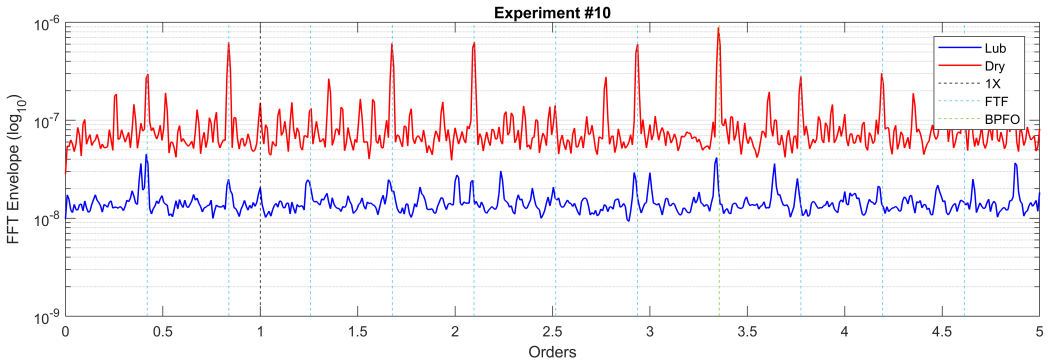


Figure 3.15: Zoom of Spectrum where FTF harmonics are used to find the real FTF.

### 3.4.2 Data Analysis

During the process of analyzing data was found that for the dry conditions there is an amplification of the frequency spectrum under lubricated conditions including the noise floor as shown in Figure 3.16. Hence, it is not possible to compare the values of the characteristic frequencies since all of them are higher than the lubricated values. The difference in magnitude is due the effect of the lubricant acting as a damper that dissipates the impact reducing the vibrations. The increase in noise floor could also be explained with the surface roughness that is now in contact due the lack of a minimum film thickness to separate the surfaces in contact.

To analyze the data a qualitative analysis is performed for each experiment. The analysis focus on detecting the presence of a characteristic frequency and its harmonics in the observed results. Table 3.2 summarize the results of the analysis.

The FTF and BPFO are found in the majority of the lubricated and dry conditions as shown in Figure 3.16. The BPFO predominates over the presence of FTF. The presence of the FTF is interesting since it was not expected but is also reported by Boškonski. The frequency indicates that the cage could be impacting the balls at the entrance of the load zone as well. Experiment #4 and #5 exhibit sidebands at the BPFO frequency indicating

Table 3.1: Measured FTF error with respect to calculated FTF.

| Experiment | FTF measured (X) | Error (%) |
|---|---|---|
| **Calculated** | 0.**3815** | **0** |
| E1 | 0.4364 | 14.4 |
| E2 | 0.4376 | 14.7 |
| E3 | 0.444 | 16.4 |
| E4 | 0.3864 | 1.3 |
| E5 | 0.4325 | 13.4 |
| E6 | 0.3874 | 1.5 |
| E7 | 0.4164 | 9.1 |
| E8 | 0.4189 | 9.8 |
| E9 | 0.3944 | 3.4 |
| E10 | 0.4194 | 9.9 |
| E11 | 0.4164 | 9.1 |
| E12 | 0.3944 | 3.4 |

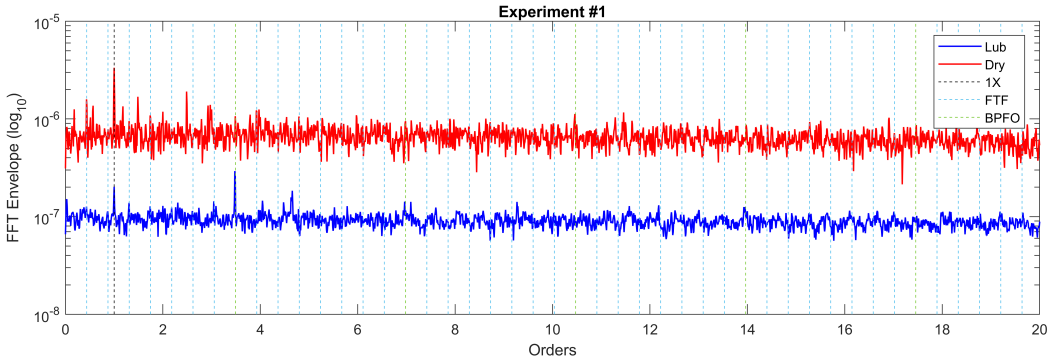


Figure 3.16: Envelope spectrum comparison between dry and lubricated conditions

the presence of a modulating frequency close to FTF. For the interference conditions, the presence of the FTF or BPFO is not clear since the signal present multiple frequencies close to these values but is not possible to match the harmonics (Figure 3.17). Experiments #4 to #6 show an increase of the BSF with sidebands close to the FTF.

Table 3.2: Characteristic frequency results summary

| Experiment | Conditions | FTF | BPFO | BPFI | BSF |
|---|---|---|---|---|---|
| E1 | Lub | None | High | None | None |
| | Dry | Medium | Low | None | None |
| | Dry + 5mils | Not Clear | None | None | None |
| E2 | Lub | Low | High | None | None |
| | Dry | Medium | Medium | None | None |
| | Dry + 5mils | Not Clear | Not Clear | None | None |
| E3 | Lub | None | High | None | None |
| | Dry | High | High | None | None |
| | Dry + 5mils | Not Clear | Not Clear | None | High |
| E4 | Lub | Medium | High | None | None |
| | Dry | low | High | None | None |
| | Dry + 5mils | Not Clear | None | None | High |
| E5 | Lub | Medium | High | None | None |
| | Dry | low | High | None | None |
| | Dry + 5mils | Not Clear | Not Clear | None | High |
| E6 | Lub | low | High | None | None |
| | Dry | High | Low | None | None |
| | Dry + 5mils | Not Clear | Not Clear | None | High |
| E7 | Lub | High | High | None | None |
| | Dry | High | High | None | None |
| E8 | Lub | High | High | None | None |
| | Dry | High | High | None | None |
| E9 | Lub | High | High | None | None |
| | Dry | High | High | None | None |
| E10 | Lub | High | High | None | None |
| | Dry | High | High | None | None |
| E11 | Lub | Medium | High | None | None |
| | Dry | Medium | High | None | None |
| E12 | Lub | High | High | None | None |
| | Dry | Medium | High | None | None |

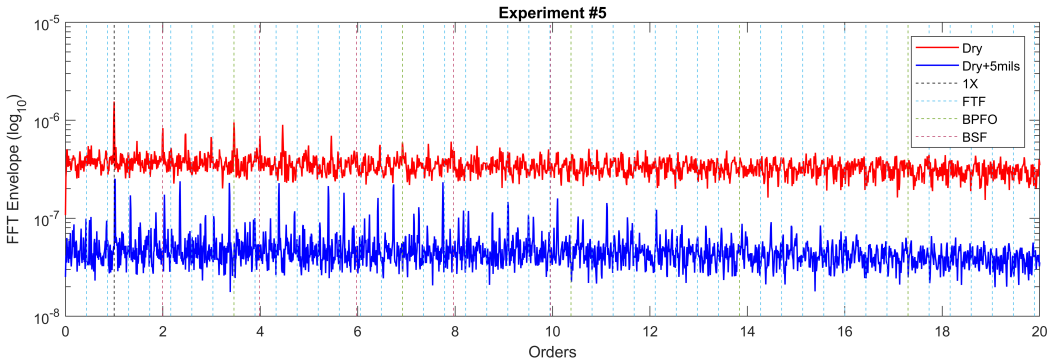


Figure 3.17: Interference conditions of Experiment #4 shows the problem of identify the frequencies with the known FF and BPFO.

### 3.4.3 Summary of Analysis

Twelve experiments are presented in the experimental results. Half of the twelve experiments are tested under lubricated, dry and interference conditions, the other half only under dry and lubricated. The envelope analysis is applied using FK as the filtering method. At least ten acquisition were taken for each condition in order to obtain an averaged spectrum and reduce noise. Finally the characteristic frequencies are found by observation with a maximum error of 16.4% for the case of the FTF

In conclusion, the vibration levels around the resonance frequency of the bearings increased under dry conditions. The interference condition decrease the vibration levels and the impulsivity of the signal, but is hard to determine the new vibration frequency components, only the BSF frequency is clearly identified. The BPFO frequency predominates in the spectrum of dry and lubricated conditions but the FTF also appears frequently. Further research should be conducted to conclude if the origin of the FTF.

The experiments supports the model of Sawalhi were the balls impact the entrance of the load zone at the FTF frequency in the lubricated and dry conditions with a difference in magnitude due the lack of dissipation provided by the lubricant.

# 4. TORSIONAL VIBRATIONS

Bearing problems have been mainly studied through lateral vibrations where the methodology is well established and the characteristic frequencies are known. In the case of torsional vibrations little efforts have been conducted and no known frequencies associated with bearing problems are known. Moreover, lubrication starvation despite been one of the most common faults in bearings there are no precedents on the impact of lubrication on torsional vibrations. In this work is presented an effort to engage this problem using the traditional methodology of baseline comparison, in which starting from a healthy baseline, the time and frequency (order) domain are studied to detect differences that could be used as indicators. The disadvantage of this methodology is the sensitivity to operational conditions.

To start the analysis a simulator is developed to study the friction under lubrication starvation. The simulator is based on the skf model, EHL model and GW model presented in the first chapter. The SKF model is composed from four friction components, however, since the sliding friction is the only related to lubrication starvation the simulator is restricted to the effects of this component.

The simple test bench used for testing the TIMS sensor is also used to obtain preliminary results on lubrication starvation. The results of the preliminary tests contribute mainly to discover the potential problems with the experimentation procedure and help to plan the final tests on the Rotor-Kit test bench. The final section of this chapter is focus on the experiments realized on the Rotor-Kit with a detailed description of the procedure, results and analysis.

## 4.1 Numerical Simulation

A numerical simulation of the lubrication on torsional vibrations is presented in this section. To simulate lubrication starvation the parameter of minimum film thickness is fixed to zero, while for the case of a properly lubricated bearing the parameter is calculated by the EHL model. In order to simplify the computation procedure only the rotational degree of freedom ($\theta$) is considered.

The parameters of the bearing are the same as the 6204-2RS-10 used in the experiments B.2. The simulation starts by calculating the interference and the bearing material parameters as curvature and material parameters. Since the data of interest is the friction moment a constant speed or a speed profile is set at the beginning of the simulation. Based on the pre-calculated speed the cage speed and the angular position of each of the balls is calculated for the entire time of simulation.

Using the theory reviewed in Section 1.6 the load distribution for each ball is calculated based on the current position and static or dynamic load. Figure 4.1 shows the load distribution for two angular positions under the same static load, the load zone limits are given by Equation 1.33. As the balls enter the load zone the applied load start increasing until reaching the maximum load to later decrease until the exit of the load zone. This variation on the load will change the minimum film thickness of each ball, therefore the friction on each of them.

Based on the speed, load and materials of each ball, the friction moment is calculated using the theory covered in Sections 1.2, 1.3, and 1.4. Since the static load and the materials are constant for the experiments is possible to obtain a Stribeck curve by piloting the sliding friction component vs speed. As the speed increases the lubrication transitions from dry (Coulomb) friction to shear (Lubricant) friction as shown in Figure 4.2. The minimum film thickness and roughness value used are also plotted in the figure, there is a

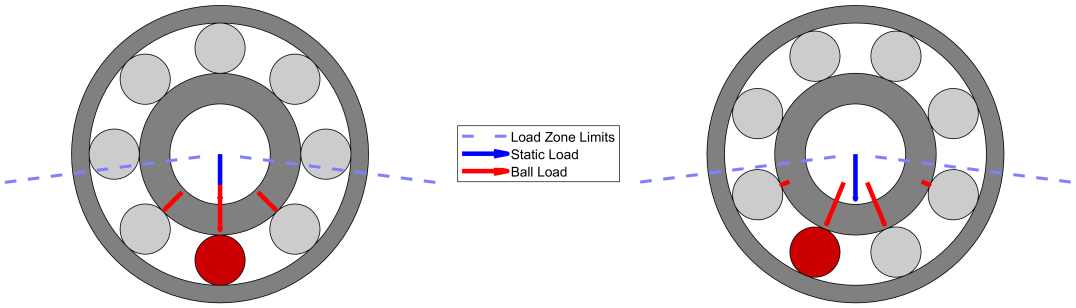


Figure 4.1: Load zone and load distribution depending on ball angular position

mixed regime zone close to the point were these two values intersect. This is the zone for lubrication starvation.

A steady state simulation is prepared to obtain the variations on the friction moment as the balls enter and leave the load zone. A constant velocity is used to simulate the bearing in steady state. The detection using torsional vibrations relies on the use of speed variations to identify lubrication starvation but for simplicity these effect is neglected to only obtain the friction force as a perturbation. In Figure 4.3 is presented the comparison between the dry and lubricated conditions for different loads. The main difference between load conditions is the increase in the magnitude as predicted by the Stribeck curve while the effect on the load is the softening in the transition of the balls into the load zone since the load is distributed in more balls.

A frequency analysis in the order domain shows that the signal is composed by a main frequency at 3X and its harmonics as shown in Figure 4.4. There is no difference in the magnitude of the frequencies. The DC component was removed for the analysis which is the main difference observed in the time domain analysis.

The magnitude of the sliding friction component is small compared to the usual motor driven systems as observed in the simulation, hence it could only impact the speed as soon as the driving motor is of low torque. Another observation is that the main effect

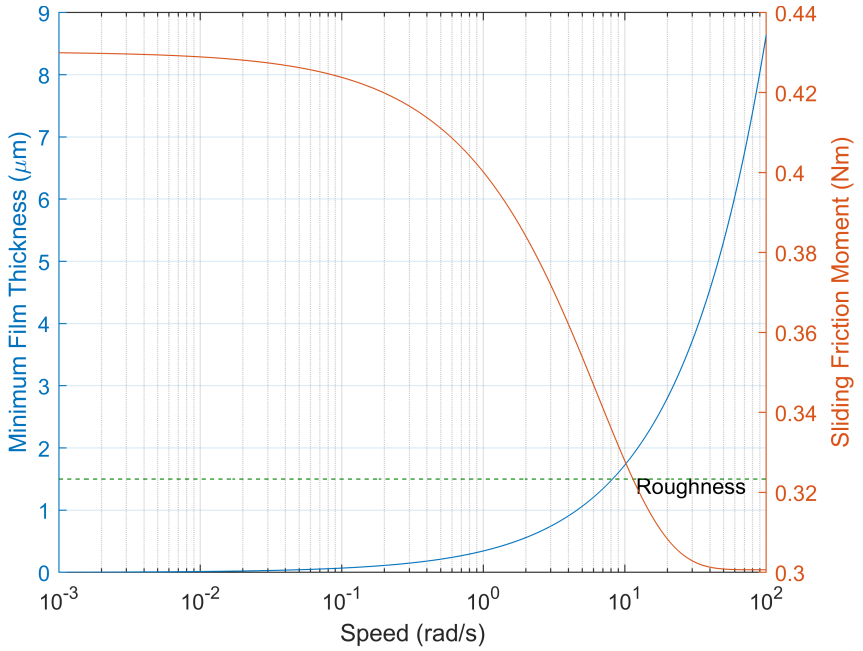


Figure 4.2: Stribeck curve of the transition between dry and lubricated friction

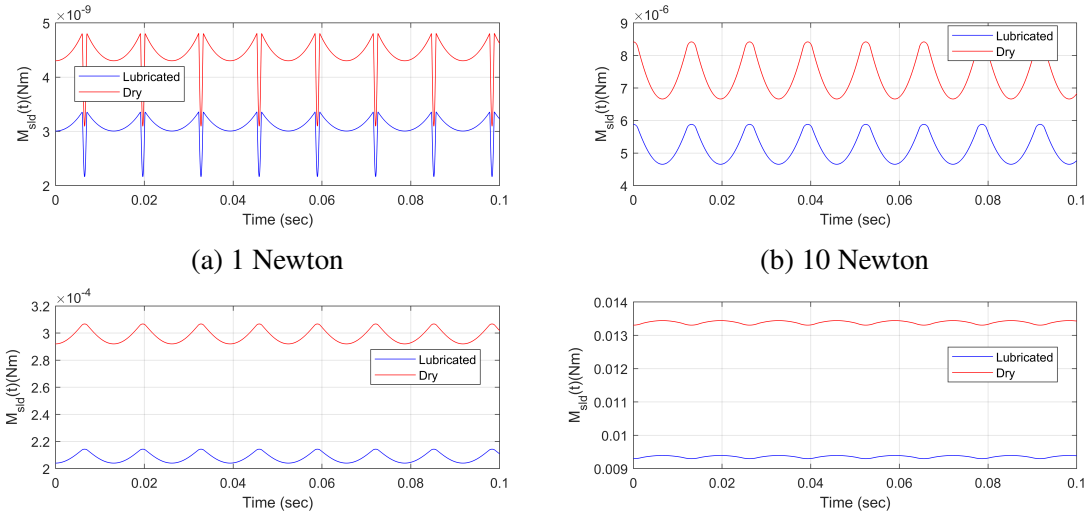


(a) 1 Newton

(b) 10 Newton

(c) 100 Newton

(d) 1000 Newton

Figure 4.3: Simulation of lubrication starvation effects on sliding friction moment

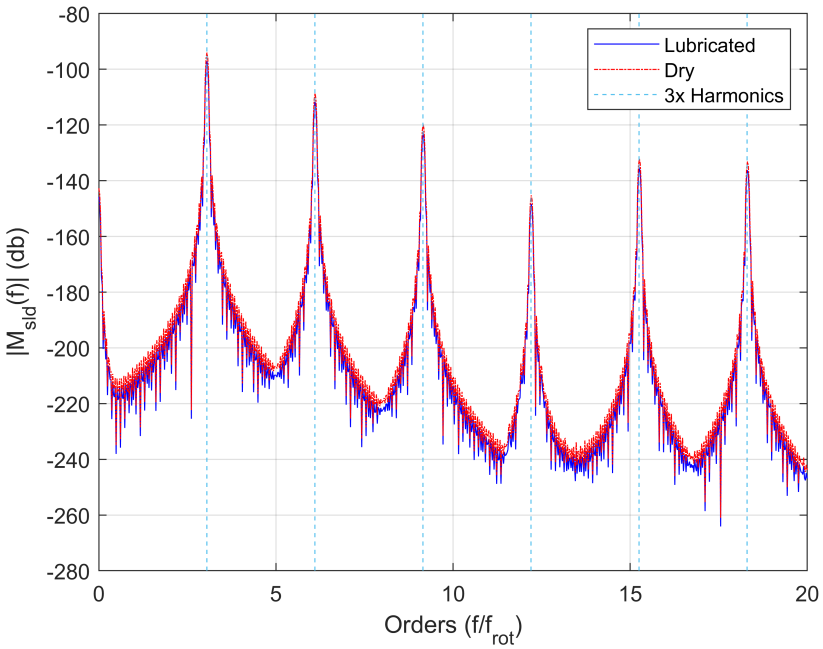


Figure 4.4: Order spectrum for simulation of lubrication starvation

of lubrication starvation is a decrease in efficiency on induction and synchronous motors since the energy instead of being used to move load it will be dissipated as heat. For the case of DC motors in open loop, the speed will be reduced due the increase in friction.

The simulation results also indicates that the effect of lubrication starvation is proportional to the load. Under light and medium loads the friction component is less than 10 micro Nm which is low compared to a normal motor torque. In real applications is expected that the bearings races will suffer scuffing (wear process due micro welding effects) hence the surface roughness will increase making the effect of lubrication starvation more evident.

## 4.2 Preliminary Experiments in Simple Test Bench

The simple test-bench used to test the TIMS sensor was also used to obtain preliminary results of bearings under dry conditions. The conditions for testing were light load, no

control over speed, and lubricant LGMT2. The control of speed was done by using the LCD tachometer as feedback to try to test at the same speed. The bearing tested is the 6204-2rs-12 which is for a $3/4$ shaft. The lubricant control follows the same procedure as described in Section 3.2. The objective of the preliminary experiments was to find the potential problems and a proper procedure for the final experiments in the Rotor-Kit and as secondary objective find a possible indicator of improper lubrication.

### 4.2.1 Experimental Procedure

For the first experiment a lubricated bearing is tested five times while trying to keep a constant speed of 300 rpm. After five acquisitions the bearing is removed and weighted in a precision scale to measure the original mass of the bearing. Later the bearing is cleaned with paint thinner to remove the grease and weighted again to obtain the amount of grease in the bearing. Finally the bearing is assembled again and tested five times under dry conditions. The goal of the first experiment is to identify indicators of lubrication starvation in the time and order domain.

For the second experiment two bearings are tested, one lubricated and one dry. The objective is to test the indicator found in the first experiment and validate it for different bearings. This time the bearings were tested nine times but at different speeds as shown in Table 4.1. An important point to mention is that the drill have two gear trains for different speeds and torques, the first gear train (low speed-high torque) is used for tests 1-4, while the second gear train (high speed-low torque) for test 5-9. The change in gear trains create noise and harmonics in the range of interest.

From the scale measurements the grease in the ball bearing is 1.628g and 1.67g for the first and second experiment respectively. Figure 4.5 presents a comparison between lubricated and dry conditions in the time domain. For the results of torsional vibrations is hard to distinguish characteristics that differentiate the two conditions as in comparison

| Experiment | Lubricated (rpm) | Dry (rpm) |
|---|---|---|
| 1 | 141 | 159 |
| 2 | 217 | 205 |
| 3 | 338 | 320 |
| 4 | 402 | 388 |
| 5 | 404 | 436 |
| 6 | 593 | 615 |
| 7 | 875 | 860 |
| 8 | 993 | 1039 |
| 9 | 1404 | 1497 |

Table 4.1: Speeds for second experiment

with the accelerometer signals where it was possible to observe impulsivity in the time domain, which could be measured by kurtosis or crest factor. Another problem found with this setup is to achieve a constant velocity and to repeat it, hence is not possible to use the RMS indicator. Based on this results the possibility to detect problems with lubrication in time domain is discarded. Instead the order domain is proposed due the advantage that the TIMS method use synchronous acquisition, this provide the advantage that peaks in order domain are sharper and constant despite the speed variations of the drill.

Figure 4.6 shows the results of the order domain analysis in which a difference in some orders could be used to compare the dry and lubricated conditions. For the preliminary tests the sensor was configure to store only 26 turns and was setup for 2400 ppr, but the data show low levels of vibrations above 600 orders. Due both problems is necessary to reduce the ppr to 1200 using the preset of the TIMS sensor and increase the FIFO size to store more than 100 turns.

### 4.2.2 Experimental Results

A band-pass filter is used to measure the power spectral density (PSD) of different sections of the order domain. An equiripple filter is design with a stop requirement of -60

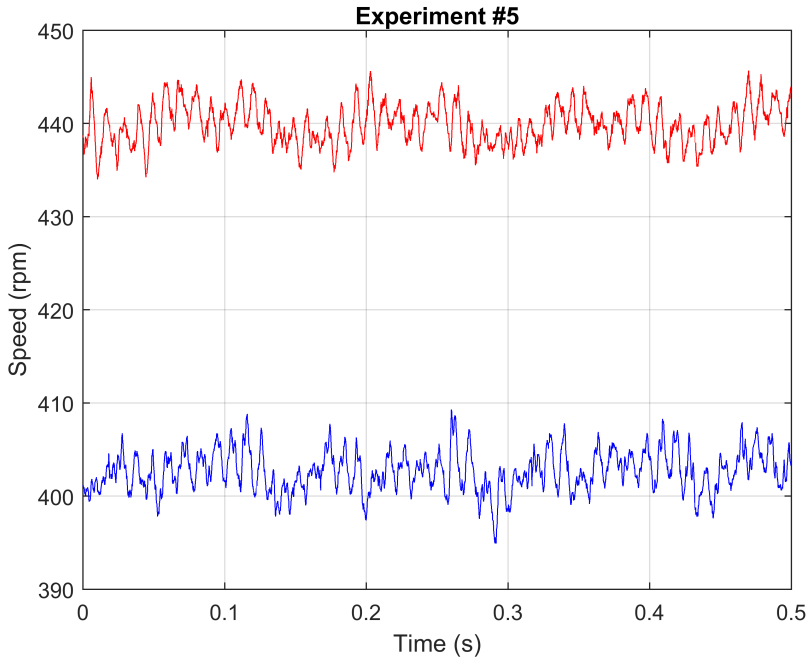


Figure 4.5: Preliminary test between lubricated and dry conditions

db and a pass requirement of 1 db. A swept of order ranges from 1-100 in increments of 10 orders is used to select the most affected range. The regions of 20-30, 30 -40 and 40-50 are the most affected, hence a band-pass filter from 20 to 30 orders is used to measure the power density in this region as shown in Figure 4.7. Since the speed varies from test to test a bar plot is used to compare the values from lubricated to dry conditions. In the graph is possible to observe an increase in power density for the dry test, therefore this region is proposed as the indicator of lubrication starvation for the experiment 2 where two different bearings are tested. By testing two bearing we eliminate the possibility that this region is related to the bearing geometry.

For the results of experiment 2 a similar analysis is performed, the PSD is obtained for each dry and lubricated test. The results are compared side to side in Figure 4.8 although the velocities are not exactly the same, hence the average speed between the two is displayed in the x-axis.

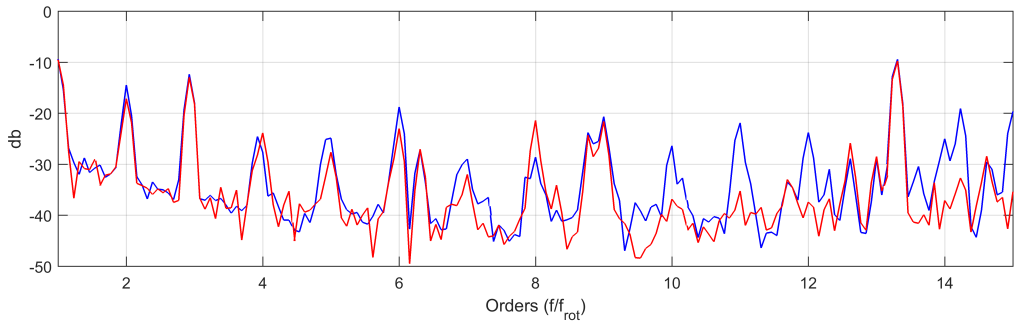


Figure 4.6: Preliminary results of experiment 1 analyzed in order domain

The main objectives of the experiments were to prove the sensor capabilities, a better experimental setup and to find an indicator of improper lubrication. The sensor proves adequate for the analysis since the main activity in the spectrum is in the range of 0-100 orders while the sensor could detect activity up to 600 orders. Moreover, the PSD indicator is valid in both tests and the order range is still the same even for different bearings. To validate the indicator in a more controlled test bench is necessary to use the Rotor-kit, in which the indicator could also be tested against changes of load.

The potential problems found in the preliminary experiments were the velocity control, which proves to be critical to find an indicator, the calibration of the TIMS sensor to use 1200 ppr instead of the 2400, and the need to increase the FIFO size to store more turns and improve the order resolution.

## 4.3 Torsional Vibration Experiments in Rotor-Kit

The Rotor-Kit experiments are prepared based on the preliminary experiments realized in the simple test bench and the potential problems found in the experimental procedure. Since the main problem with the simple test bench was the speed control, the rotor kit controls the parameter using a VFD. A series of experiments (Table 4.2) are done to test the effects of the VFD over torsional vibrations by using different shaft speeds and the

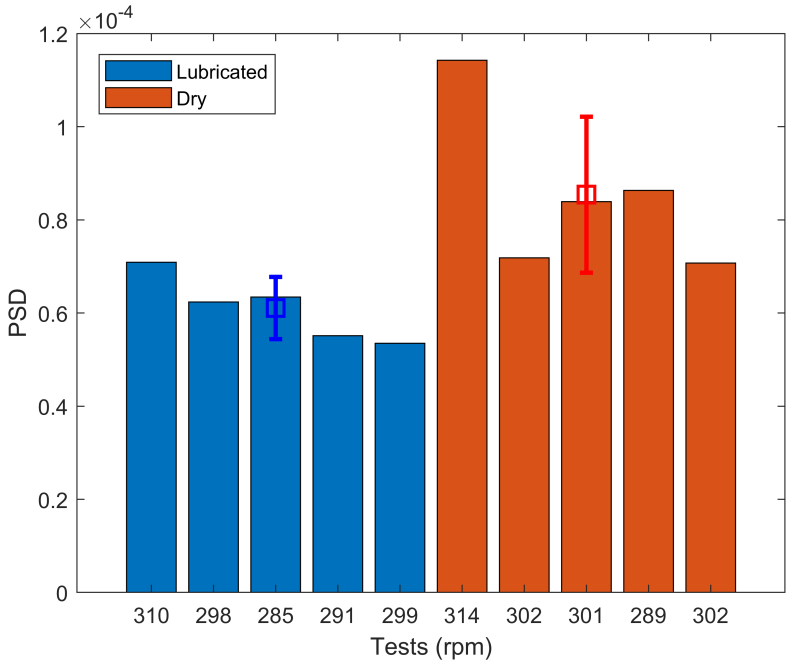


Figure 4.7: Power spectral density in the region of 20-50 orders from the preliminary results of experiment 1

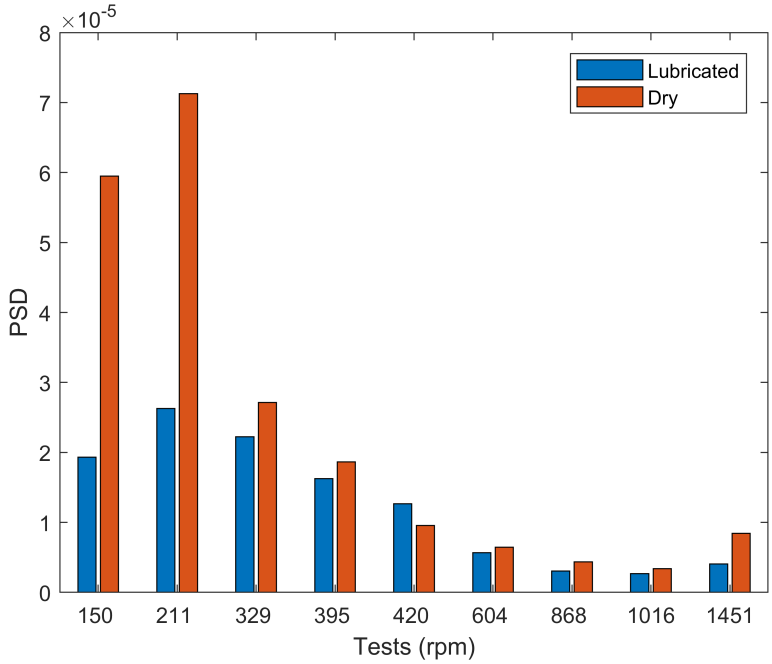


Figure 4.8: Power spectral density in the region of 20-50 orders from the preliminary results of experiment 1

| Test No. | ppr | Shaft Speed (Hz) |
|---|---|---|
| 1 | 2400 | 10 |
| 2 | 2400 | 10 |
| 3 | 2400 | 10 |
| 4 | 2400 | 20 |
| 5 | 1200 | 10 |
| 6 | 1200 | 20 |

Table 4.2: Encoder test for VFD effects.

change of ppr from 2400 to 1200 to study if there is any effects by increasing the frequency resolution.

From the order domain analysis shown in Figure 4.9 it seems the VFD has a huge influence for the 10 Hz test, since the peaks in 1.2X and 12.2X (12 Hz and 120 Hz) have energy leakage, which indicates a perturbation with fix frequency. For the case of the 20 Hz tests the influence of the VFD seems disappear close to 1X and remains close to 6X which corresponds to 120 Hz. There is also an increase in 8X with some energy leakage, this could be a mixture of fix frequency and harmonic of shaft speed. The improvement due change of ppr is appreciated between tests 3 and 5 where the peaks are more defined. Based on the results is decided that the experiments must be done in a frequency above 20 Hz and with a frequency in which harmonics do not match 120 Hz to distinguish it from the VFD perturbation.

A series of eight experiments to compare the difference between dry and lubricated bearings are done using 28 Hz for the shaft speed. The first experiment procedure is the same as the preliminary tests where the lubricated bearing is tested first then is removed and cleaned to test the bearing under dry conditions. The results are shown in Figure 4.10 where is possible to observe a difference in the 8th order. The dry results are divided in two sets, one for acquisitions with 2400 ppr and the second for acquisitions using 1200

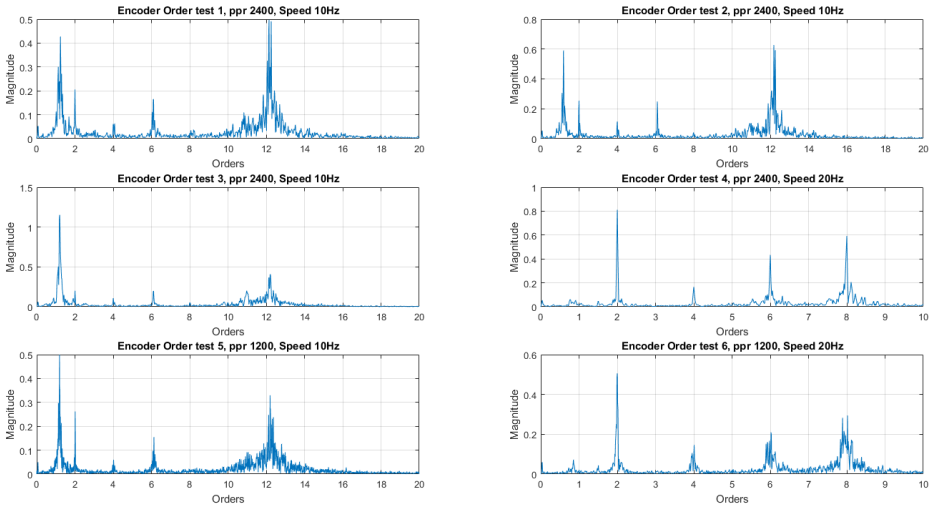


Figure 4.9: Torsional vibrations results from VFD analysis

ppr. The difference in resolution is more evident in this experiment.

Comparing the results of experiment 1 with the preliminary experiments, there is an appreciable difference between dry and lubricated. In the case of the preliminary results the difference was located between the 20th and 50th orders and the magnitude difference was below $1 \times 10^{-3}$. The PSD analysis for the signal with a band-pass filter between the 7th and 9th order is presented in Figure 4.11. In this analysis the difference is more evident between the two conditions and in the dry condition is observed that the vibrations levels increase as the bearing is heating up. For the second set of acquisitions with the ppr set to 1200 the vibrations decrease and start fluctuating in lower values, but still above the lubricated baseline, this could be related to the bearing reaching the operational temperature.

For experiment 2 a new level of lubrication is added to test the difference in vibrations. An increase in the 6th order and no variation in the 8th order are observed in the results presented in Figure 4.12. The lubricated test at 50% presents some activity in the 6th

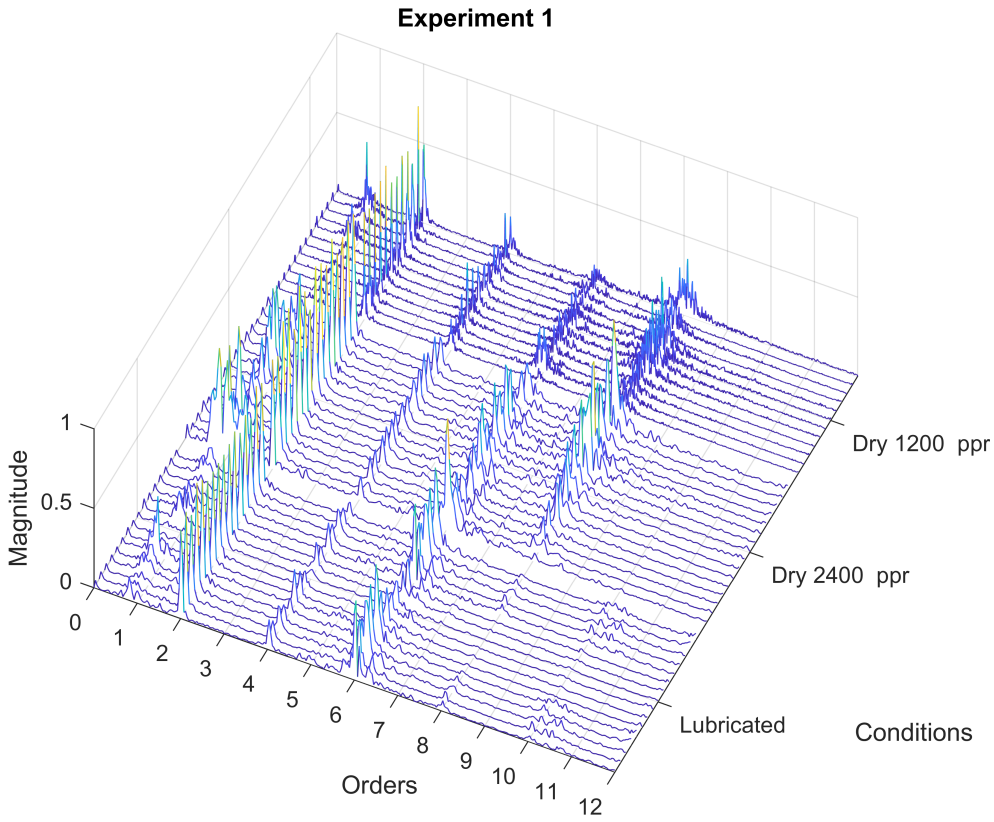


Figure 4.10: Order domain analysis for experiment 1

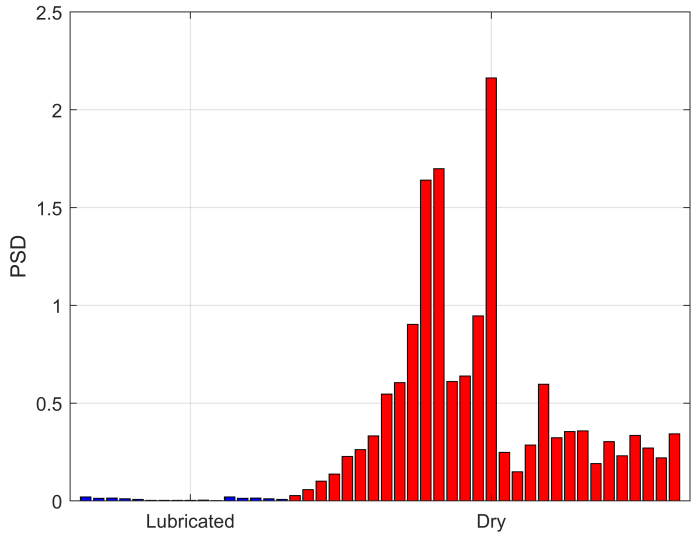


Figure 4.11: PSD comparison for 8th order

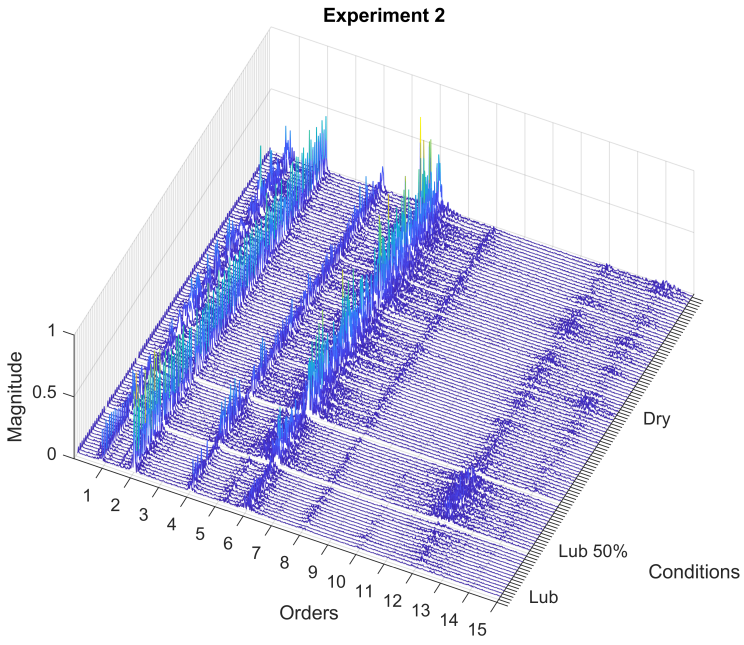


Figure 4.12: Order domain analysis for experiment 2

order as well. While the results are promising due the difference in vibration levels, the fact that the order with activity is not the same as the previous test (8th order) eliminates the possibility of using a certain order as an indicator for lubrication starvation. To validate the results of experiment 2 a third experiment shown in Figure 4.13 is done with the same procedure. In the results is possible to observe a small activity in the 11th order for the lubrication at 50% and the dry test, but on the contrary the vibrations in the 4th order decrease for dry conditions.

The difference in results between experiments 1 to 3 make it difficult to define a specific indicator of lubrication starvation. The variations are attributed to the experimental procedure where the bearings are dismounted in order to remove the lubricant which could change the shaft alignment and the torque at which the mounting screws are tighten. To solve the problem, a different procedure is establish in which the dry tests are performed

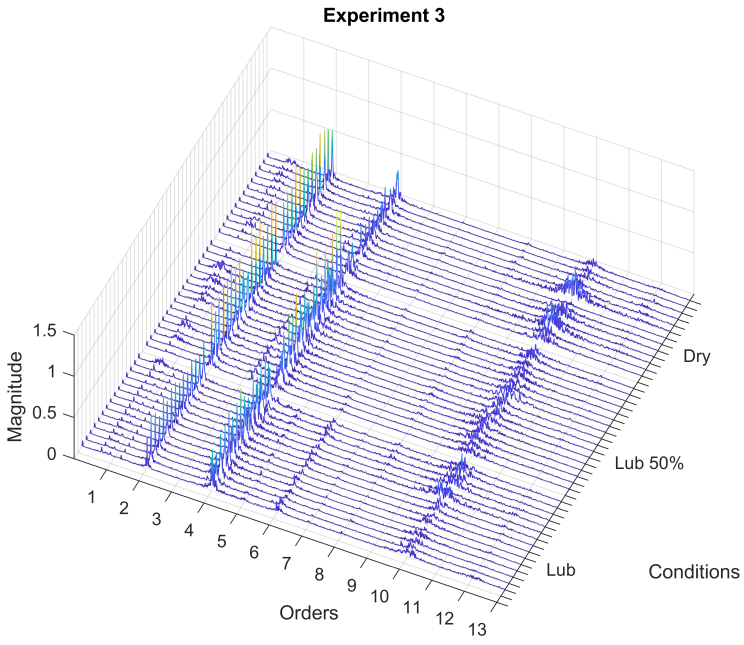


Figure 4.13: Order domain analysis for experiment 3

first and later the lubricant is added without dismounting the bearing from the shaft, also the screws are tightened using a torque wrench in order to control the interference parameter.

Experiments 4 to 7 shown in Figure 4.14 are performed with the new procedure. For these experiments the number of the FIFO were increased to 109 turns, hence the acquisition and transmission of data for one test take an approximate time of 6 minutes. The long time of transmission is the reason for these experiments to only have 3 to 4 tests for each condition. The advantage is the increase in resolution to more than 100 lines per order. Moreover, the intermediate lubrication level was decreased to 5%.

In the results is possible to observe that there is no difference between the lubricated, 5% lubricated and dry conditions. Therefore, is concluded the first three experiments were highly affected by the mounting procedure and difference in alignment. The results for

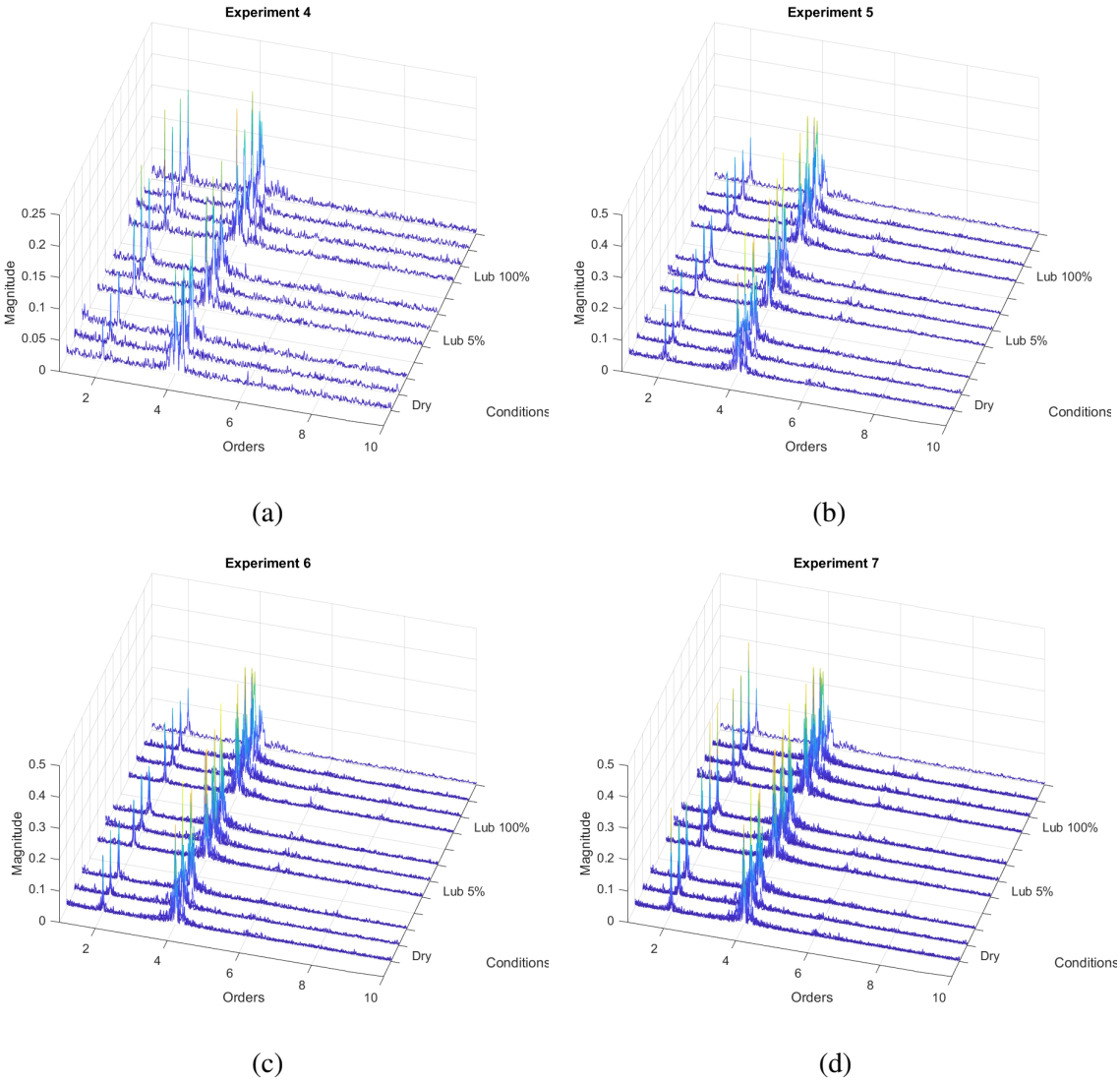


Figure 4.14: Order domain analysis for experiment 4 (a), 5 (b), 6 (c), and 7 (d)

the torsional vibrations conclude that is not possible to detect lubricaton levels using this method due the low level of perturbation generated by the change in friction. The experimental results agree with the simulation results in which for light to medium loads the friction component is not high enough to modify the speed or create torsional vibrations.

Further research should be conducted using torsional vibrations for bearing under high loads. The negative results of this research should not discourage further research on torsional vibrations. The results here obtained could help to define the limits and disadvantages of torsional over lateral vibrations or to be more specific, the advantages and disadvantages of the TIMS method.

# 5. ENERGY ANALYSIS

The energy consumption of industrial motor-driven systems account for 65% of the US electricity [77]. The motor energy losses could be due various reasons [78]:

- Stator winding resistance losses.
- Rotor conductor bar and end resistance losses.
- Stator and rotor core losses.
- Friction and windage losses. (Include bearing losses, wind resistance, and cooling fan load).
- Stray load losses (miscellaneous).

In this work is presented the analysis of efficiency of an induction motor of 3 Hp subject to friction losses due lubrication starvation, Bearing friction could account for 8 to 12% of total losses [77]. Previous work has been conducted to study the bearing faults impact on energy losses [79], cyclic (Outer race hole) and non-cyclic (Corrosion) faults were considered. From his results is concluded that non-cyclic faults are hard to detect using Motor Current Signature Analysis (MCSA) due the low effect on the torque, which are similar results as the one obtained in Chapter 4 of this work. But in the case of efficiency measurements a clear reduction was found even when the corrosion do not affect the inside races of the bearing.

Motor efficiency could be measured using a dynamometer to obtain the mechanical power output as stated in the testing procedure on the IEEE standard 112-2004 [80] and a wattmeter for the electrical power input to measure current and voltage. The measurements should be done in watts or kilowatts depending of the size of the motor.

The minimization of energy losses is critical to large motors since the energy cost could even match the cost of the motor. A condition based maintenance is critical to mantain the energy performance and remaining life of such large motors. Until now the usual condition monitoring covers mainly cyclic bearing faults as outer or inner race defects, but those faults are usually presented once the bearing is already damaged. Lubrication monitoring could be used to maximize the remaining life of the bearing instead of just detect an imminent failure, besides the potential energy savings justify the cost of implementing the monitoring system. As part of this work a case study is presented where the motor population of a medium size plant is assumed to be under poor lubrication conditions. The energy savings are used to calculate a simple payback that justifies the implementation of a predictive maintenance program.

## 5.1 Experimental Setup

The Rotor-Kit is prepared to realize energy efficiency measurements using voltage and current probes for the electrical power input while for the mechanical power output a dynamometer is coupled between the motor and the rotor with the loaded disks.

For the first part of the experiments the rotor is light loaded since there is only a light static load but the rotor is not subject to any rotational load, six experiments under this conditions were performed. For the second part of the experiments the rotor is coupled to a 3 Hp generator to act as a full load to the motor and the rotor is loaded with 7.5 kg to test different friction coefficients. The shaft is speed is set to 28Hz since the tests were performed in parallel with the lateral and torsional vibrations measurements.

The data is acquired through a National Instrument acquisition system and a LabVIEW interface. A complete description of the experimental setup could be found in Chapter 2 and the calibration procedure for the sensors used is found in Section B.1.

Electrical power input is usually measured using the RMS value of voltage and current

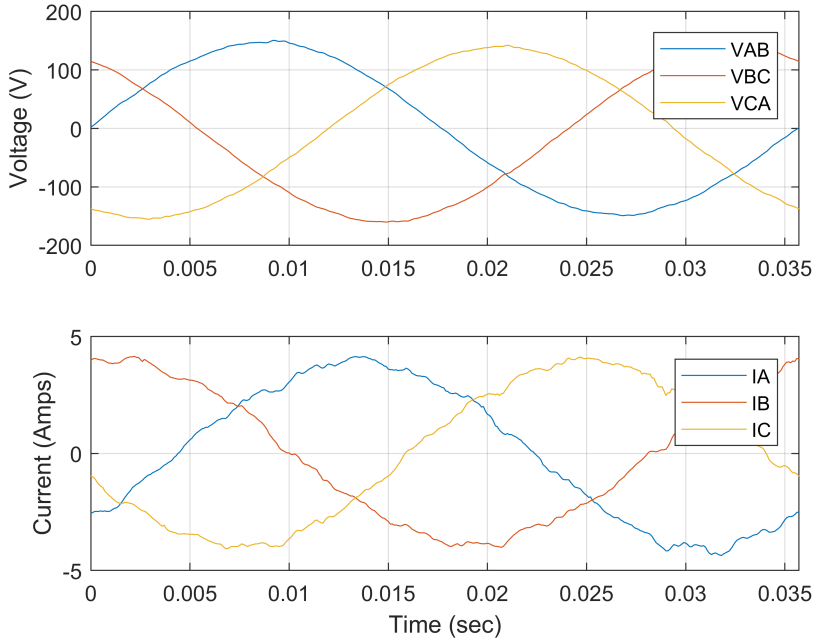


Figure 5.1: Voltage and current measurements for light load conditions

over certain number of cycles for each line and then an average is taken. The power factor could be measured (usually provided by the wattmeter) to measure the real electrical power instead of the apparent electrical power, this is useful in the case of measuring mechanical losses. For the case of out laboratory setup, is possible to measure the instant electrical power on each line by having the time data of voltage and current as shown in Figure 5.1.

Using Equation 1.64 the RMS of the instantaneous electrical power input is calculated. Before applying this equation the voltage line to line should be transformed to voltage line to neutral using Equations 1.66 to 1.68. The transformation change the phase of the lines by $30°$. The switch in phase step is essential to take in account the correct power factor which is the phase between the voltage and current line to neutral as shown in Figure 5.2. Usually a power factor close to $90°$ indicates a pure inductive load which in our case is due the light load or no load conditions of the motor, is expected that as the load increases the power factor decreases.

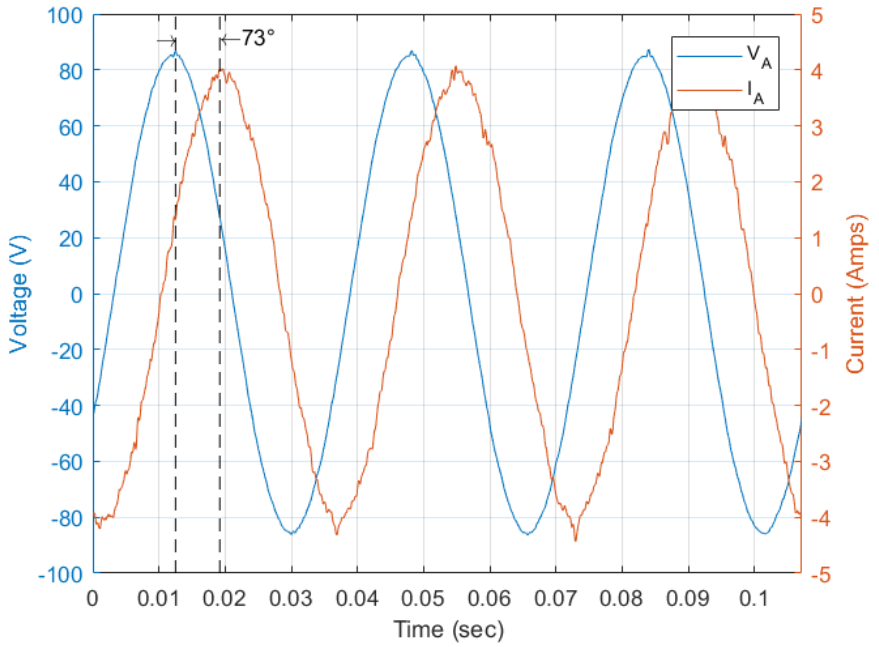


Figure 5.2: Phase between voltage and current line to neutral

The electrical power input is then calculated for each phase and added to obtain the total electrical power input. The results are presented in Figure 5.3a were is observed that for each test the electrical input power changes but there is no correlation with respect the bearing conditions. This is important to mention, since a method used to calculate the efficiency is to assume a constant load and calculate the change in efficiency with only the voltage and current input, but as observed here is necessary to also measure the mechanical power output to obtain the real change in efficiency. The mechanical power output of the motor is calculated using Equation 1.69 and the results are shown in Figure 5.3b. For this calculation the torque should be measured in Nm and the speed in rad/sec.

Once obtained the electrical power input and mechanical power output of each experiment the energy efficiency is calculated using Equation 1.63. Figure 5.4a presents the results for the energy efficiency tests for dry and lubricated conditions under light load. Observing the data we could conclude that the motor has a low efficiency even for lubri-

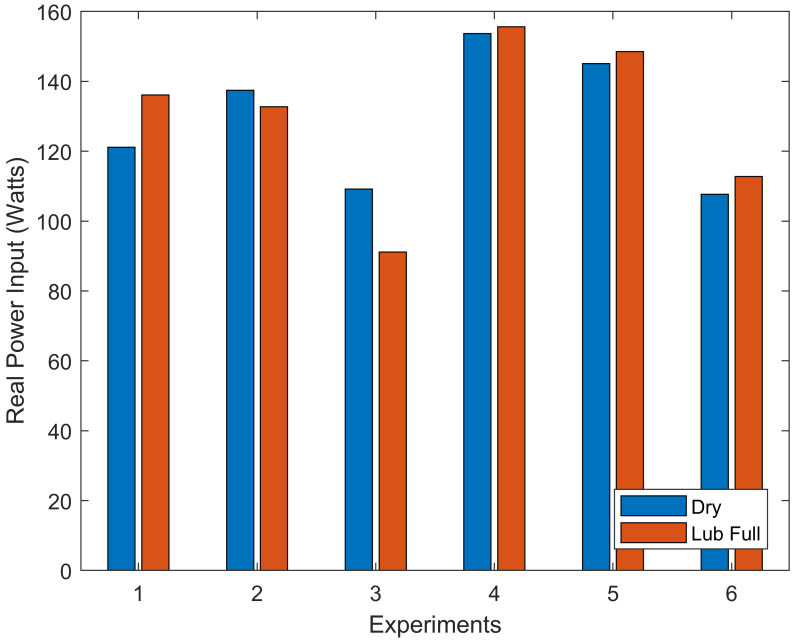


(a)

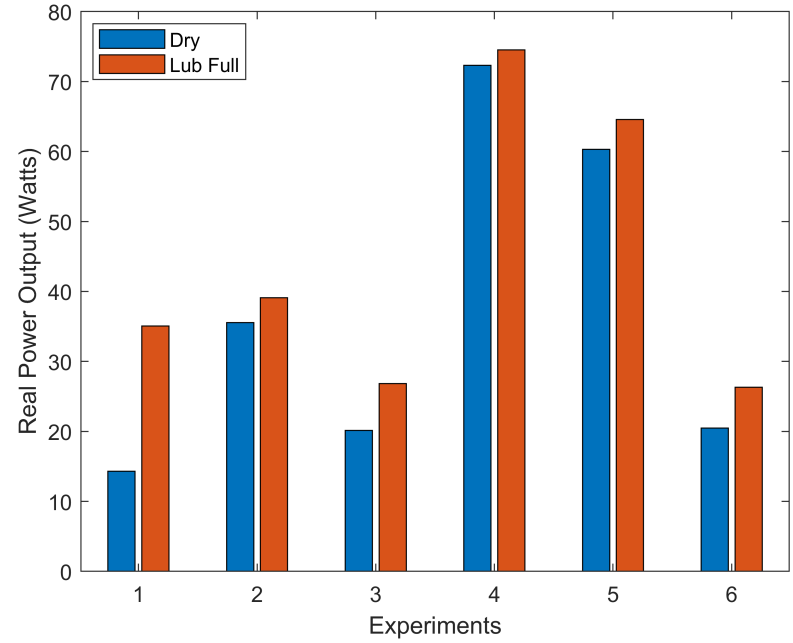


(b)

Figure 5.3: Total eletrical power input (a) and mechanical power output (b) under light load

| Factors | Load 36% | Load 62% | Load 68% | Load 73% | Load 79% |
|---|---|---|---|---|---|
| **Dry** | Dry / L36% | Dry / L62% | Dry / L68% | Dry / L73% | Dry / L79% |
| **Lub 5%** | Lub5% / L36% | Lub5% / L62% | Lub5% / L68% | Lub5% / L73% | Lub5% / L79% |
| **Lub 100%** | Lub100% / L36% | Lub100% / L62% | Lub100% / L68% | Lub100% / L73% | Lub100% / L79% |

Table 5.1: Design of experiment for energy analysis under different loads and conditions

cated conditions since is working under light load, but even under light load the efficiency of the motor decreases due lubrication starvation reaching levels as low as 0.13 (Experiment 1).

To perform an energy analysis, it is more convenient to use the percentage of efficiency reduction as shown in Figure 5.4b, here we could use the best case number of 4% from experiment 4 to obtain conservative values of energy savings. The variations of efficiency reduction observed in each experiment could be due the light load of the rotor, hence to minimize the effect on efficiency calculations is necessary to perform experiments at higher loads.

## 5.2 Variable Load Experiments

The free load tests presented in the last section were done without the generator and static load upgrades described in Section 2.3, hence the results are just valid for the motor under low or free load (Level 0). Since the efficiency of the system is highly dependent of the load factor, an extensive experiment to test the lubrication starvation effect under different load factors is presented in this section. The design of the experiment for each bearing tested is presented in Table 5.1, each test condition is acquired five times to obtain the mean to be used for efficiency calculations. A total of nine bearings were tested, hence a total of 675 samples are used for the experiment.

Comparing the results of the experiment for all bearings is possible to obtain the curve

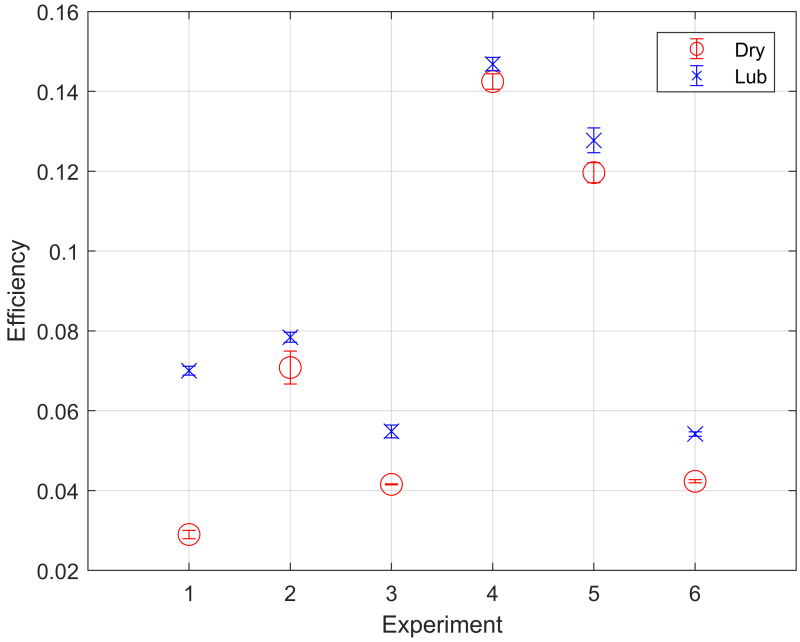


(a)

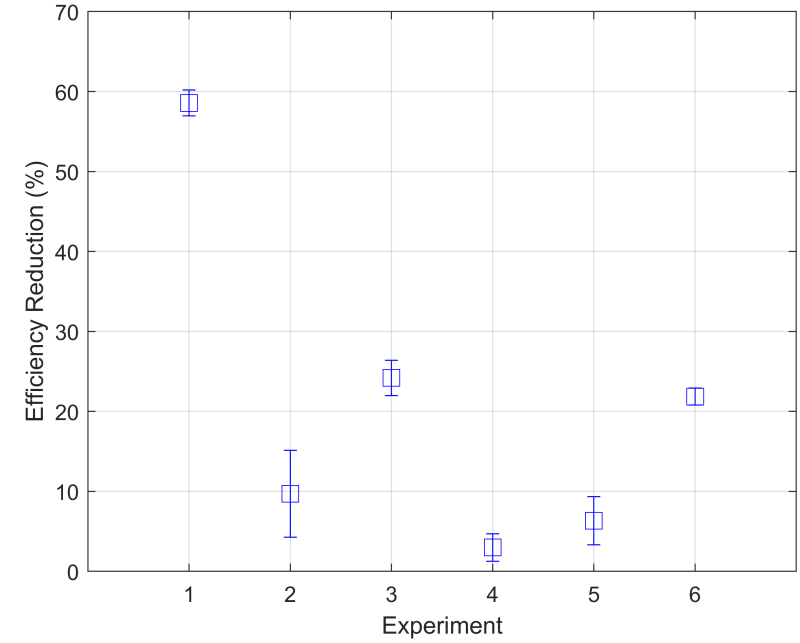


(b)

Figure 5.4: (a) Energy efficiency of dry vs lubricated conditions; (b) Reduction in energy efficiency due lubrication starvation

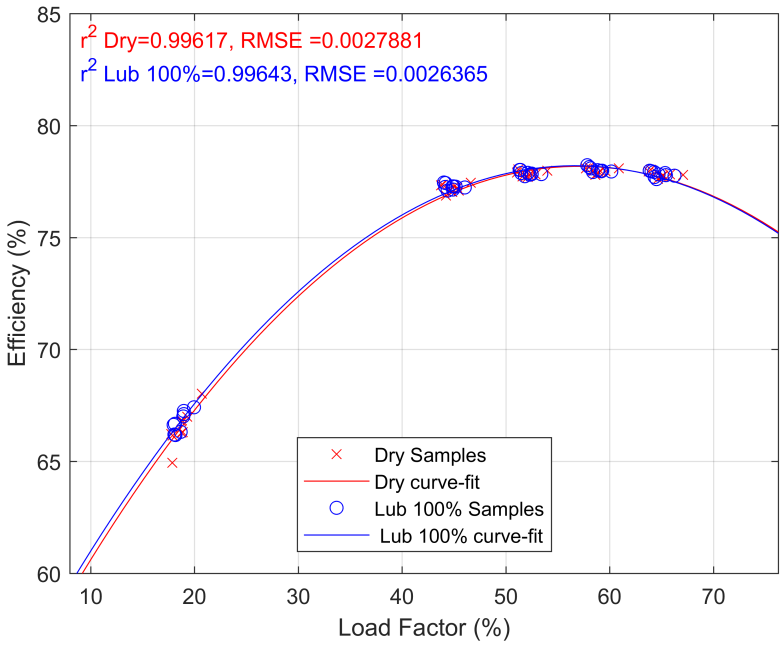


Figure 5.5: Efficiency vs load for dry and 100% lubricated conditions

fitting for the dry, 5% lubricated, and 100% lubricated samples as shown in Figure 5.5 and 5.6. In the efficiency curves is possible to observe that for low loads the efficiency difference is higher than for high loads. This could be related to the fact that the energy dissipated by friction is constant, hence for low loads the ratio the mechanical power loss due friction is considerable compared to the mechanical power output to move the load, but for high loads the mechanical power loss due friction is minimal compared to the mechanical power used to move a higher load.

Figure 5.7 shows the decrease in efficiency between lubricated and the other two conditions. We could observe in the comparison that around 0.3% of the efficiency could be reduce under dry conditions at low loads, but for high loads the efficiency decrease is almost negligible.

As conclusion of the experiments when a motor is working at full load the energy efficiency loss due lubrication starvation could be neglected but when a motor is working

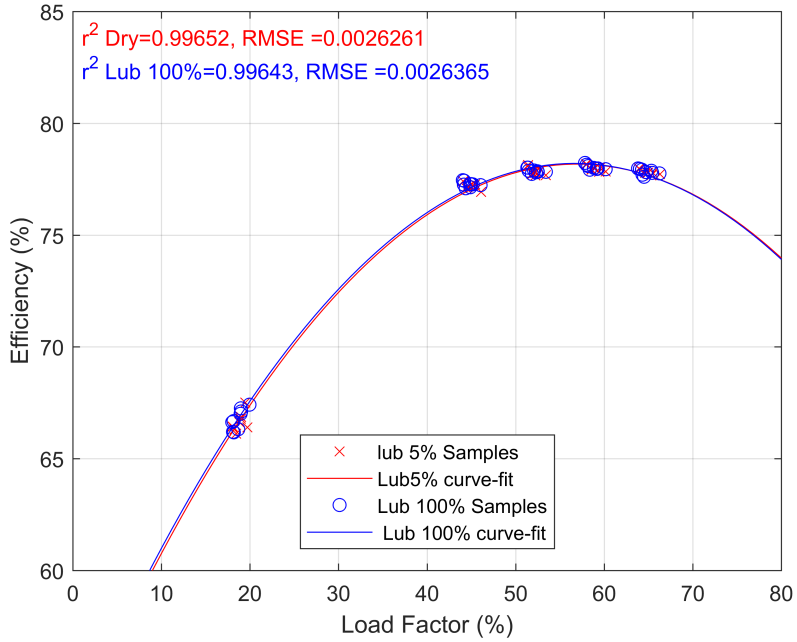


Figure 5.6: Efficiency vs load for 5% and 100% lubricated conditions

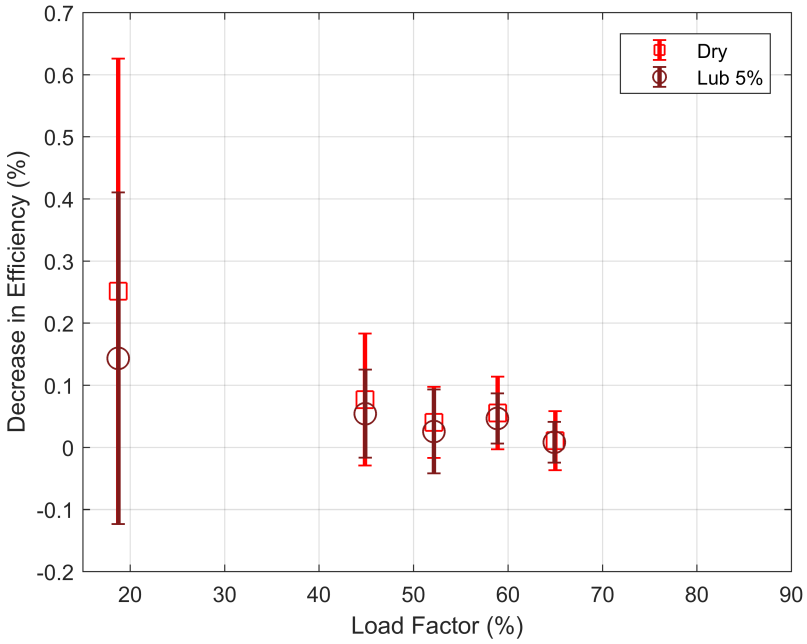


Figure 5.7: Decrease in effciency due lubrication starvation

| Motor | Power (Hp) | Qty | Total Power (Hp) | Load Factor | Duty Factor | Efficiency |
|---|---|---|---|---|---|---|
| Blower Tower 1 | 50 | 1 | 50 | 0.75 | 0.8 | 90% |
| Blower Tower 2 | 25 | 1 | 25 | 0.75 | 0.8 | 90% |
| QSI Compressor | 200 | 1 | 200 | 0.75 | 0.8 | 97% |
| Extruder motor | 25 | 1 | 25 | 0.75 | 0.8 | 90% |
| Molds Pumps | 20 | 10 | 200 | 0.75 | 0.8 | 93% |
| Mill Motor | 200 | 1 | 200 | 0.75 | 0.8 | 95% |
| Small Mill Motor | 150 | 1 | 150 | 0.75 | 0.8 | 93% |
| Mold Injection | 50 | 3 | 150 | 0.75 | 0.8 | 93% |
| Grinder | 200 | 1 | 200 | 0.75 | 0.8 | 92% |

Table 5.2: Motor list for case study

under a varying load lubrication starvation could impact the energy consumption of the equipment.

## 5.3 Case Study

Based on the results of efficiency obtained in the previous section a case study is presented using a real motor inventory from a rubber company. The maintenance crew has a policy of run to failure motor maintenance which leads to a downtime of one month in one of the pumps during the past year. The motor list is shown in Table 5.2, the values of efficiency and mechanical power were obtained from the nameplates, the load factor was estimated during the assessment and the duty factor was obtained based on information from the plant personnel. Table 5.3 summaries the plant information needed to calculate the energy savings.

Using a hand held vibrometer the low and high frequency RMS value of 10 motors were measured. Table 5.4 presents the results of the assessment in which two motors present high levels of vibrations based on the ISO standard 10816 and one motor present high frequency vibrations that could be related to bearing problems.

| Plant information | Value | Units |
|---|---|---|
| Avoided Cost of Electrical Energy | 0.069 | $/kWh |
| Avoided Cost of Electrical Demand | 6.0 | $/kW· mo |
| Operating Hours | 4,368 | hrs |
| Total Annual Consumption | 6,098,227 | kWh |
| Avg Month. Consumption | 508,185 | kWh |
| Total Annual Demand | 7,837 | kW |
| Avg. Month. Demand | 653 | kW |
| Annual Revenue | 17 | MMdlls |

Table 5.3: Summary of plant statistics

| Motor | Low Frequency RMS (mm/s) | High Frequency RMS (g) | Diagnostic |
|---|---|---|---|
| 1 | 9.8 | 0.5 | Low unbalance in fan blades |
| 2 | 5.8 | 2 | Low vibrations due motor impeller |
| 3 | 15.2 | 0.7 | High rotor unbalance |
| 4 | 1.6 | 0.2 | Healthy |
| 5 | 1.2 | 1.5 | Low bearing vibrations |
| 6 | 1.5 | 0.9 | Healthy |
| 7 | 1.7 | 0.5 | Healthy |
| 8 | 11.52 | 1.4 | High problem with pump impeller |
| 9 | 9.2 | 1.46 | Low vibrations due motor impeller |
| 10 | 3.1 | 1.2 | Healthy |

Table 5.4: Vibration measurements on sample motors.

The assumption for the case study based on the motor condition and the maintenance policy is that the lubrication is not properly maintained, hence the energy loses due lubrication starvation is 0.2%.

To calculate the energy savings the following equations are used

$$E_C = \frac{(P_T)(0.746\ \frac{kW}{Hp})(LF)(DF)(T_O)}{\eta} \tag{5.1}$$

$$E_P = E_C\,(1 - 0.04) \tag{5.2}$$

$$E_S = E_C - E_P \tag{5.3}$$

$$E_{CS} = E_S \cdot C_E \tag{5.4}$$

$$D_C = \frac{(P_T)(0.746)(LF)(12\ \frac{mo}{yr})}{\eta} \tag{5.5}$$

$$D_P = D_C\,(1 - 0.04) \tag{5.6}$$

$$D_S = D_C - D_P \tag{5.7}$$

$$D_{CS} = D_S \cdot C_D \tag{5.8}$$

$$T_{CS} = E_{CS} + D_{CS} \tag{5.9}$$

where, $P_T$ is the total motor power and the units is $Hp$. $LF$ and $DF$ are the load factor and duty factor respectively. $T_O$ is the operating hours given in $hrs$, $\eta$ is the motor efficiency. $E_C$, $E_P$ are the current and proposed energy usage, and their unit is $\frac{kWh}{yr}$. $D_C$ and $D_P$ are the current and proposed demand usage, and their unit is $\frac{kW \cdot mo}{yr}$. $E_S$ and $D_S$ are the energy and demand savings and their unit is $\frac{kWh}{yr}$ and $\frac{kW \cdot mo}{yr}$, respectively. $E_{CS}$, $D_{CS}$ and $T_{CS}$ are the energy, demand, and total cost savings respectively and their unit is $\frac{\$}{yr}$.

Table 5.5 present the results for energy calculations where the total energy savings are approximately $450 dlls per year.

The cost of a hand held vibrometer with the capability for testing high frequency vibrations is approximately $495 dollars [1]. The vibrometer could detect the RMS of high frequency spectrum, which is not the best indicator of lubrication starvation but if there is an initial baseline of healthy conditions it could be used instead of kurtosis or crest factor. Considering the cost of the system and the annual savings the simple payback is 1.1 years or 13 months.

The payback do not include downtime cost that could be approximated by diving the total annual revenue and the operating hours giving approximately $3,900 dlls per hr. Considering that the plant had a downtime period of one month for one of the machines, even considering a decrease of 10% downtime the savings are more than $140,000 dlls per year. Another factor to consider is the savings in repair/replacement cost, since with a predictive maintenance program the cost of reconditioning is 1/3 of the rewind cost.

In conclusion, the condition monitoring of motors and specially in ball bearings is fairly inexpensive compared to the avoided energy cost and downtime costs. The research invested in these areas could help to save money, energy and even lives. Further research should be conducted to evaluate the effects of lubrication starvation for longer periods since the bearing will suffer fast wearing and fatigue due the lack of lubrication that could increase the power loss in the bearing.

[1] https://www.testproductsintl.com/condition-based-monitoring/9070-smart-vibration-analyzer/

Table 5.5: Motor energy analysis

| **Motor** | **Current Energy Usage (kWh/yr)** | **Proposed Energy Usage (kWh/yr)** | **Energy Savings (kWh/yr)** | **Energy Cost Savings ($/yr)** | **Current Demand Usage (kW·mo)/yr** | **Proposed Demand Usage (kW·mo/yr)** | **Demand Savings (kW·mo)/yr)** | **Demand Cost Savings ($/yr)** | **Total Cost Savings ($/yr)** |
|---|---|---|---|---|---|---|---|---|---|
| Blower Tower 1 | 108,618 | 108,400 | 217 | $15 | 373 | 372 | 1 | $4 | $19 |
| Blower Tower 2 | 54,309 | 54,200 | 109 | $7 | 187 | 186 | 0 | $ 2 | $ 10 |
| QSI Compressor | 405,206 | 404,395 | 810 | $ 56 | 1,392 | 1,389 | 3 | $ 17 | $ 73 |
| Extruder motor | 54,309 | 54,200 | 109 | $ 7 | 187 | 186 | 0 | $ 2 | $ 10 |
| Molds Pumps | 420,455 | 419,614 | 841 | $ 58 | 1,444 | 1,441 | 3 | $ 17 | $ 75 |
| Mill Motor | 411,604 | 410,780 | 823 | $ 57 | 1,413 | 1,411 | 3 | $ 17 | $ 74 |
| Small Mill Motor | 315,341 | 314,711 | 631 | $ 44 | 1,083 | 1,081 | 2 | $ 13 | $ 57 |
| Mold Injection | 315,341 | 314,711 | 631 | $ 44 | 1,083 | 1,081 | 2 | $ 13 | $ 57 |
| Grinder | 425,025 | 424,175 | 850 | $ 59 | 1,460 | 1,457 | 3 | $ 18 | $ 76 |
| **Total** | **2,510,208** | **2,505,187** | **5,020** | **$ 346** | **8,620** | **8,603** | **17** | **$ 103** | **$ 450** |

# 6. SUMMARY AND CONCLUSIONS

The problem of lubrication starvation on ball bearings was addressed using two different measurment techniques that were implemented in a test bench called Rotor-Kit. Several experiments were performed to test the bearing under dry and lubricated conditions. Finally an energy analysis was presented to justify the research efforts on the topic.

The experimental test-bench Rotor-kit is prepared to perform several common rotor faults including bearing faults. The system is capable of measure torsional vibrations, lateral vibrations, torque, speed, voltage, current, bearing temperature and the strain in the bearing housing. Moreover, the system is also prepared to perform condition monitoring using vibrations, motor current signature analysis (MCSA) and temperature. After the upgrade the system is now able to perform energy analysis on rotor machinery components by measuring the power input and power output.

A new sensor based on the TIMS method and FPGA technology was developed. The sensor is capable of measure high frequency torsional vibrations with a high resolution due the large capacity of storing more than 110 turns and use a high speed clock of 100 Mhz with the possibility to increase it up to 200 Mhz. The FPGA proves to be a flexible technology to develop an advance prototype in a short time. If desired, the prototype could be transfer into an applicable specific integrated circuit (ASIC) for mass production. Further research is needed to implement more advance methods for measuring torsional vibrations, as for example the use of two encoders to measure the deflection in certain sections. The speed of transmission could also be improved using a communication protocol faster than the RS-232.

The lateral vibration analysis of lubrication starvation provide new information regarding the origin of the characteristic signal of lubrication starvation. Three indicators were

tested to compare their performance to detect lubrication starvation. The main characteristic of lubrication starvation was found to be the impulsivity which is measured by Crest Factor and Kurtosis. Kurtosis proves to be a more efficient indicator than Crest Factor since is capable of separate the test conditions by levels of damage. Besides, Crest Factor decrease as the fault reach critical levels when the sensor reaches the saturation levels which could lead to miss a fault during a real life application. Kurtosis indicator is improved by applying the Fast-Kurtogram which find the frequency region most affected by the impulsivity, the improved indicator could detect even low levels of lubrication.

By increasing the interference of the bearing was possible to prove that the origin of the characteristic signal of lubrication starvation is the excess of clearance. This extra clearance is created when the lubricant is removed leaving gaps between the components. The gap allows the bearing components to move and start colliding between them. Moreover, the lubricant also acts as a damping component dissipating the impacts, specially the impact when the balls enter the load zone. This impact happens due the bottleneck created at the entrance of the load zone.

The fast-kurtogram could also be used to apply the envelope analysis of the filtered signal. The envelop analysis of the experiments show the presence of the BPFO component for lubricated and dry tests proving the existance of the bottleneck at the entrance of the load zone. Moreover, the FTF component also appear consistenly across all experiments. The origin of this component could be related to the load zone as well but there is no clear explanation for the appearance of this component. Additionally, the FTF has been reported before in lubrication starvation tests realized by Boškoski et al., but in this case the bearing was under pure axial load. The pure axial load dissapear the load zone, hence no BPFO component is reported in their results. No conclusions could be done from the results of the interference test using envelope analysis since no clear components were detected, except for the BSF that appear in four of the six experiments.

From the results could be concluded that the criteria to diagnose lubrication starvation could be based on the following indicators. A high impulsivity in the signal or values of Kurtosis above 10, an increase in the bearing housing temperature and the presence of the BPFO and FTF components in the envelope analysis.

A simulator was developed to study the sliding friction component behaviour for lubrication starvation and under different loads. The behavior of the friction show that under lubrication starvation the magnitud of friction is amplified but the frequency content remains the same. The levels of the calculated friction were expected to be too low to affect the velocity or to appear in the torsional vibrations spectra. The simulated results were corroborated in the experiments where no difference was observed from lubricated to dry tests. The torsional vibrations measurements prove to be extremely sensitive to the mounting procedure, since at the beginning the results were greatly affected by the experimental procedure. The recommended procedure for lubrication starvation is to first test the bearing under dry conditions and add the lubricant without dismounting the bearing.

An energy analysis of lubrication starvation was performed using the Rotor-Kit capabilities to measure voltage, current, torque and speed. The energy analysis results for a light loaded rotor were that the efficiency could be reduced from 4 to 60% under dry conditions. Hence, great energy savings could be achieved by lubricating the bearing properly and implementing a predictive maintenance program as shown in the case study presented in Chapter 5.

## 6.1 Unique Contributions

The unique contributions of this work are:

- Design and development of torsional vibration sensor with high frequency range and high spectral resolution based on the TIMS method and FPGA.

- Reconditioning of experimental test-bench to study bearing faults and energy anal-

ysis with interfaces for condition monitoring of different rotor-faults.

- Experimental data of lubrication starvation that includes lateral and torsional vibrations, voltage, current, torque and speed.
- Experimental results of lateral vibrations proving that extra clearance is the origin of the characteristic signal of lubrication starvation.
- Comparison of fault indicators for detection of lubrication starvation and proving that FK is the best indicator.
- Experimental results and analysis proving the presence of BPFO and FTF in the spectra, which corroborates the theory of previous authors about the impacts on the entrance of the load zone.
- Simulation reults of sliding friction on ball bearings using the SKF, EHL and GW model.
- Experimental results of torsional vibrations validating the simulation results and proving that torsional vibrations are not a good candidate for detection or diagnosis of lubrication starvation.
- An energy analysis of the impact of lubrication starvation on efficiency showing that efficiency could be reduced from 4% to 60%.
- A case study that proves the economical advantage of implementing condition monitoring on a real plant.

# REFERENCES


[1] T. A. Harris, "Rolling bearing macrogeometry," in *Rolling Bearing Analysis*, ch. 2, pp. 47–80, John Wiley and Sons, 4th ed., 2001.

[2] R. B. Randall, *Vibration-Based Condition Monitoring: Industrial, Aerospace and Automotive Applications*. John Wiley & Sons, Mar 2011.

[3] J. Antoni and R. Randall, "The spectral kurtosis: application to the vibratory surveillance and diagnostics of rotating machines," *Mechanical Systems and Signal Processing*, vol. 20, no. 2, pp. 308 – 331, 2006.

[4] N. Ertugrul, *LabVIEW for Electric Circuits, Machines, Drives, and Laboratories*. Prentice Hall, 2002.

[5] T. A. Harris, "Rolling bearing types and applications," in *Rolling Bearing Analysis*, ch. 1, pp. 1–44, Hoboken, NJ: John Wiley and Sons, 4th ed., 2001.

[6] T. A. Harris, "Distribution of internal loading in statistically loaded bearings," in *Rolling Bearing Analysis*, ch. 7, pp. 231–385, John Wiley and Sons, 4th ed., 2001.

[7] H. Penrose, "Large electric motor reliability: what did the studies really say?." `https://www.efficientplantmag.com/2012/03/large-electric-motor-reliability-what-did-the-studies-really-say/` , 2012. [Online; accessed 27-November-2017].

[8] J. Vance, F. Zeidan, and B. Murphy, "Bearings and their effect on rotordynamics," in *Machinery Vibrations and Rotordynamics*, pp. 171–269, Wiley Online Library, 2010.

[9] C. Radu, "The most common causes of bearing failure and the importance of bearing lubrication." `http://www.rkbbearings.com/admin/gest{_}docs{_}res/attach1/1271884609.pdf` , 2010. [Online; accessed 27-November-2017].

[10] B. P. Graney and K. Starry, "Rolling element bearing analysis," *Materials Evaluation*, vol. 70, no. 1, pp. 78–85, 2012.

[11] G. Singh and S. A. S. Al Kazzaz, "Isolation and identification of dry bearing faults in induction machine using wavelet transform," *Tribology International*, vol. 42, no. 6, pp. 849–861, 2009.

[12] P. Boškoski, J. Petrovčič, B. Musizza, and a. Juričić, "Detection of lubrication starved bearings in electrical motors by means of vibration analysis," *Tribology International*, vol. 43, pp. 1683–1692, Sep 2010.

[13] K. M. Ragulskis and A. Y. Yurkauskas, "Diagnostic features of bearings and bearing units," in *Vibration of Bearings* (E. I. Rivin, ed.), pp. 12–35, CRC Press, 1989.

[14] H. Chengbing and Y. Gu, "An increment transfer matrix method for the coupled bending and torsional vibrations of turbo-generator shafts with rub-impact," *Advances in information Sciences and Service Sciences*, vol. 4, no. 18, pp. 189–196, 2012.

[15] A. Darpe, K. Gupta, and A. Chawla, "Coupled bending, longitudinal and torsional vibrations of a cracked rotor," *Journal of Sound and Vibration*, vol. 269, pp. 33–60, Jan 2004.

[16] M. LI and L. YU, "Analysis of the coupled lateral torsional vibration of a rotor-bearing system with a misaligned gear coupling," *Journal of Sound and Vibration*, vol. 243, pp. 283–300, May 2001.

[17] T. H. Patel, M. J. Zuo, and A. K. Darpe, "Vibration response of coupled rotor systems with crack and misalignment," *Proceedings of the Institution of Mechanical Engineers, Part C: Journal of Mechanical Engineering Science*, vol. 225, pp. 700–713, Mar 2011.

[18] T. H. Patel and A. K. Darpe, "Coupled bending-torsional vibration analysis of rotor with rub and crack," *Journal of Sound and Vibration*, vol. 326, pp. 740–752, Oct 2009.

[19] A. W. Lees, M. I. Friswell, and G. Litak, "Torsional vibration of machines with gear errors," *Journal of Physics: Conference Series*, vol. 305, p. 012020, Jul 2011.

[20] C. Liu, D. Jiang, J. Chen, and J. Chen, "Torsional vibration and fatigue evaluation in repairing the worn shafting of the steam turbine," *Engineering Failure Analysis*, vol. 26, pp. 1–11, Dec 2012.

[21] J. Chen, R. B. Randall, B. Peeters, H. V. der Auweraer, and W. Desmet, "Automated misfire diagnosis in engines using torsional vibration and block rotation," *Journal of Physics: Conference Series*, vol. 364, May 2012.

[22] P. Charles, J. K. Sinha, F. Gu, L. Lidstone, and A. Ball, "Detecting the crankshaft torsional vibration of diesel engines for combustion related diagnosis," *Journal of Sound and Vibration*, vol. 321, pp. 1171–1185, Apr 2009.

[23] P. J. Sweeney and R. B. Randall, "Gear transmission error measurement using phase demodulation," *Proceedings of the Institution of Mechanical Engineers, Part C: Journal of Mechanical Engineering Science*, vol. 210, pp. 201–213, May 1996.

[24] S. K. Roy, A. R. Mohanty, and C. S. Kumar, "Fault detection in a multistage gearbox by time synchronous averaging of the instantaneous angular speed," *Journal of Vibration and Control*, vol. 22, pp. 468–480, May 2014.

[25] "Application of wavelet packet analysis for fault detection in electro-mechanical systems based on torsional vibration measurement," *Mechanical Systems and Signal Processing*, vol. 17, pp. 1219–1235, Nov 2003.

[26] C. Bujoreanu and F. Breaban, "Bearing scuffing detection and condition monitoring using virtual instrumentation," *Academic Journal of Manufacturing Engineering*, vol. 12, no. 2, pp. 23–28, 2014.

[27] J. Miettinen and P. Andersson, "Acoustic emission of rolling bearings lubricated with contaminated grease," *Tribology International*, vol. 33, no. 11, pp. 777–787, 2000.

[28] N. Tandon, G. Yadava, and K. Ramakrishna, "A comparison of some condition monitoring techniques for the detection of defect in induction motor ball bearings," *Mechanical Systems and Signal Processing*, vol. 21, pp. 244–256, Jan 2007.

[29] J. Jezic von Gesseneck, B. Caers, M. Van Overmeire, D. Lefeber, B. Vanderborght, and P. Schuurmans, "A torque-based method for the study of roller bearing degradation under poor lubrication conditions in a lead bismuth environment," *Nuclear Engineering and Design*, vol. 305, pp. 121–131, 2016.

[30] D. Sier, L. Xinglin, W. Jiugen, and T. Hongfei, "Frictional torque characteristic of angular contact ball bearings," *Journal of Mechanical Engineering*, vol. 47, no. 5, pp. 114–120, 2011.

[31] Y. Wang, F. Lin, H. Jiang, and W. Yuan, "Investigation on frictional characteristic of deep-groove ball bearings subjected to radial loads," *Advances in Mechanical Engineering*, vol. 7, no. 7, pp. 1–12, 2015.

[32] SKF, "The SKF model for calculating the frictional moment." `http://www.skf.com/binary/30-299767/index.html`. [Online; accessed 27-November-2017].

[33] R. W. Bruce, *Handbook of Lubrication and Tribology, Volume II: Theory and Design*, vol. 2. Boca Raton, FL: CRC press, 2012.

[34] "SKF General Catalogue." `http://www.boie.de/ftp/pub/skf/6000_I_EN.pdf`, 2005. [Online; accessed 27-November-2017].

[35] D. Dowson, "Elastohydrodynamic and micro-elastohydrodynamic lubrication," *Wear*, vol. 190, pp. 125–138, Dec 1995.

[36] A. Grubin and I. E. Vinogradova, *Investigation of the Contact of Machine Components*. Central Scientific Research Institute for Technology and Mechanical Engineering, 1949.

[37] D. Dowson and G. R. Higginson, "A numerical solution to the elastohydrodyamic problem," *Journal of Mechanical Engineering Science*, vol. 1, no. 1, pp. 6–15, 1959.

[38] D. Dowson, "Paper 10: Elastohydrodynamics," in *Proceedings of the Institution of Mechanical Engineers, Conference Proceedings*, vol. 182, pp. 151–167, SAGE Publications Sage UK: London, England, 1967.

[39] B. J. Hamrock and D. Dowson, "Isothermal elastohydrodynamic lubrication of point contacts: Part III: Fully flooded results," *Journal of Lubrication Technology*, vol. 99, p. 264, Apr 1977.

[40] J. I. McCool, "Comparison of models for the contact of rough surfaces," *Wear*, vol. 107, pp. 37–60, Jan 1986.

[41] J. A. Greenwood and J. B. P. Williamson, "Contact of nominally flat surfaces," *Proceedings of the Royal Society A: Mathematical, Physical and Engineering Sciences*, vol. 295, pp. 300–319, Dec 1966.

[42] J. Greenwood and J. Wu, "Surface roughness and contact: An apology," *Meccanica*, vol. 36, no. 6, pp. 617–630, 2001.

[43] J. F. Archard, "Elastic Deformation and the Laws of Friction," *Proceedings of the Royal Society A: Mathematical, Physical and Engineering Sciences*, vol. 243, pp. 190–205, Dec 1957.

[44] T. A. Harris, "Friction in fluid-lubricated rolling element-raceway contacts," in *Rolling Bearing Analysis*, ch. 13, pp. 461–481, John Wiley and Sons, 4th ed., 2001.

[45] V. L. Popov, "Contact between rough surfaces," in *Contact Mechanics and Friction*, ch. 7, pp. 97–116, Berlin, Heidelberg: Springer Berlin Heidelberg, 2010.

[46] R. Stribeck, "Ball bearings for various loads," *Trans. ASME*, vol. 29, pp. 420–463, 1907.

[47] E. E. Krämer, *Dynamics of Rotors and Foundations*. Berlin, Heidelberg: Springer Berlin Heidelberg, 1993.

[48] Y. Wijnant, J. Wensing, and G. Nijen, "The influence of lubrication on the dynamic behaviour of ball bearings," *Journal of Sound and Vibration*, vol. 222, pp. 579–596, May 1999.

[49] M. I. Friswell, *Dynamics of Rotating Machines*. Cambridge, United Kingdom: Cambridge University Press, 2010.

[50] N. Tandon and A. Choudhury, "A review of vibration and acoustic measurement methods for the detection of defects in rolling element bearings," *Tribology International*, vol. 32, no. 8, pp. 469–480, 1999.

[51] I. Standard, "10816-1: 1995," *Mechanical vibration-evaluation of machine vibration by measurements on non-rotating parts, Part 1, General guidelines*, vol. 1, 1995.

[52] T. Williams, X. Ribadeneira, S. Billingon, and T. Kurfess, "Rolling element bearing diagnostics in run-to-failure lifetime testing," *Mechanical Systems and Signal Processing*, vol. 15, pp. 979–993, 2001.

[53] L. M. Roger, "The application of vibration signature analysis and acoustic emission source location to on-line condition monitoring of anti-friction bearings," *Tribology International*, vol. 12, pp. 51–58, Apr 1979.

[54] C. Pachaud, R. Salvetat, and C. Fray, "Crest factor and kurtosis contributions to identify defects inducing periodical impulsive forces," *Mechanical Systems and Signal Processing*, vol. 11, pp. 903–916, 1997.

[55] R. Dwyer, "Detection of non-gaussian signals by frequency domain kurtosis estimation," in *Acoustics, Speech, and Signal Processing, IEEE International Conference on ICASSP'83.*, vol. 8, pp. 607–610, IEEE, 1983.

[56] W. T. P. Tse and T. C. Leung, *Advanced system for automatically detecting faults occurring in bearings*. Nova Science Publishers, 2010.

[57] J. Antoni, "Fast computation of the kurtogram for the detection of transient faults," *Mechanical Systems and Signal Processing*, vol. 21, no. 1, pp. 108–124, 2007.

[58] R. B. Randall and J. Antoni, "Rolling element bearing diagnostics-A tutorial," *Mechanical Systems and Signal Processing*, vol. 25, pp. 485–520, Feb 2011.

[59] J. S. Bendat, "The Hilbert transform and applications to correlation measurements," 1991.

[60] A. M. Schomerus, *Effectiveness of various techniques in reducing noise generated in measuring torsional vibration*. PhD thesis, Texas A & M University, Aug 2007.

[61] J. M. Vance and R. S. French, "Measurement of torsional vibration in rotating machinery," *Journal of Mechanisms, Transmissions, and Automation in Design*, vol. 108, no. 4, pp. 565–577, 1986.

[62] S. Seidlitz, R. Kuether, and M. Allen, "Experimental approach to compare noise floors of various torsional vibration sensors," *Experimental Techniques*, Jul 2014.

[63] R. Bharadwaj, A. Parlos, and H. Toliyat, "Adaptive neural network-based state filter for induction motor speed estimation," *IECON'99. Conference Proceedings. 25th*

*Annual Conference of the IEEE Industrial Electronics Society (Cat. No.99CH37029)*, vol. 3, pp. 1283–1288, 1999.

[64] J. Stein and H. Fick, "The Torsional stress analyzer for continuously monitoring turbine-generators," *IEEE Transactions on Power Apparatus and Systems*, vol. PAS-99, pp. 703–710, Mar 1980.

[65] M. Humer and S. Kulig, "Measurement and assessment of torsion oscillations in turbogenerators by using a torque sensor and robust observer," in *IECON'03. 29th Annual Conference of the IEEE Industrial Electronics Society (IEEE Cat. No.03CH37468)*, vol. 2, pp. 1369–1377, IEEE, 2003.

[66] R. Zhang, "Torsional vibration control of the main drive system of a rolling mill based on an extended state observer and linear quadratic control," *Journal of Vibration and Control*, vol. 12, pp. 313–327, Mar 2006.

[67] S. H. Kia, H. Henao, and G.-A. Capolino, "Torsional vibration monitoring using induction machine electromagnetic torque estimation," in *Industrial Electronics, 2008. IECON 2008. 34th Annual Conference of IEEE*, pp. 3120–3125, IEEE, Nov 2008.

[68] L. Murawski and A. Charchalis, "Simplified method of torsional vibration calculation of marine power transmission system," *Marine Structures*, vol. 39, pp. 335–349, Dec 2014.

[69] P. Wang, P. Davies, J. M. Starkey, and R. L. Routson, "A torsional vibration measurement system," *IEEE Transactions on Instrumentation and Measurement*, vol. 41, no. 6, pp. 803–807, 1992.

[70] S. Rothberg and N. A. Halliwell, "Vibration measurements on rotating machinery using laser doppler velocimetry," *Journal of Vibration and Acoustics*, vol. 116, pp. 326–331, Jul 1994.

[71] N. Halliwell, "The laser torsional vibrometer: a step forward in rotating machinery diagnostics," *Journal of Sound and Vibration*, vol. 190, pp. 399–418, Feb 1996.

[72] T. J. Miles, M. Lucas, N. A. Halliwell, and S. J. Rothberg, "Torsional and bending vibration measurement on rotors using laser technology," *Journal of Sound and Vibration*, vol. 226, pp. 441–467, Sep 1999.

[73] Z. Meng and B. Liu, "Research on torsional vibration noncontact measurement of rotary machine," in *Third International Symposium on Precision Mechanical Measurements* (K.-C. Fan, W. Gao, X. Yu, W. Huang, and P. Hu, eds.), pp. 6280 – 6280 – 6, International Society for Optics and Photonics, International Society for Optics and Photonics, Nov 2006.

[74] L. Xiang, S. Yang, and C. Gan, "Torsional vibration measurements on rotating shaft system using laser doppler vibrometer," *Optics and Lasers in Engineering*, vol. 50, pp. 1596–1601, Nov 2012.

[75] J. Mijares, B. Rasmussen, and A. Parlos, "Detection of lubrication starvation in ball bearings and preload effects," in *Proceedings of The Society of Machinery and Failure Prevention Technology*, (Virginia Beach, VA), pp. 1–10, MFPT, 2017.

[76] N. Sawalhi and R. B. Randall, "Simulating gear and bearing interactions in the presence of faults: Part I. The combined gear bearing dynamic model and the simulation of localised bearing faults," *Mechanical Systems and Signal Processing*, vol. 22, pp. 1924–1951, Nov 2008.

[77] R. Saidur, "A review on electrical motors energy use and energy savings," *Renewable and Sustainable Energy Reviews*, vol. 14, pp. 877–898, Apr 2010.

[78] Advance Manufacturing Office, "Estimating Motor Efficiency in the Field," 2012.

[79] L. Frosini and E. Bassi, "Stator current and motor efficiency as indicators for different types of bearing faults in induction motors," *IEEE Transactions on Industrial Electronics*, vol. 57, pp. 244–251, Jan 2010.

[80] "Ieee standard test procedure for polyphase induction motors and generators," *IEEE Std 112-2004 (Revision of IEEE Std 112-1996)*, pp. 1–83, Nov 2004.

# APPENDIX A

## BEARING TABLES FOR DEFORMATION AND LOAD DISTRIBUTION

In this section are found the tables used to calculate the Hertzian deformartion of a ball in Section 1.6 and the internal load distribution across the balls of the bearing.

| $F(\rho)$ | $\delta^*$ |
|---|---|
| 0 | 1 |
| 0.1075 | 0.9974 |
| 0.3204 | 0.9761 |
| 0.4795 | 0.9429 |
| 0.5916 | 0.9077 |
| 0.6716 | 0.8733 |
| 0.7332 | 0.8394 |
| 0.7948 | 0.7961 |
| 0.83495 | 0.7602 |
| 0.87366 | 0.7169 |
| 0.90999 | 0.6636 |
| 0.93657 | 0.6112 |
| 0.95738 | 0.5551 |
| 0.97290 | 0.4960 |
| 0.983797 | 0.4352 |
| 0.990902 | 0.3745 |
| 0.995112 | 0.3176 |
| 0.997300 | 0.2705 |
| 0.9981847 | 0.2427 |
| 0.9989156 | 0.2106 |
| 0.9994785 | 0.17167 |
| 0.9998527 | 0.11995 |
| 1 | 0 |

Table A.1: Dimensionless parameter $\delta^*$ as a function of $F(\rho)$. (Taken from [5])

| $\epsilon$ | Point Contact |
|---|---|
| 0 | 1/Z |
| 0.1 | 0.1156 |
| 0.2 | 0.1590 |
| 0.3 | 0.1892 |
| 0.4 | 0.2117 |
| 0.5 | 0.2288 |
| 0.6 | 0.2416 |
| 0.7 | 0.2505 |
| 0.8 | 0.2559 |
| 0.9 | 0.2576 |
| 1.0 | 0.2546 |
| 1.25 | 0.2289 |
| 1.67 | 0.1871 |
| 2.5 | 0.1339 |
| 5.0 | 0.0711 |
| $\infty$ | 0 |

Table A.2: Load distribution integral $J_r(\epsilon)$. (Taken from [6])

# APPENDIX B

# SYSTEM SPECIFICATIONS

## B.1 Sensors Specifications and Calibration

The voltage is measured using a hall effect sensor that generates a current which is circulated through a measuring resistor. The voltages are measured from phase to phase ($V_{AB}, V_{BC}$ and $V_{CA}$).

The voltage to be measured is around 240 V, hence a selected resistance $R_1 = 25k\Omega$ is used according to the manufacturer specifications. A measuring resistance of $R_m = 174\Omega$ is selected. The conversion ratio is 2500:1000 (2.5:1) then the sensitivity of the voltage sensor is found to be

$$V_r = \left(\frac{V_a}{174\Omega}\right)\left(\frac{1.0}{2.5}\right)(25k\Omega) = 57.47 * V_a \tag{B.1}$$

where $V_r$ is the real voltage while $V_a$ is the measured or acquired voltage.

The current is measured in each of the phases ($I_a, I_b$, and $I_c$) using the current transducer LAH25-NP from the brand LEM. This sensor is based on a Hall effect method which generates a current that circulates through a measurement resistance. The sensor is configured to have a ratio of 1:1000 and the measurement resistance is $110\Omega$. Hence, the sensitivity of the current sensor is then $9\frac{Amps}{V}$ with a measured offset of 2.1A.

For the torque sensor the sensitivity was found to be $2\frac{Nm}{V}$ while for the tachometer $1000\frac{rpm}{V}$.

## B.2 Bearings Dimensions and Frequencies

The bearings used for the experimentation of lubrication starvation are the standard series 6204-2RS-10 which is a deep grove ball bearing for radial loads and shaft diamater of $\frac{5}{8}$in. The bearing has plastic seals which allow an easy removal of the lubricant. The dimensions and frequencies of interest for fault diagnosis are presented in Table B.1. The bearing should be assembled with a tight tolerance, hence the bearing should be heat mounted on the shaft.

| Ball Diameter (in) | # of Balls | Pitch Diameter (in) | BSF Ball Spin | FTF Fundamental Train | BPFI Inner Ring Defect | BPFO Outer Ring Defect | BDF Ball Defect |
|---|---|---|---|---|---|---|---|
| 0.3125 | 8 | 1.3189 | 1.99 | 0.38 | 4.95 | 3.05 | 3.98 |

*Table coefficient values multiplied by speed.

Table B.1: Dimension and frequencies for bearing 6204-2RS-10

## B.3 Thermal Expansion Coefficients

To calculate the thermal expansion on each of the bearing components is necessary to know the linear coefficients of expansion. Table B.2 provide the coefficients for the materials for the ball bearing 6204-2RS-10, the housing and shaft.

## B.4 Procedure to Control the Lubricant Level

In order to control the amount of lubricant five bearings where weighted before and after removing the grease. Table B.3 present the results for five tests, from where the amount of grease for a full lubrication level was approximated to 1.8gr. A syringe is used to distribute the lubricant in all balls of the bearing, hence the relation between was previously found to be 1.15 ml/gr.

| Component | Material | Coefficient $ppm/C^{\circ}$ |
|---|---|---|
| Bearing | Chrome Steel | 10 |
| Housing | Aluminum | 23 |
| Shaft 1 | Steel 1040 | 11.3 |
| Shaft 2 | SS 303 | 17.2 |

Table B.2: Linear thermal expansion coefficients

| Bearing weight (g) | |
|---|---|
| Lubricated | Dry |
| 107.03 | 105.37 |
| 107.03 | 105.35 |
| 107.02 | 105.35 |
| 107.03 | 105.35 |
| 107.01 | 105.35 |
| Average (g) | |
| 107.024 | 105.354 |

Table B.3: Lubricant measurements

APPENDIX C

LATERAL VIBRATIONS EXPERIMENTAL RESULTS

## C.1 Dry vs Lubricated Results

In C.1 shows a clear peak on the FTF for the dry conditions but not many harmonics. In the lubricated test is possible to observe the high peak in the BPFO and the 2nd and 3rd harmonics.

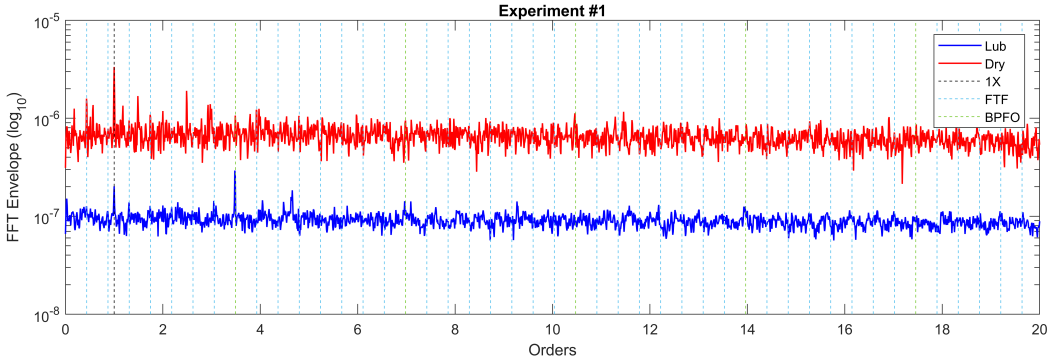


Figure C.1: Experiment 1 Dry vs Lubricated

In C.2 at the dry conditions is possible to observe the FTF peak and some of the harmonics while the BPFO is present but in a smaller magnitude than FTF. In the case of the lubricated contidions the FTF is shown in some of the harmonics while the BPFO is clearly shown in the main and harmonics.

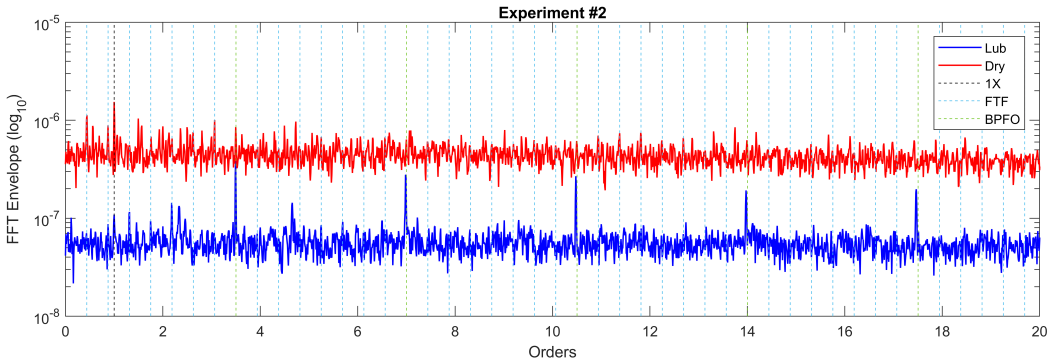


Figure C.2: Experiment 2 Dry vs Lubricated

In C.3 the FTF is clearly shown in the dry conditions with some low frequency side-bands while for the lubricated conditions there is no evidence of FTF. BPFO is clearly showed in both dry and lubricated conditions.

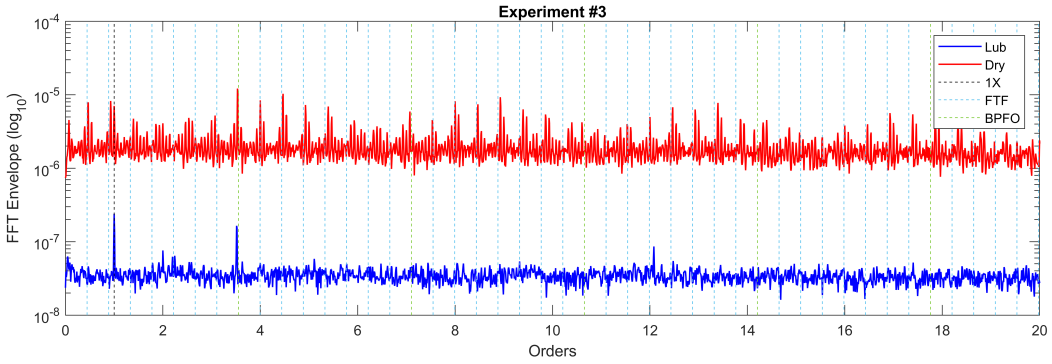


Figure C.3: Experiment 3 Dry vs Lubricated

In C.4 the main BPFO and its harmonics are clearly shown for the lubricated and dry conditions while the FTF appears only in the harmonics of the lubricated conditions and in low levels at the dry conditions.

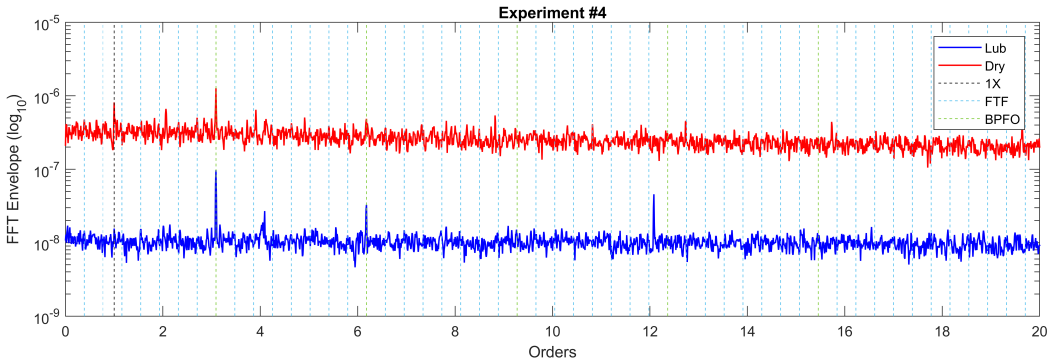


Figure C.4: Experiment 4 Dry vs Lubricated

In C.5 the main BPFO and its harmonics are clearly shown for the lubricated and dry conditions, some sidebands close to half the rotating frequency (0.5X) appear around BPFO indicating a modulation. The FTF appears at low levels in the harmonics of the dry conditions while for the lubricated conditions there is a clear peak in the FTF but not many harmonics.

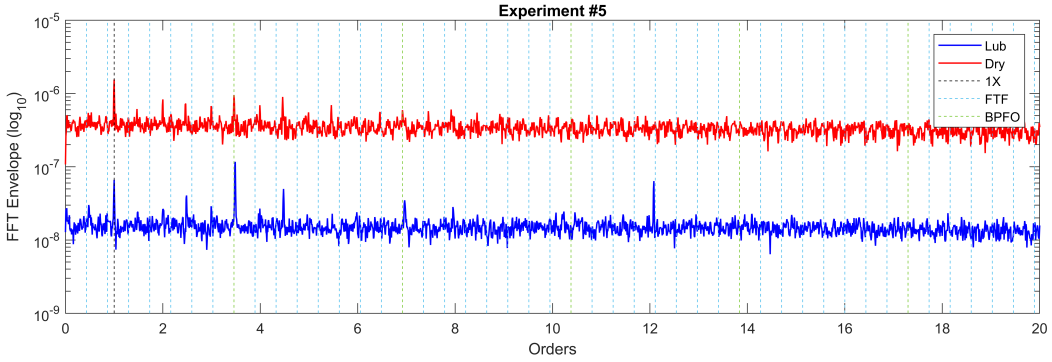


Figure C.5: Experiment 5 Dry vs Lubricated

In C.6 the main FTF clearly appears in the dry conditions with several harmonics while the are only few matching harmonics and no main FTF for the lubricated conditions. The

BPFO presents a clear peak in the main for lubricated while only a small peak in the main for the dry conditions.

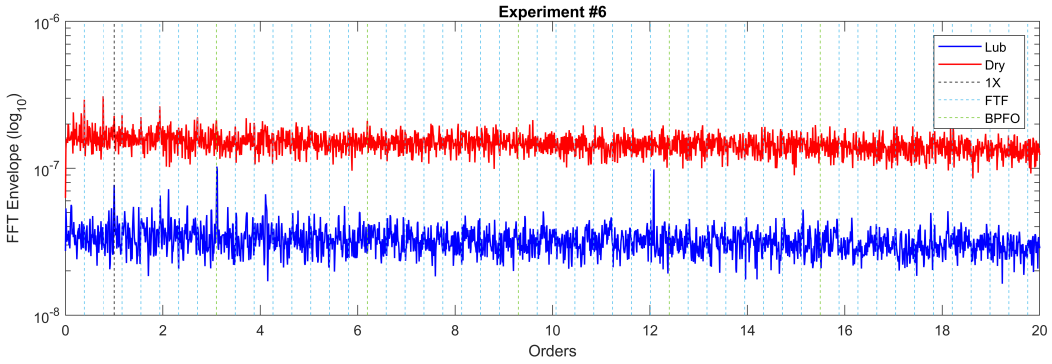


Figure C.6: Experiment 6 Dry vs Lubricated

In C.7 presents clear peaks in the main FTF and BPFO and their harmonics for both the dry and lubricated conditions.

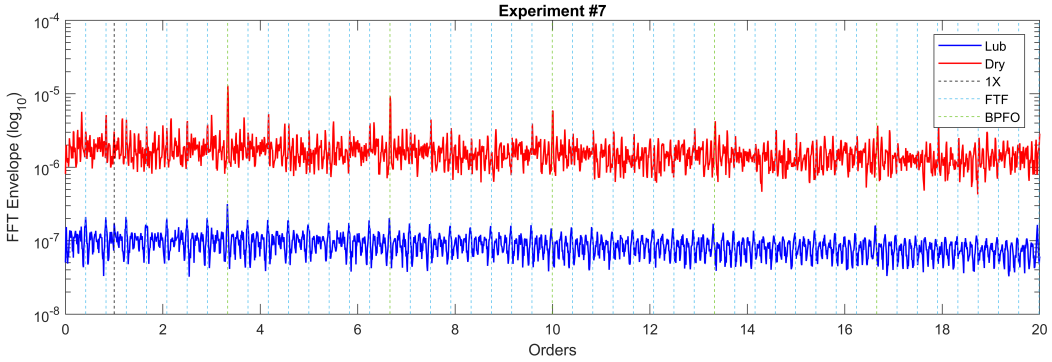


Figure C.7: Experiment 7 Dry vs Lubricated

In C.8 presents clear peaks in the main FTF and BPFO and their harmonics for both the dry and lubricated conditions.

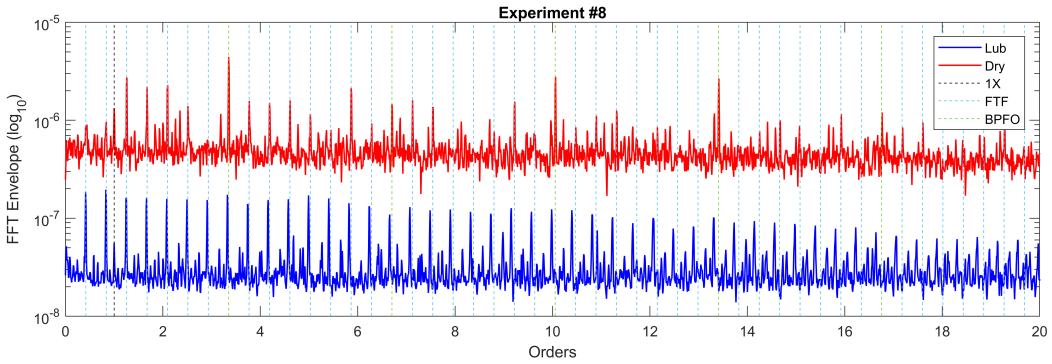


Figure C.8: Experiment 8 Dry vs Lubricated

C.9 presents clear peaks in the main FTF and BPFO and their harmonics for both the dry and lubricated conditions.

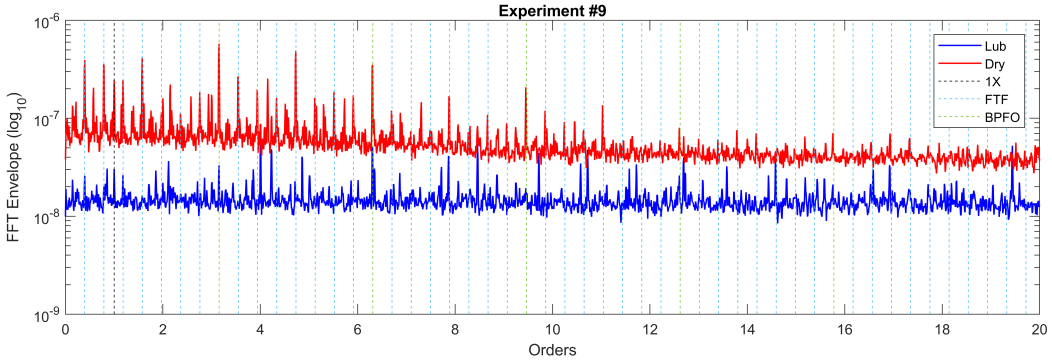


Figure C.9: Experiment 9 Dry vs Lubricated

C.10 presents clear peaks in the main FTF and BPFO and their harmonics for both the dry and lubricated conditions.

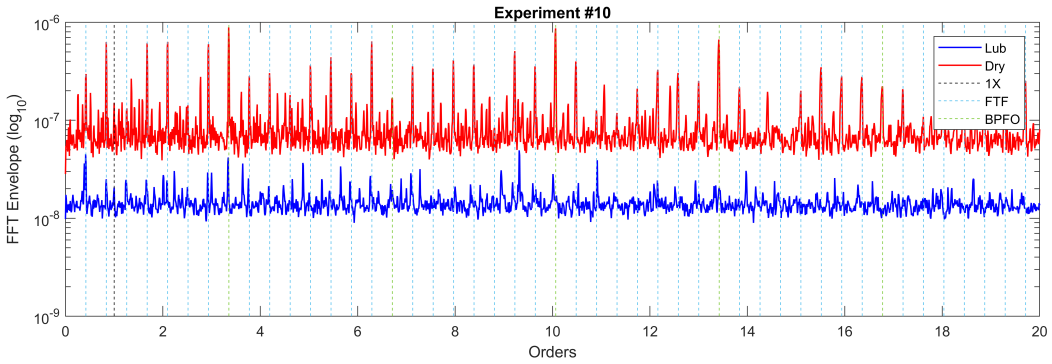


Figure C.10: Experiment 10 Dry vs Lubricated

C.11 presents clear peaks in the main BPFO and their harmonics for both the dry and lubricated conditions. The FTF also present a clear peak in the main and its harmonics but in a smaller amplitude as the BPFO.

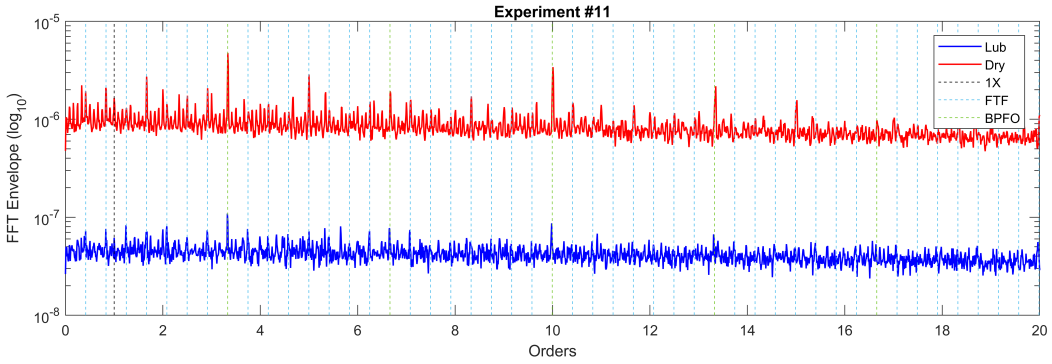


Figure C.11: Experiment 11 Dry vs Lubricated

C.12 presents clear peaks in the main FTF and BPFO and their harmonics for both the dry and lubricated conditions.

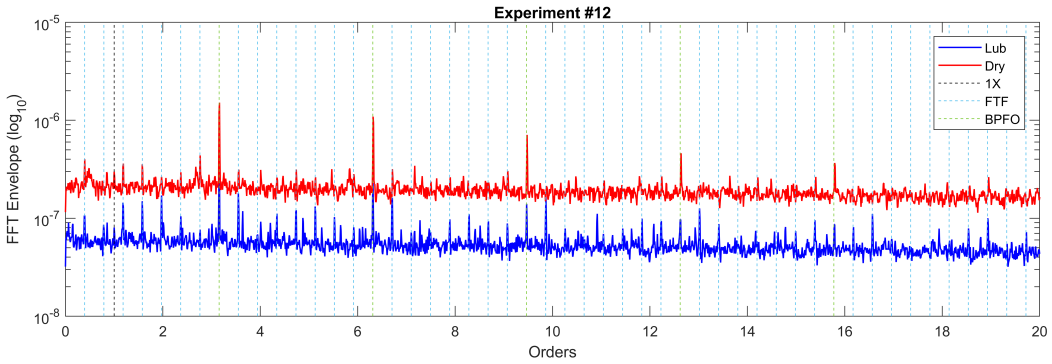


Figure C.12: Experiment 12 Dry vs Lubricated

## C.2 Dry vs Interference Results

C.13 do not show activity on the BSF for the interference test. Is not clear if the frequency peaks match the FTF and BPFO and their harmonics.

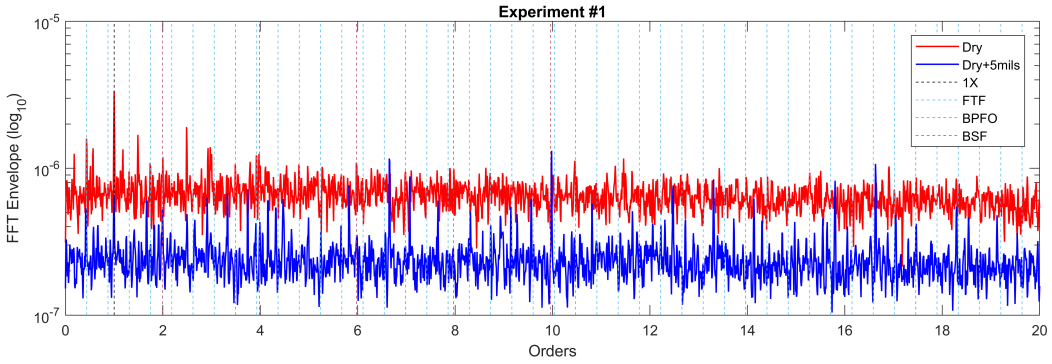


Figure C.13: Experiment 1 dry vs dry with interference

C.14 do not show activity on the BSF for the interference test. Is not clear if the frequency peaks match the FTF and BPFO and their harmonics.

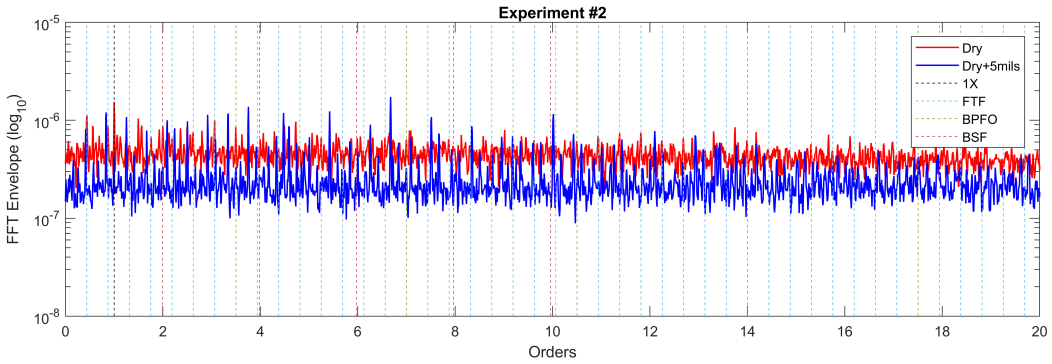


Figure C.14: Experiment 2 dry vs dry with interference

C.15 shows a clear peak on the BSF and its harmonics for the interference test. Is not clear if the frequency peaks match the FTF and BPFO and their harmonics.

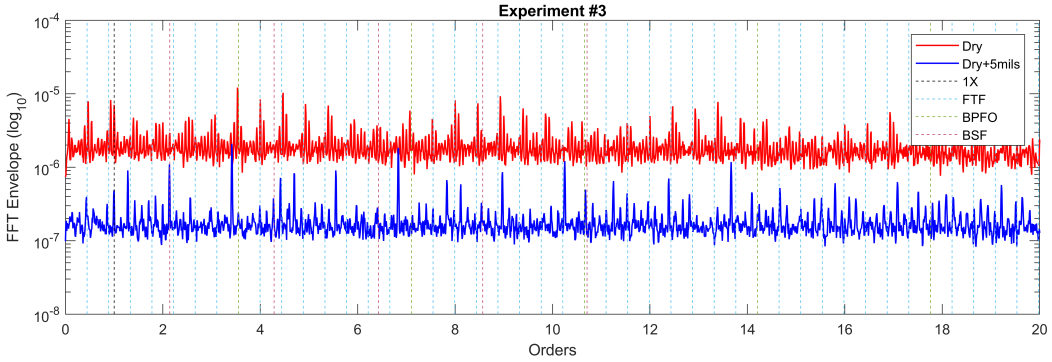


Figure C.15: Experiment 3 dry vs dry with interference

C.16 shows a clear peak on the BSF and its harmonics for the interference test. . Is not clear if the frequency peaks match the FTF and BPFO and their harmonics.

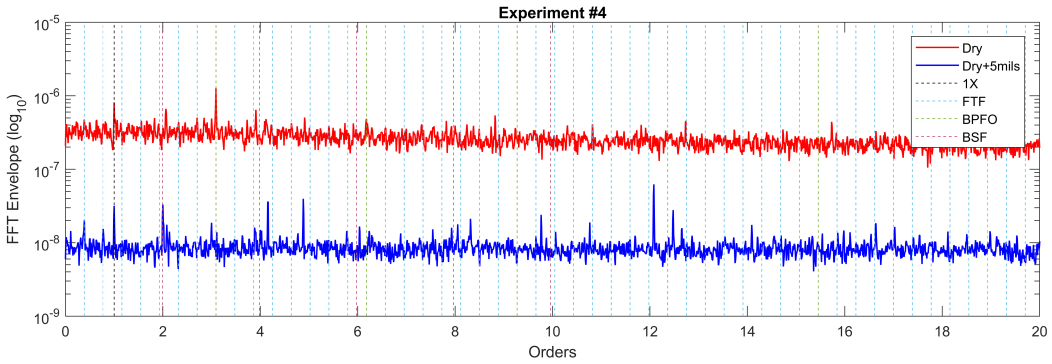


Figure C.16: Experiment 4 dry vs dry with interference

C.17 shows a clear peak on the BSF and its harmonics for the interference test. . Is not clear if the frequency peaks match the FTF and BPFO and their harmonics.

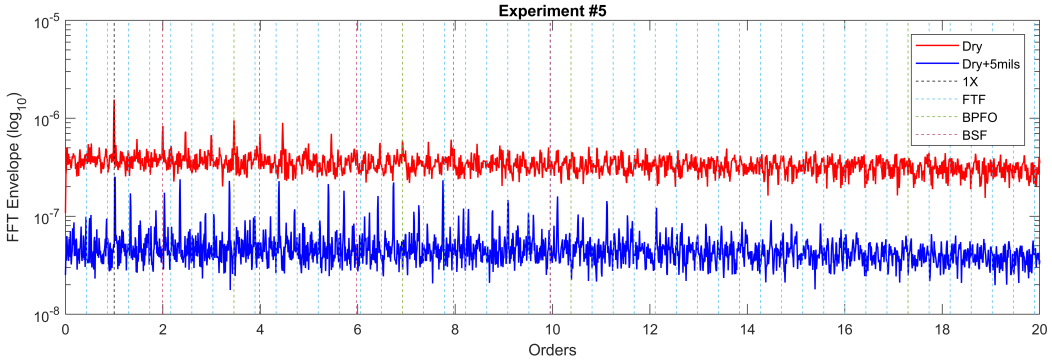


Figure C.17: Experiment 5 dry vs dry with interference

C.18 shows high activity on the BSF for the interference test with some sidebands indicatin amplitude modulation by a frequency close to the FTF. Is not clear if the frequency peaks match the FTF and BPFO and their harmonics.

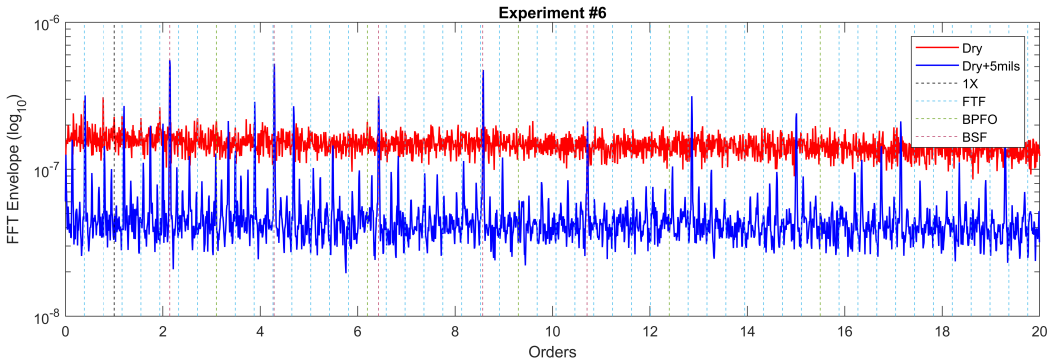


Figure C.18: Experiment 6 dry vs dry with interference